EXPERIMENTAL INVESTIGATIONS AND THEORETICAL MODELING OF LARGE AREA MASKLESS PHOTOPOLYMERIZATION WITH GRAYSCALE EXPOSURE

A Thesis
Presented to
The Academic Faculty

by

Matthew Conrad

In Partial Fulfillment
of the Requirements for the Degree
Masters of Science in the
George W. Woodruff School of Mechanical Engineering

Georgia Institute of Technology
December 2011

EXPERIMENTAL INVESTIGATIONS AND THEORETICAL MODELING OF LARGE AREA MASKLESS PHOTOPOLYMERIZATION WITH GRAYSCALE EXPOSURE

Approved by:

Dr. Suman Das
Woodruff School of Mechanical Engineering
Georgia Institute of Technology

Dr. Kyriaki Kalaitzidou
Woodruff School of Mechanical Engineering
Georgia Institute of Technology

Dr. John Halloran
Department of Materials Science and Engineering
University of Michigan

Dr. Dajun Yuan
Woodruff School of Mechanical Engineering
Georgia Institute of Technology

Date Approved: November 10, 2011

To Christina, whose patience with my whims, encouragement through my fears, and love in the midst of pain gives me strength to live with joy and integrity.

ACKNOWLEDGEMENTS

I would like to acknowledge my advisor, Professor Suman Das, for his willingness to incorporate me into his research group. I am thankful that he allowed me to pursue such an interesting research topic and for his advice throughout the research process. I appreciate his willingness to show me the bigger picture of the Direct Digital Manufacturing of Airfoils project by arranging for me to tour the PCC Airfoils Foundry to learn about investment casting. I am also grateful for being provided the opportunity to attend the 2011 SFF Symposium in Austin, Texas to present my research.

I would like to acknowledge Dr. Dajun Yuan, and Professors John Halloran and Kyriaki Kalaitzidou for serving on my thesis committee. I am grateful for all their advice and time put forth to develop my ability to conduct high quality research. I would also like to acknowledge all the members of the Direct Digital Manufacturing Laboratory for their frequent conversations regarding the interpretation of experimental results. I would like to specifically acknowledge Taiwo R. Alabi, for providing instrumental dialogue in the development of the scattering length pixelation model and for providing assistance in many of the experiments conducted for this thesis. I would also like to acknowledge Professor Haskell Beckham for allowing me access to his laboratory to use the FTIR instrument. In addition, much appreciation is due to Ryan Breneman for his work on conducting binder burnout and sintering experiments for my research.

Most importantly, I would like to acknowledge my wife, Christina Conrad, whose constant love, support and encouragement gave me the strength to successfully complete my research objectives. She helped me maintain a healthy perspective regarding my research and reminded me of what is most important and for that I am truly grateful.

TABLE OF CONTENTS

LIST OF TABLES

Page

LIST OF FIGURES

Page

LIST OF ABBREVIATIONS

LAMP	Large Area Maskless Photopolymerization
PCMS	Photocurable Ceramic Material System
UV	Ultraviolet
GSS	Grayscale Support Structure
BBO	Binder Burnout
SLM	Spatial Light Modulation
DMD	Digital Micro-mirror Device
HDDA	Hexanediol Diacrylate
SEM	Scanning Electron Microscopy
FTIR	Fourier Transform Infrared Spectroscopy
ATR	Attenuated Total Reflectance
HDS	Harlequin Dispersive Screening
ND	Neutral Density
OD	Optical Density
R^2	Coefficient of Determination
CCD	Charge Coupled Device

LIST OF SYMBOLS

In	Photoinitiator molecule
k_d	Initiation rate constant
R_i	Rate of initiation
ϕ_i	Quantum efficiency of initiation
ϵ	Molar extinction coefficient
I_a	Absorbed light intensity
M	Monomer molecule
M·	Radical monomer
k_i	Initiation rate of monomer molecules
P_n·	Radical polymer chain of length n
k_p	Propagation rate constant
P_{n+1}·	Radical polymer chain of length n+1
P_m·	Radical Polymer chain of length m
P_{n+m}	Dead polymer chain of length n+m
P_m	Dead polymer chain of length m
k_t	Termination rate constant
z	Depth into PCMS
I(x,y,z)	Light intensity distribution in PCMS
I(x,y,0)	Light intensity incident to surface of PCMS
D_p	Resin sensitivity
C_d	Cure depth
E	Exposure dose

E_c	Critical exposure dose
I_o	Light intensity incident to PCMS
t	Time
l_{sc}	Scattering length
Φ	Ceramic volume fraction
c_p	Concentration of photoinitiator
ε_p	Molar extinction coefficient of photoinitiator
c_A	Concentration of UV absorber
ε_A	Molar extinction coefficient of UV absorber
h	Plank's constant
ν	Frequency of light
Ω	Number of absorbed radicals for UV absorber
γ_Q	Effectiveness of inhibitors
Q	Concentration of inhibitors
γ_O	Effectiveness of oxygen
O	Concentration of oxygen
γ_A	Concentration of UV absorbers
α	Degree of conversion
n	Number transparent of pixels per unit area
a	Side length of pixel

g	Grayscale factor
I_{gr}	Average projected light intensity
G	Grayscale value of projected image
r	Gaussian radius
t_c	Critical exposure time
$E_{c,DE}$	Dose equivalent critical energy
$E_{c,excess}$	Excess critical energy dependent on light intensity
I_{min}	Transition light intensity
f	Proportionality factor
γ_{INH}	Effectiveness of inhibitors
c_{INH}	Concentration of inhibitors
$D_{p,sr}$	Screening resolution dependent resin sensitivity
B	Exposure diameter
C_w	Cure width

SUMMARY

Large Area Maskless Photopolymerization (LAMP) is a technology being developed by a team compromising The Georgia Institute of Technology, The University of Michigan, PCC Airfoils and Honeywell to fabricate integrally-cored ceramic molds for the investment casting of turbine airfoils. In LAMP, ultraviolet (UV) light in the form of bitmap images is projected from a spatial light modulator (SLM) onto a photocurable ceramic material system (PCMS). Exposed and unexposed regions are determined through black and white portions of the bitmaps, where white pixels correspond to exposed regions and black pixels correspond to unexposed regions. UV light induces photopolymerization and the formation of an insoluble solidified network. Three-dimensional structures are built layer-by-layer through sequential application and curing of PCMS layers of 100μm thickness. To date, ceramic molds fabricated using LAMP have been successfully implemented in investment casting of single-crystal turbine airfoils without internal cooling schemes. Two particularly important challenges for the fabrication of airfoil molds with internal cooling passages are: (a) fabrication of unsupported structures in the mold geometry and; (b) mitigation of internal stresses that arise during layer-by-layer build-up due to volumetric shrinkage during photopolymerization. Unsupported geometries arise in nearly every cored airfoil mold and often in a location where support structures cannot be easily removed after fabrication. Internal stresses generated by volumetric shrinkage can lead to cracking during binder burnout (BBO), sintering and casting. This thesis aims to simultaneously address these challenges through the investigation of grayscale exposure to control the degree of monomer conversion during photopolymerization of single and multiple layers.

The effective intensity of the UV light incident on the monomer system can be reduced by selectively turning off pixels within the nominally "white" or "on" regions of the projected bitmaps, effectively producing an exposure with a lower light intensity. In an effort to reduce internal stresses in the mold, the grayscale exposure can be tuned to create regions of uncured or partially cured monomer within the mold geometry to reduce the connectivity between cured regions and thus reduce the net effect of volumetric shrinkage. Grayscale exposure can also be used to generate support structures with a low degree of polymerization to create a gel state beneath and surrounding the unsupported segments of the mold, which can be washed away after completion of mold fabrication. In order to successfully utilize grayscale techniques in LAMP, the cure depth must be predicted. This is accomplished through cure depth measurements at different exposure times to develop a "working curve," which is used to predict the depth of cure. In addition, the degree of monomer conversion and its relation to cure depths resulting from grayscale exposure must be understood. Measurements of the degree of conversion are obtained through Fourier Transform Infrared spectroscopy (FTIR). Empirical models are developed and compared to theoretical predictions. Also, the scattering length pixelation model is introduced as a technique to predict the light intensity distribution within the PCMS for exposure patterns at multiple length scales. Results from these grayscale investigations are then applied to LAMP and the effectiveness of grayscale to fabricate unsupported geometries and internal stresses from volumetric shrinkage is discussed.

CHAPTER 1

INTRODUCTION

Large Area Maskless Photopolymerization (LAMP) is a technology being developed by a team compromising The Georgia Institute of Technology, The University of Michigan, PCC Airfoils and Honeywell to disrupt the current state-of-the-art investment casting process for manufacturing turbine airfoils. Investment casting of airfoils utilizes a lost-wax process to define the external features of the airfoil geometry and a core to define the internal cooling passages. A schematic of the investment casting process is shown in Figure 1.1. The process begins with the production of the tooling required to fabricate the core, patterns, mold and setters, which can typically amount to over one thousand tools [1]. This drastically increases the costs associated with design and revisions of the airfoil. The initial step in investment casting of cored airfoils is the fabrication of the leachable ceramic core by injection molding. Molten wax is then injection molded to incorporate the core and define the shape of the airfoil. The wax patterns are subjected to several rounds of slurry coating followed by stucco coating. Next, the molds are placed in an autoclave for dewaxing. After dewaxing, the molds are subjected to binder burnout and sintering to produce ceramic molds with the density and the mechanical properties appropriate for metal casting. This results in hollow mold shells with internal cores that are ready for casting. Once casting is completed, the mold shell is removed, the core is etched out and the airfoils are removed from the casting tree.

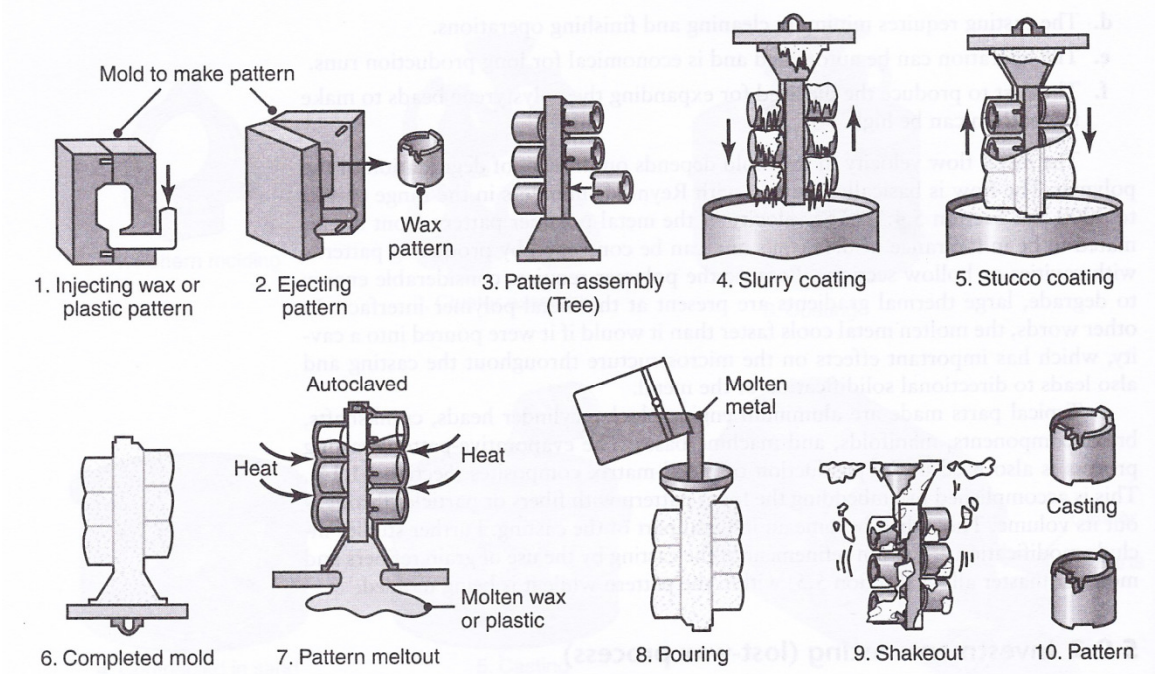

FIGURE 5.21 Schematic illustration of investment casting (lost-wax process). Castings by this method can be made with very fine detail and from a variety of metals. *Source:* Steel Founders' Society of America.

Figure 1.1: Schematic of the investment casting process [2].

The development of LAMP shows promise to significantly reduce the cost of airfoil fabrication by eliminating tooling costs and reducing the fabrication time characteristic of investment casting. Figure 1.2 shows how LAMP removes many of the procedures of traditional investment casting. It eliminates the lost wax process as well as the need for core, wax and setter tooling. In LAMP, the shell and core can be integrally fabricated as one component from a three-dimensional digital model converted to a set of images, which correspond to a specified layer, projected by a spatial light modulator (SLM) onto a photocurable ceramic material system (PCMS). The PCMS is a ceramic particle-filled acrylate monomer system with appropriate levels of photoinitiators, UV absorbers, and dispersants. This technology opens new possibilities for manufacturing components that were previously difficult or impossible to manufacture conventionally.

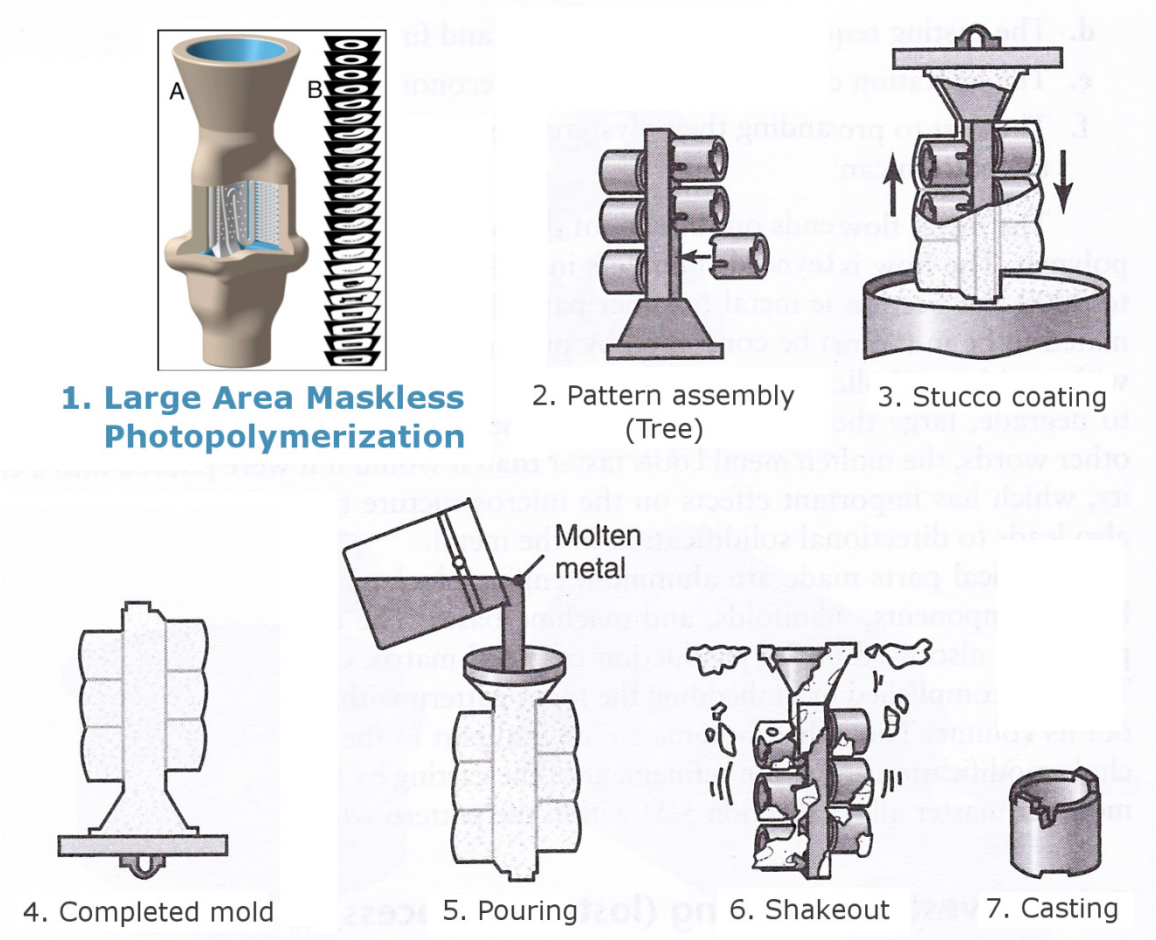

Figure 1.2: Schematic of the investment casting process [2] with the incorporation of LAMP [3].

1.1 Overview of Large Area Maskless Photopolymerization

The key characteristic of LAMP is layered fabrication of the PCMS by selective UV exposure through a scanning SLM within the individual layers, which is shown schematically in Figure 1.3. First, a three-dimensional model of the airfoil mold must be converted into a stack of high-resolution bitmap images of 100 μm thickness slices of the model. Once the images have been prepared, a 100 μm thickness layer of PCMS is placed within the exposure window by the material recoating system. Then, selected regions of

the resin are exposed to UV light through a maskless optical imaging system. The system consists of a UV light source, focusing optics and an SLM. The UV light is reflected onto a Texas Instruments digital micromirror device (DMD), a type of SLM which contains a 1024 x 768 micromirror array. Each mircomirror is a 17μm x 17μm reflective square that corresponds to an individual pixel of a 1500 dpi bitmap image loaded to the DMD, where the pixels can be white (exposed to UV) or black (unexposed). The projection lens and projection plane are calibrated so as to provide a 1:1 ratio of the DMD area to the exposure area. This enables the spatial resolution of UV exposure to be approximately 17 μm over the entire build area.

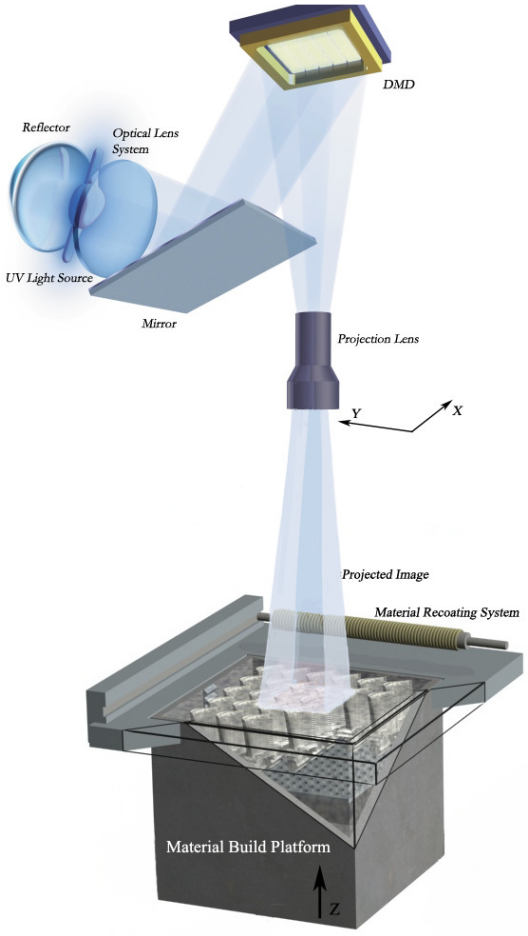

Figure 1.3: Schematic of the LAMP machine being developed in the Direct Digital Manufacturing Laboratory at Georgia Tech [4].

All components of the maskless optical imaging system are mounted on a high precision motion system, which enables the SLM to scan in a serpentine path over an exposure area much larger than the area of the DMD with 1μm positioning accuracy. During exposure to UV radiation, the selected regions of the PCMS polymerize forming a solid insoluble network around the ceramic particles. After exposure, the material build platform moves down by the layer thickness of 100 μm and the material recoating system applies an additional layer of PCMS. This process continues until all the cross-sectional images of the airfoil mold have been formed as successive layers to produce a green body airfoil mold. After the "build" is complete, excess uncured resin is drained and washed away by a solvent, such as isopropanol or Saf-T-Cure Cleanup 3D 101 (3D101). Then, the cured polymer is removed without significant modifications to mold geometry through a pyrolysis process called binder burnout (BBO). During BBO, the mold is gradually heated and held at 350°C for two hours to allow most of the polymer to burn off. Gradual heating continues up to temperatures of 600°C and followed by sintering to temperatures up to 1400°C to fuse together the ceramic particles to a relative density of 60-80% [3, 5]. The result is an integrally-cored ceramic mold ready for investment casting of airfoils.

The current capabilities of LAMP, as of July 2011, for the fabrication of airfoils are shown in Figure 1.4. The far left panel (a) shows the three-dimensional model of the airfoil mold to be fabricated with LAMP. The adjacent image (b) shows the external shell of the airfoil mold, while the image on the right (c) demonstrates how LAMP can fabricate the complex internal geometries of the core while being integrally connected to

the external shell. As a result, LAMP is a technology with the potential to disrupt the current state-of-the-art in investment casting applications.

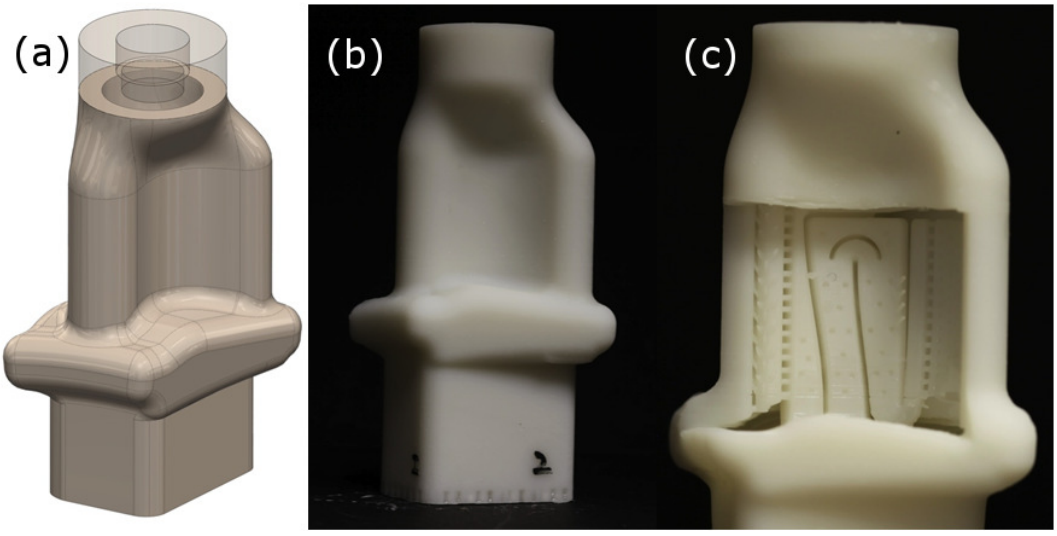

Figure 1.4: Example of the fabrication capabilities of LAMP. (a) A Three-dimensional model of the airfoil mold. (b) The external shell of an airfoil mold and (c) complex internal geometry of an integrally-cored airfoil mold fabricated with LAMP [6].

1.2 Motivation and Objective

While the success of LAMP is demonstrated in Figure 1.4, the fabrication of integrally-cored ceramic molds for the investment casting of single-crystal airfoils still faces some challenges. The two challenges investigated in this thesis are the fabrication of unsupported geometries and the mitigation of shrinkage-related internal stresses that arise in the fabrication of multiple layers.

Unsupported geometry is a feature that can be encountered during the course of a multilayer fabrication of a three-dimensional object where the feature has no connection to a region from the preceding layer. An example of this encountered in the fabrication of an integrally-cored airfoil mold is shown in Figure 1.5. The left image is a cross section

of an airfoil mold which corresponds to a layer that precedes an unsupported feature. It can be seen that the next layer contains an exposed region that has no overlap with the preceding layer. Once this layer is exposed to UV light, the position of the cured unsupported feature could be altered during the recoating of additional resin for subsequent layers or by sinking into the uncured resin.

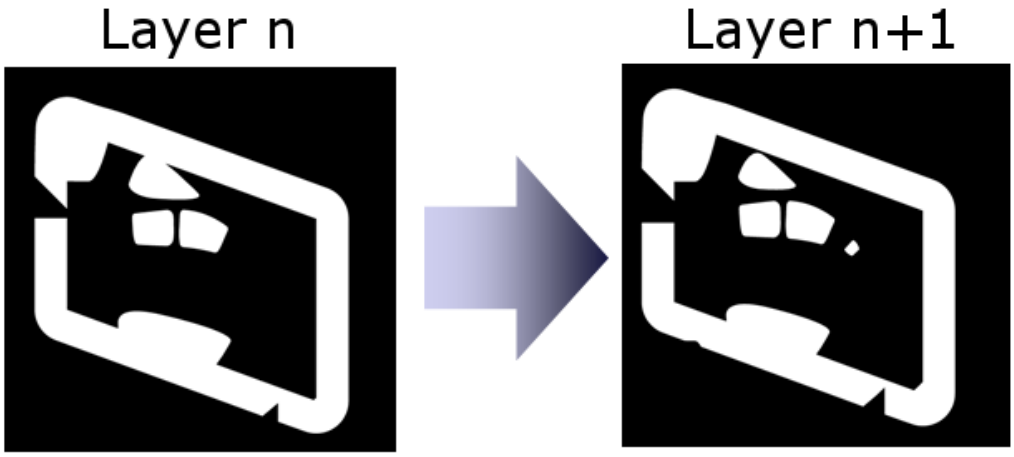

Figure 1.5: Example of an unsupported feature that arises in the fabrication of an integrally-cored airfoil mold.

Typically, unsupported geometries are fabricated by the use of support structures and through the optimization of the build orientation to minimize the number of necessary support structures [7]. Support structures are features added to the CAD model to maintain the defined geometry during part fabrication. Once the build is completed, the support structures are removed from the part to obtain the original specified geometry. It was found that the build orientation of an integrally-cored airfoil mold cannot be optimized to eliminate unsupported features. Also, the use of temporary supports in LAMP is challenging due to their location within the internal passages of the mold, which makes removing the temporary supports by mechanical methods nearly impossible. Two options to overcome this difficulty are: (a) redesign of the airfoil so that

the mold contains no unsupported features for a particular orientation and, (b) development a novel build technique where temporary support structures can be removed by an alternative method that does not impact the originally intended mold geometry. Airfoil redesign places a limitation on the components possible with LAMP. In an effort to expand the capabilities of LAMP, the focus of this thesis will be on the investigation and development of a novel method to fabricate unsupported features with LAMP.

During photopolymerization, volumetric shrinkage is induced [8, 9], and in the context of fabricating airfoil molds, the accumulation of volumetric shrinkage from each layer induces internal stresses between layers and can introduce geometrical inaccuracies. These internal stresses could be a source for crack initiation and propagation during BBO and sintering. Figure 1.6 shows the various defects observed after BBO and sintering. The left image (a) is of the airfoil mold green body prior to any heat treatment. It can be seen that green bodies demonstrate very few visible cracks prior to binder burnout, which makes crack prediction from visual inspection of green body molds difficult. The right image (b) is of the same mold after binder burnout and sintering. Three types of defects can be observed after sintering, which are horizontal “fissures”, vertical “cracks” and a well defined angular defect. The horizontal fissures propagate perpendicular to the build direction, which indicates that polymerization shrinkage is a likely source for this class of defects. To address the observed types of defects, other factors such as thermal polymerization of residual monomer within the mold, BBO stress, sintering stress and the techniques for large area scanning must be considered.

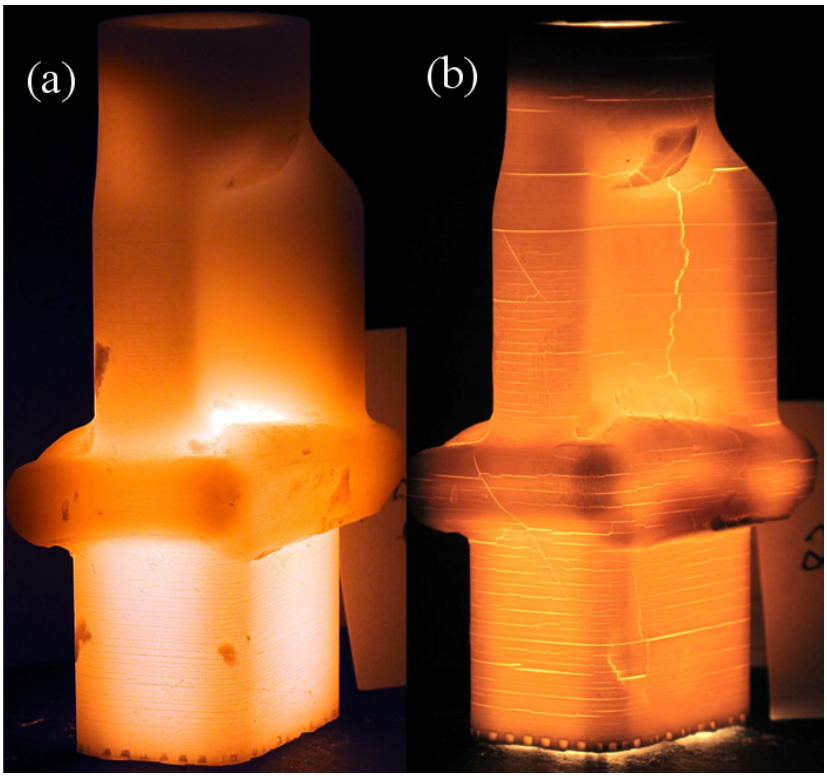

Figure 1.6: Example of cracks that form during binder burnout and sintering. (a) represents the mold green body prior to binder burnout and (b) is the mold after binder burnout and sintering [10].

In this thesis, the utilization of grayscale exposure techniques is investigated to simultaneously address the challenges of mitigating polymerization shrinkage stress build-up and the fabrication of unsupported features. Grayscale exposure exploits the properties of the SLM to selectively and simultaneously expose a large area (~2.3 cm^2) of ceramic loaded resin to UV light. In grayscale exposure, selected pixels are turned to black to leave small portions of the resin unexposed within a nominally exposed region. Under the proper conditions, grayscale exposure can cause the resin to respond as though the intensity of the incident UV light was reduced [11]. Consequently, grayscale exposure can provide a method to modify the curing characteristics during a single layer exposure. In theory, grayscale shows the possibility to fabricate unsupported geometries by creating a partially polymerized region surrounding the unsupported feature in order to provide

viscous support during fabrication. After completion of the build, the partially polymerized region could be removed through development with a selected solvent to reveal the successful fabrication of the unsupported feature. Grayscale exposure also has the potential to mitigate internal stresses during part fabrication by creating regions of fully cured resin separated by regions of uncured or partially cured resin. This could provide mechanical isolation of the cured regions interspersed with uncured regions, or provide a level of compliance between the fully cured and partially cured regions, converting macro-scale shrinkage resulting from an "all-white" uniform intensity exposure to local shrinkage resulting from a grayscale exposure.

In order to successfully implement grayscale exposure in LAMP, the effects must be characterized and methods to predict the resultant properties need to be developed. The objective of this thesis is to experimentally investigate the effects of grayscale exposure and develop a theoretical model to provide a framework for selecting the proper grayscale levels needed to successfully fabricate unsupported geometries and mitigate internal stresses. The validity of the grayscale model will then be tested through the use of grayscale exposure in LAMP to fabricate test components for unsupported features and internal stress relief.

1.3 Organization of Thesis

An outline for this thesis can be found in Figure 1.7. Chapter 2 provides a literature background on information relevant to the investigation of grayscale exposure as well as presents the experimental techniques utilized in these grayscale exposure investigations. Chapter 3 focuses on characterizing the optical properties of the maskless optical imaging system used in LAMP. This is accomplished by characterizing the net

effect of various grayscale exposures as well measuring the intensity profile at sub-pixel resolution. From these measurements, a simplified model is developed to describe the light intensity profile for an arbitrary distribution of exposed and unexposed pixels. Once the intensity distribution of UV light incident on the PCMS is understood, the effect of grayscale exposure can be characterized. Chapter 4 presents experimental data collected from cure depth measurements with grayscale exposure, where cure depth measurements yield critical curing parameters.

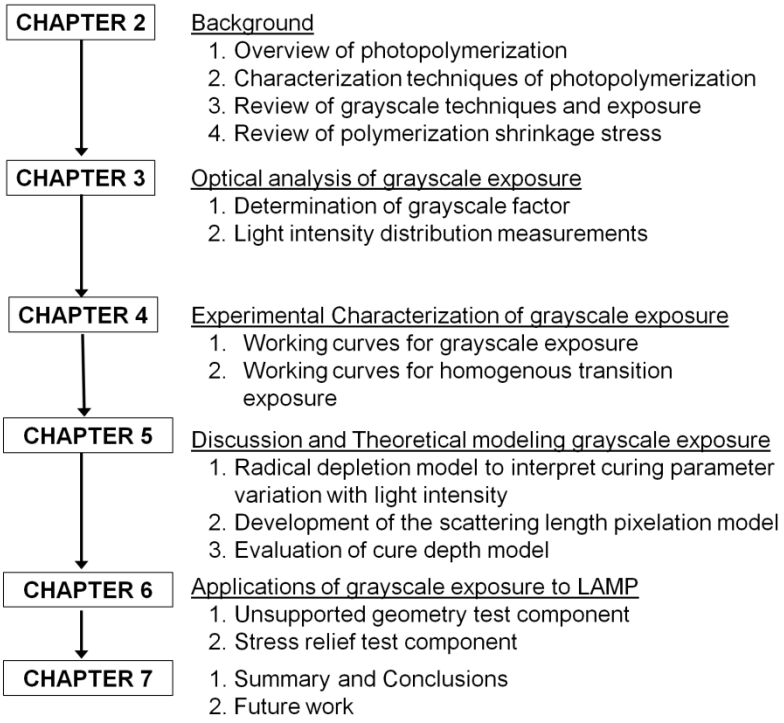

Figure 1.7: Organization of Thesis

Chapter 5 investigates the experimental results from Chapter 4, which demonstrate that the curing parameters behave as a function of uniform and grayscale light intensity. Chapter 5 also develops the scattering length pixelation model based on the experimental results and theoretical considerations. The model predicts the cure depth

based on the light intensity distribution and results are compared with the experimental data. Chapter 6 investigates the effect of grayscale and screening resolution on the degree of conversion through FTIR, which can be used to characterize volumetric shrinkage and shrinkage stress. The information obtained from the grayscale exposure photopolymerization investigations is applied to fabricate test features containing unsupported geometries and to mitigate photopolymerization shrinkage related defects that may occur during BBO and sintering. Chapter 7 provides a summary of the work completed and provides recommendations for future work.

CHAPTER 2

BACKGROUND

2.1 Overview of Photopolymerization

Photopolymerization is the primary physical phenomenon utilized in LAMP to produce a three-dimensional object from exposure to UV light. It is the process of rapidly transforming a liquid molecule into a solid polymer network with an appropriate light source. Due to fast cure speeds and excellent spatial resolution, photopolymerization is used in a wide variety of applications such as resin composites for tooth restorations [12], stereolithography [13], protective coatings, and manufacturing of microcircuits [14]. In the case of LAMP, photopolymerization is used to rapidly form hundreds or thousands of layers each with a prescribed thickness.

2.1.1 Kinetics of Photopolymerization

In general, there are three stages of photopolymerization, namely are initiation, propagation and termination. Two types of photopolymerization exist, which are cationic and free radical photopolymerization and are determined by the method of initiation. In cationic initiation, photons are absorbed by initiator molecules to cleave a proton, which then reacts with the liquid monomer molecule to initiate monomer chain propagation. In radical polymerization, radicals are generated through α-cleavage to form two separate molecules with unpaired electrons in their valence shell [15]. In LAMP, free radical photopolymerization is utilized in the PCMS to fabricate each layer of the build. Initiation is described by the following equation:

$$In \xrightarrow{k_d} 2R \cdot \tag{2.1}$$

Where *In* is the initiator molecule, k_d is the initiation rate constant and R· is the radical formed from splitting the initiator into two reactive species. The rate of initiation depends of the rate of photons introduced into the material system [16].

$$R_i = 2\phi_i \epsilon [In] I_a \tag{2.2}$$

Where R_i is the rate of initiation, ϕ_i is the quantum efficiency, ϵ is the molar extinction coefficient, $[In]$ is the photoinitiator concentration and I_a is the absorbed light intensity. The second phase of initiation is the addition of the primary radical to a monomer, M, to produce a chain initiating radical M_1· [17].

$$R\cdot + M \overset{k_i}{\rightarrow} M_1\cdot \tag{2.3}$$

Where k_i is the initiation rate of monomer radicals. Following the formation of a radical monomer is chain propagation, where a radical monomer reacts with additional monomers to increase the polymer chain length of M· to P·.

$$P_n\cdot + M \overset{k_p}{\rightarrow} P_{n+1}\cdot \tag{2.4}$$

Chain propagation can continue for hundreds to thousands of iterations with a rate constant of k_p. The rate of propagation is generally considered to be greater than the rate of initiation and thus, k_i is considered the rate limiting step. Eventually, the growing polymer chain will terminate. Termination can occur through a number of mechanisms, where the most common is bimolecular termination of two growing polymer chains [18].

$$P_n\cdot + P_m\cdot \overset{k_t}{\rightarrow} P_{n+m} \tag{2.5}$$

Here, k_t is the rate of termination. In addition to bimolecular termination, a polymer chain can terminate through disproportionation (eq. 2.6) and inhibition (eq. 2.7) [18]. Disproportionation occurs when two propagating polymer chains terminate to form two molecules, which reduces the molecular weight of the polymer. During inhibition, an

inhibitor species, Z, either intentionally or unintentionally included in the material system, reacts with a radical polymer chain to form a nonreactive species.

$$P_n\cdot + P_m\cdot \overset{k_t}{\rightarrow} P_n + P_m \quad 2.6$$

$$P_n\cdot + Z \overset{k_z}{\rightarrow} P_nZ\cdot \quad 2.7$$

The termination rate constant, k_t often includes both termination mechanisms of bimolecular combination and disproportionation. In addition, termination can occur in primary radicals and short polymer chains by primary radical depletion [19, 20].

2.1.2 Photocurable Ceramic Material System Used in LAMP

The PCMS consists of five components, which are the photoinitiator, monomer, UV absorber, ceramic particles and dispersant. The photoinitiator used is 1-hydroxy-cyclohexyl-phenyl-ketone (Irgacure 184) at 1.25 wt%, which was selected to efficiently polymerize the monomer hexanediol diacrylate (HDDA) at 18.52 wt%. An additional monomer, ethoxylated (4) pentaerythritol tetraacrylate, is also used at 2.26 wt% to reduce polymerization shrinkage. With these components, polymerization will occur if exposed to UV light. However, the resin sensitivity would not be ideal for LAMP. To reduce the resin sensitivity, i.e. the depth of light absorption, 0.05 wt% of hydroxyphenyl benzotriazole (Tinuvin 171) is added to the material system to act as a UV absorber and enable fabrication of successive layers of 100μm. In order to fabricate ceramic molds, a high volume fraction (55%) of ceramic particles is needed to obtain appropriate mold densities. Figure 2.1 shows an SEM micrograph of the ceramic particles used in LAMP, which are spherical silica particles with a d_{90} of 25μm and d_{50} of 7μm (Tecosphere Microdust). One challenge that arises when loading ceramic particles into a photocurable resin is aggregation. To formulate a homogenously loaded system, 6 wt% of Diethyl

polypropoxy-2 hydroxyethyl ammonium phosphate (Variquat CC-59) is used as a dispersant. All investigations into grayscale exposure, polymerization shrinkage stress mitigation and the fabrication of unsupported geometries reported in this thesis were conducted on the described PCMS.

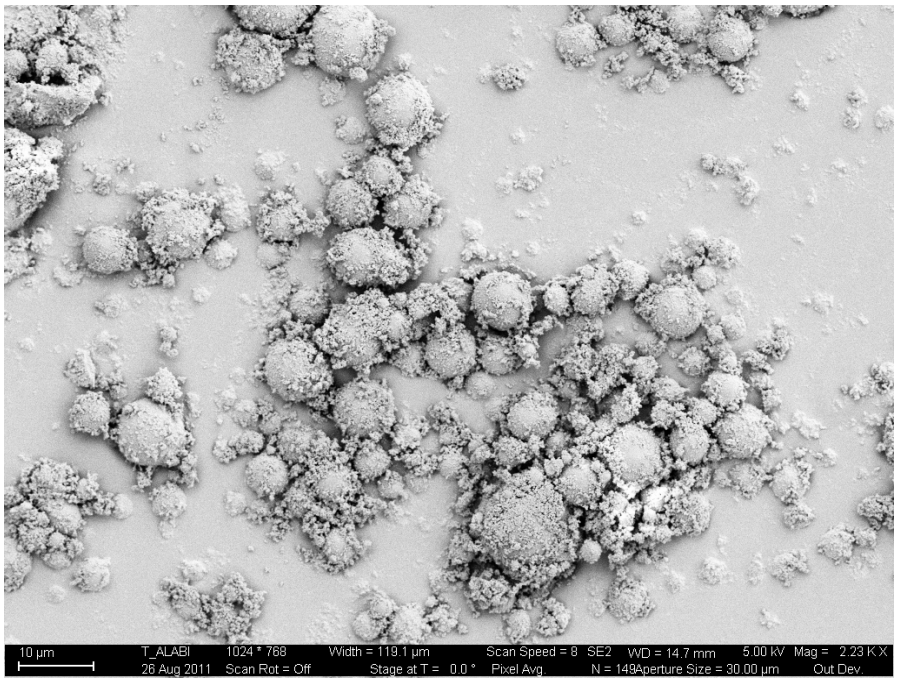

Figure 2.1: SEM micrograph of Tecosphere Microdust spherical silica particles with a mean diameter of 5µm.

2.1.3 Cure Depth Theory and Measurement

When a PCMS is exposed to light of an appropriate wavelength to form primary radicals, the system polymerizes by the mechanisms outlined in the previous section. Polymerization initiates the formation of a solid insoluble network, where the degree of monomer conversion is highest at the surface exposed to light and decreases with depth into the resin. The thickness of the resultant polymer is related to a critical degree of polymerization at which the polymer network exceeds the gel point and forms a solid

[16]. The most common relationship between cure depth and light exposure is the Jacobs equation, which is derived from an extension of the Beer-Lambert law [13, 21].

$$I(x,y,z) = I(x,y,0)\, exp\left(-\frac{z}{D_p}\right) \tag{2.8}$$

$$C_d = D_p \ln \frac{E}{E_c} \tag{2.9}$$

$$E = I_o * t \tag{2.10}$$

In equation 2.8, I(x,y,z) is the light intensity, typically in W/cm^2 or mW/cm^2, at any point within the photocurable resin, I(x,y,0) is the intensity distribution at the surface of the resin, z is the depth into the resin and D_p is known as the resin sensitivity or penetration depth. The resin sensitivity can be understood as the depth within the resin at which the energy dose is attenuated to e^{-1} of the incident dose. In equation 2.9, the depth, z, into the resin was replaced with the cure depth C_d, where the cure depth is described in terms of the energy dose incident to the surface of the resin, E, and the minimum or critical energy dose required to cause curing, E_c. The energy dose, typically in mJ/cm^2, depends on two parameters, which are the intensity of the light source on the resin surface, I_o, and the time for which the light source is incident on the resin surface, t, which is shown in equation 2.10.

The resin sensitivity and the critical energy are regarded as the fundamental parameters of the material system and are generally assumed to be independent of light intensity. These parameters can be experimentally determined through a plot of the cure depth versus the natural logarithm of exposure dose. This plot is a linear regression of the cure depth measurements, which is known as the "working curve." Figure 2.2 shows the working curve for PCMS used in LAMP. From the working curve plot, the resin sensitivity can be determined as the slope of the linear fit and the critical energy can be

obtained from the x-intercept. For the PCMS formulation studied in this thesis, the resin sensitivity was found to be 211±1.3 μm and the critical energy was 131.5±5.3 mJ/cm^2 with a 95% confidence interval.

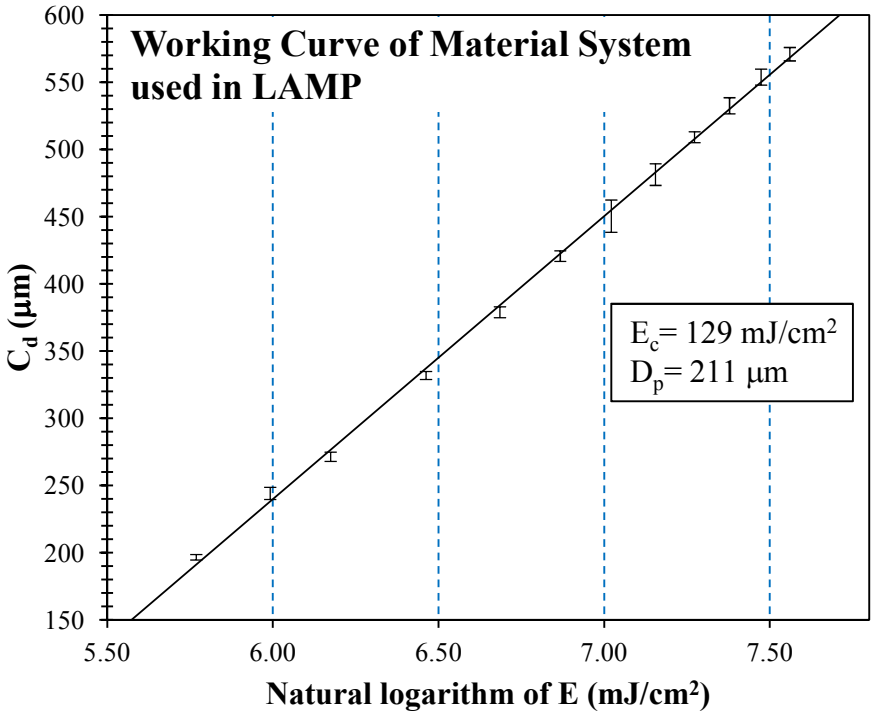

Figure 2.2: Working curve obtained from cure depth measurements of the material system used in LAMP.

Figure 2.3 shows a schematic of how cure depth samples were prepared. A UV transparent glass slide was placed on the surface of the photocurable ceramic-loaded material system and the exposure head introduced a uniform intensity of UV light onto the resin. The intensity from the UV source was determined to be 1.6W/cm^2 and the exposure dose was adjusted by selecting exposure times between 200ms and 1200ms to produce cured samples of different thicknesses. The solidified polymer network adhered to the glass, which enabled the removal of the cured sample from the uncured monomer. Residual monomer was rinsed from the glass slide and cured samples with isopropanol.

After development, the thicknesses of the samples were measured using a micrometer. Results from this procedure reliably produced cure depth measurements within a range of 5μm from the average cure depth.

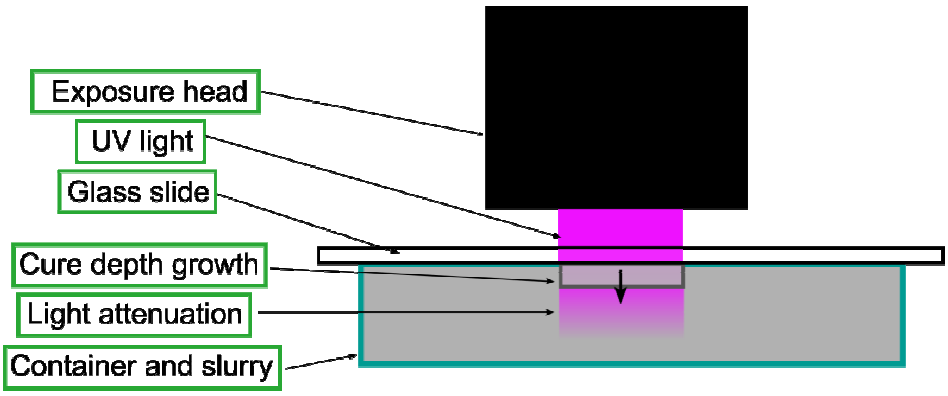

Figure 2.3: Schematic of the setup for the determination of cure depth.

While this procedure for determining the working curve is a powerful experimental method for predicting the cure depth for a particular exposure time from a specified light source, the resin sensitivity and critical energy cannot provide predictions of the cure depth when the composition or concentration of the material system is altered. As a result, numerous studies both theoretical [22] and numerical [23] have been conducted to develop a more powerful method for predicting the cure depth. The focus of this work will consider the theoretical aspects and the development of a compact model to predict the cure depth resulting from grayscale exposure. Tomeckova and Halloran developed a model [24] for the prediction of the resin sensitivity and critical energy in ceramic loaded resins. In this model, the resin sensitivity equation was described in terms of attenuation length contributions of the photoinitiator and UV absorber and scattering length contributions of ceramic particles as shown in equation 2.11 [24].

$$\frac{1}{D_p} = \frac{1}{l_{sc}} + (1 - \Phi)(c_P \varepsilon_P + c_A \varepsilon_A) \quad 2.11$$

Here, l_{sc} is the term that incorporates all the physics resulting from light scattering, Φ is the ceramic volume fraction, c is the concentration and ε is the extinction coefficient of the photoinitiator, P, and UV absorber, A. The monomer component is not included in this model since the monomer is relatively transparent to UV light. In addition to the resin sensitivity, Tomeckova and Halloran also modeled the critical energy based on inhibitor exhaustion [25]. In this model, the concept is put forth that the number of radicals generated per unit volume must equal the number of radicals depleted by inhibitor species. Once inhibitors have been exhausted, polymerization proceeds. Inhibitor species are intentionally placed in the material system to prevent polymerization during shipping and storage. Additional inhibitors are oxygen, and UV absorbers. Equation 2.12 shows the formula for critical energy based on the inhibitor exhaustion model [25].

$$E_c = (1 - \Phi)\frac{h\nu}{\Omega}\left(\gamma_Q Q + \gamma_O O + \gamma_A A\right)\frac{1}{c_P \varepsilon_P} \quad 2.12$$

Where h is Planck's constant, ν is the frequency of the light source, and Ω is the number of radicals created per absorbed photon. Also, Q, O and A are the concentrations of the added inhibitors, oxygen, and UV absorbers and γ_Q, γ_O, and γ_A are the number of radicals depleted per inhibitor, oxygen, and absorber molecules. This extension of the curing parameters of the working curve enables the prediction of cure depth for a wide range of material compositions and concentrations.

2.1.4 Fourier Transform Infrared Spectroscopy

In addition to cure depth measurements, characterization of the degree of polymerization is important to understand volumetric shrinkage and mechanical properties of the cured polymer. Determination of the degree of polymerization can be successfully characterized with Fourier Transform Infrared (FTIR) spectroscopy by measuring the degree of monomer conversion [26]. FTIR is a powerful tool to analyze the various chemical species and bonds within a molecule. Figure 2.4 shows the working principles of FTIR operated in Attenuated Total Reflectance (ATR) mode. In FTIR-ATR, an infrared beam enters a crystal with a high refractive index at a specified angle. An evanescent wave enters the investigated sample to a depth ~0.5μm to 5μm. Based on the molecular structure of the investigated sample, infrared radiation is absorbed at wavelengths unique to the sample investigated. This acts as a molecular "fingerprint," where the spectrum of the investigated sample can be compared to other known chemical compositions. After absorption, the attenuated infrared signal exits the crystal and is analyzed by the detector.

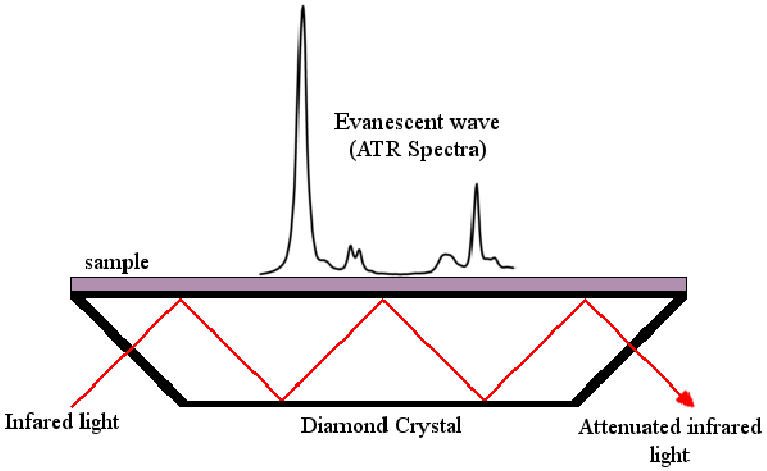

Figure 2.4: Schematic of Fourier Transform Infrared (FTIR) spectroscopy operated in Attenuated Total Reflectance (ATR) mode

The use of FTIR spectroscopy was shown to be an effective method for determining the degree of monomer conversion [26]. In LAMP, Hexanediol diacrylate (HDDA) is the primary acrylate monomer utilized for free radical polymerization. During polymerization, the carbon double bonds in the monomer are converted to single bonds and this change can be monitored using FTIR. Figure 2.5 shows the FTIR-ATR spectra of the PCMS for LAMP studied in this thesis. The region from 1600-1660cm^{-1} is characteristic of C═C stretching and the region from 1400-1430cm^{-1} is characteristic of C═C twisting. Samples are prepared in a similar manner to cure depth samples and the degree of conversion is measured at the surface incident to the light sourced. As the exposure time increases it is observed that these C=C stretching and twisting modes decrease, indicating that the carbon double bond conversion decreases due to the formation of polymer chains. During chain propagation, the spectral feature at 1750cm^{-1} was observed to remain constant and was identified as C═O stretching [9]. This feature serves as an internal reference to quantify the degree of carbon double bond conversion. Calculation of the degree of conversion can be accomplished by determining the difference in areas of the stretching and twisting features at specified exposure times with the unexposed areas and by normalizing the difference with respect to the area from C═O stretching.

$$\alpha(t) = \frac{\left[\frac{Area_{1620} + Area_{1410}}{Area_{1750}}\right]_0 - \left[\frac{Area_{1620} + Area_{1410}}{Area_{1750}}\right]_t}{\left[\frac{Area_{1620} + Area_{1410}}{Area_{1750}}\right]_0} * 100 \qquad 2.13$$

Here, α(t) is the degree of conversion and it quantifies the percentage of monomer disappearance, which can be used to characterize the degree of polymerization. Although this measurement cannot provide information regarding the molecular weight of the

polymer, it is nevertheless a powerful tool for predicting properties such as volumetric shrinkage [9], hardness [27] and viscosity [28].

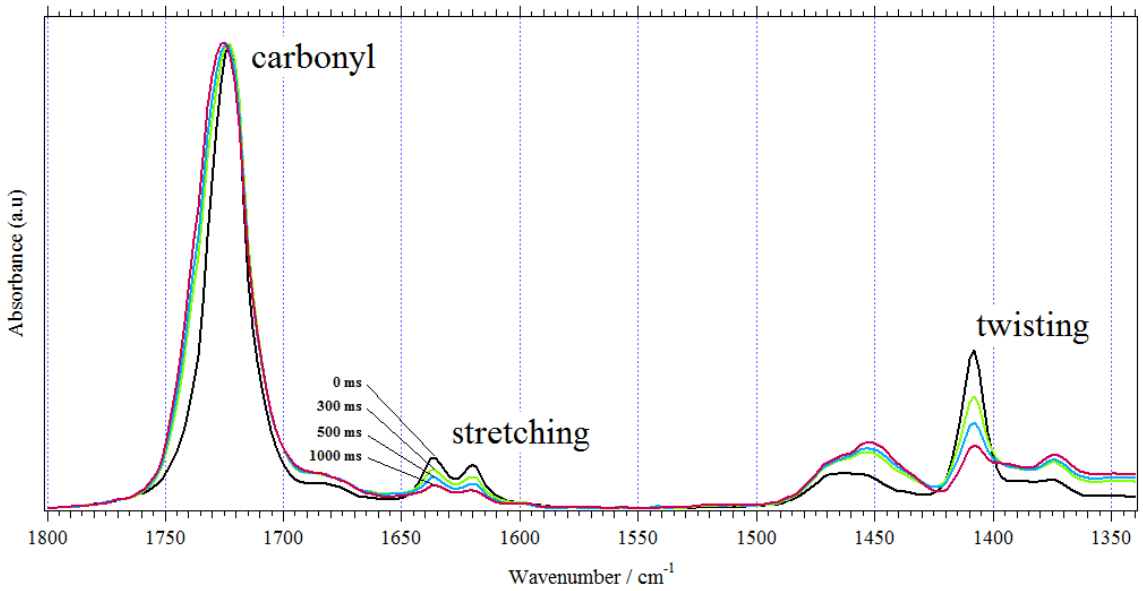

Figure 2.5: FTIR spectra of the photocurable material system used in LAMP illuminated with UV light for increasing exposure times.

2.2 Review of Grayscale Techniques and Exposure

With the advent of digital mask projection being utilized in additive manufacturing technologies, techniques used in printing to produce grayscale images became viable options for producing "masks" that incorporate grayscale exposures. In conventional stereolithography, a single laser beam is used to raster scan an entire layer. Consequently, the light intensity distribution incident on the surface of the resin is set at the maximum achievable resolution during fabrication, which is the diameter of the laser beam. However, maskless UV curing allows the simultaneous exposure of a large area. In this scenario, the light intensity distribution incident on the surface can be modified based on the white pixels loaded onto the SLM.

2.2.1 Techniques for Producing Grayscale Exposure

Grayscale exposure was first incorporated into hard masks for photolithography [29]. Hard masks contain two types of grayscale masks, which are continuous [30] and pixelated [31]. Similarly, in maskless projection there exist continuous [32] and pixelated grayscale exposures [11]. Continuous maskless grayscale exposure can be obtained by rapidly switching the pixel on and off during the exposure time [21]. In pixelated grayscale exposure, the grayscale exposure image is converted into a distribution of black (unexposed) and white (exposed) pixels. This technique is similar to that used in the printing industry and is referred to as screening where the grayscale image is obtained through "half-tone" unit cells.

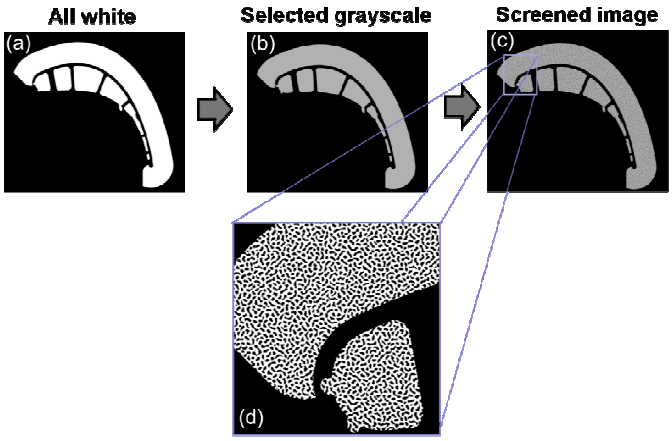

Figure 2.6: Schematic of the process to convert an image from an all white exposure to a grayscale exposure. (a) is the original image, (b) is the image where a grayscale value is selected, (c) shows the grayscale image converted to a distribution of black and white pixels, which appears very similar to the grayscale image. However, (d) shows a closer inspection of the pixel distribution to reveal the screening technique.

An example of the screening process is shown in Figure 2.6. The image in (a) represents the original image, (b) shows the image converted a grayscale level between 0 and 255, and (c) shows the screened image. When the pixel size is under a certain size,

the image appears to be a uniform shade of gray, yet in (d) it is shown that the gray image was accomplished by a distribution of black and white pixels.

Conventionally, gray levels are defined as the percentage of black pixels per unit area. However, the convention for this study is defined in terms of the percentage of white pixels per unit area, as this enables a direct proportionality to the energy dose delivered to the material system. Gray levels can be defined from 0 to 255 where 0 corresponds to black, 1-254 are shades of gray and a value of 255 is white. Two factors important for screening a grayscale image are pixel size and distribution. A large pixel size has a low screening resolution and will tend to appear pixelated instead of as a grayscale value. The pixel distribution describes the screening technique, which can control Moiré patterns. Figure 2.7 shows different screening techniques to produce the same grayscale value of 50% white. The image in (a) shows the use of a high screening resolution with a proprietary random screening technique, (b) shows the use of a lower screening resolution using the same screening technique, while (c) shows the use of an ordered screening technique at a similar screening resolution.

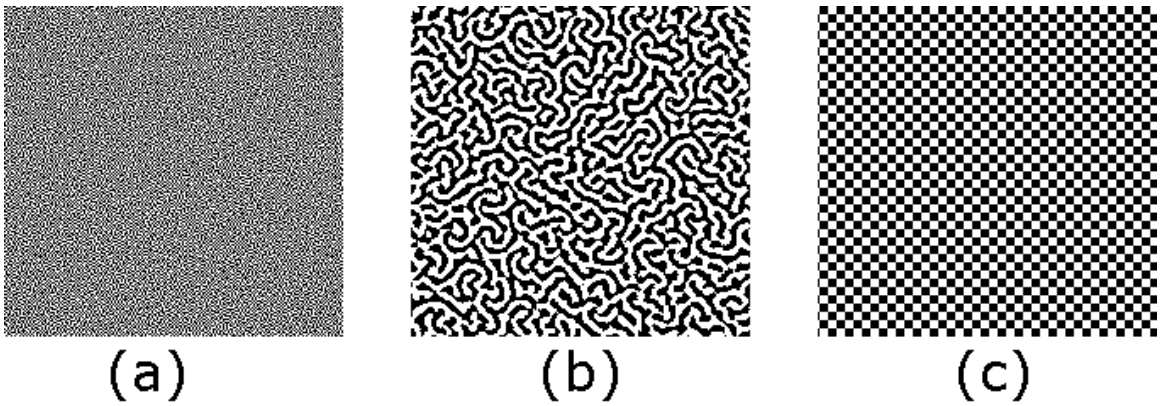

Figure 2.7: Examples of different screening techniques for an identical gray level of 50% white. (a) has a high screening resolution randomly distributed, (b) has a low screening resolution randomly distributed and (c) has an ordered low screening resolution.

2.2.2 Modulation of Light Intensity and Homogeneity

In previous investigations, grayscale exposure was applied to material systems without the incorporation of composites [11, 32, 33]. In these reports, grayscale exposure was modeled as a reduction in light intensity and the material properties were assumed to depend only on the exposure dose and not on the modulated light intensity. However, this assumption was not experimentally verified. In an investigation conducted by Atencia et al. [11], grayscale exposure using binary grayscale masks was explored. In this report, a homogenous transition was described where smooth features arise from a pattern of exposed and unexposed regions to produce an effective grayscale exposure. The homogenous transition was found to depend on the product *na,* where *n* is the number of transparent pixels per unit area and *a* is the side length of the pixel. Conceptually, if *a* is large, then the number of possible pixels per unit area is reduced and if *a* is small, then *n* can be increased. When *na* is greater than a critical value, the material system was cured with an effective grayscale exposure, and if *na* was lower than another critical value, the material system would form discrete features. The range of *na* between the homogenous and discrete critical values was defined as the homogenous transition. Atencia et al. put forth a detailed analysis of the parameters necessary to generate homogenous films from pixelated grayscale images, but little explanation was put forth to describe why the transition occurred at the experimentally determined values.

2.2.3 Applications of Grayscale Exposure

The use of grayscale exposure has received greater attention in recent years [21, 32, 34]. The primary motivation is due to the ability to control the light intensity distribution within a single exposure. As a result the cure depth can be controlled and

three-dimensional patterns can be generated within a single layer using a constant exposure time. This was tremendously useful in the fabrication of microlenses, which enabled the formation of a smooth curved surface resulting from one exposure [33]. Grayscale exposure was also applied to the microfluidics field to create fine point microneedles and microchannels of variable height within a single exposure [11]. More recently grayscale exposure was explored in micro-stereolithography to fabricate geometries with unsupported structures by incorporating grayscale exposure to the uncured surroundings [32]. As a result, a partially polymerized grayscale support structure was able to be selectively etched away to reveal a fully polymerized and accurately built structure. To date, the effects of grayscale exposure have not been explored for ceramic-loaded photocurable material systems. Additionally, grayscale exposure has primarily been used for micro-scale applications. This study aims to address grayscale exposure in ceramic-loaded material systems and to investigate its applicability to larger length scales.

2.3 Stress Relief and Characterization

During photopolymerization of acrylate monomers, volumetric shrinkage of around 10% is commonly observed [9]. When the monomer being polymerized is in contact with another material, stress develops between the two materials. Shrinkage stress has been studied extensively by the dental community due to the use of resin composites as dental restorations [35-38]. Interestingly, it was found that shrinkage stress depends not only on the degree of conversion, but also on the conversion rate. Emami reports that shrinkage stress was dependent on the intensity of the light source causing photopolymerization [39]. However, at a high energy dose, the volumetric shrinkage and

Young's Modulus was independent of the light intensity and only dependent on the energy dose. These results show that stress development during photopolymerization is not solely dependent on the volumetric shrinkage, but also on the shrinkage rate. The common explanation put forth is that the gel point is delayed and shrinkage at the bonded surface is compensated with viscous flow and relaxation [40, 41].

As a result, FTIR measurements can be used to characterize the polymerization stress that develops during UV exposure. Both the degree of conversion and the rate of conversion must be characterized to determine stress reduction. The rate of conversion can be obtained by taking the derivative of the degree of conversion versus exposure time plot. Stress reduction by grayscale exposure can be observed by determining which grayscale level provides the greatest reduction in rate of polymerization. FTIR can also be used to characterize stress relief associated with screening resolution selection. By keeping the grayscale level and exposure dose constant and by varying the screening resolution, the effect of screening resolution on stress relief can be determined. If the degree of conversion of one screening resolution is low compared to another, then it can be concluded that the shrinkage was reduced.

When considering mitigation of stresses in LAMP, reducing the light intensity through grayscale exposure promises to be a viable method of reducing internal stresses which develop between layers. However, reducing the light intensity increases the time required for a given energy dose and cure depth. An alternative technique to reduce stress is the use of structured patterning [42]. Ganahl showed that shrinkage stress can be reduced by designing exposure masks to create regions of uncured monomer [42]. It was found that an optimal range of exposed line width and spacing provided the greatest

stress relief for single layer exposures. The explanation provided for the observed stress reduction was the migration of monomer from the unexposed regions to the exposed regions, which helped reduce volumetric shrinkage. When considering the application of the work conducted by Ganahl to stress reduction in LAMP through grayscale exposure, attention must be given to the screening resolution. If the screening resolution is too low, monomer migration may be hindered and if the screening resolution is too high, diffraction and scattering may cause polymerization in the unexposed regions.

CHAPTER 3

OPTICAL ANALYSIS OF MASKLESS PROJECTION

Chapter 3 investigates the averaged effects of light intensity projected by the UV light source as well as the local light intensity distribution resulting from various pixel distributions. Section 3.1 examines the ability of grayscale exposures to produce an averaged modulation of light intensity. Section 3.2 investigates the light intensity resulting from a single pixel and a collection of pixels through optical profiling. Results from Section 3.2 are discussed in Section 3.3 and assumptions regarding the light intensity distributions are made.

The light source used in LAMP is a high pressure mercury vapor lamp. The emission spectrum of the light source is shown in Figure 3.1. There are three distinct regions of emission from the light source, which are the I-line at 365nm, H-line at 404.7nm and G-line at 435.8nm. For this light source the G-line is the strongest spectral feature, followed by the H-line and I-line, respectively. It is important to note that the primary peak utilized for photopolymerization is the I-line, since the photoinitiator utilized exhibits negligible absorption for the longer wavelengths [43].

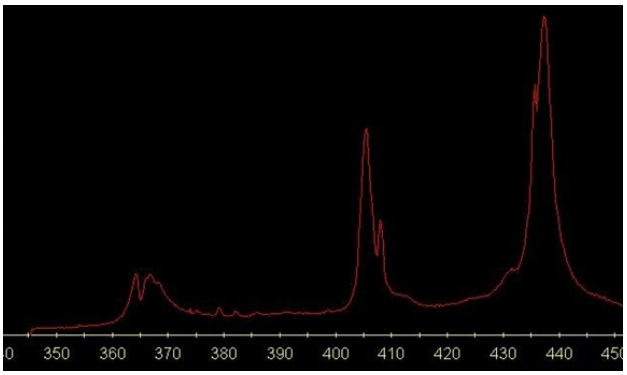

Figure 3.1: Spectrum of high pressure mercury vapor lamp [44]

3.1 Determination of the Grayscale Factor

Previous investigations conducted on grayscale exposures propose that the light intensity incident on the surface is effectively reduced [11]. This can be characterized by a "grayscale factor," g, which relates the averaged grayscale light intensity to the "all white" light intensity and can be described by equation 3.1.

$$g = \frac{I_{gr}}{I_o} \tag{3.1}$$

Where I_{gr} is the averaged light intensity incident on the PCMS resulting from a half-toned grayscale exposure, and I_o is the light intensity resulting from a full exposure, where every pixel on the DMD is turned to the on position. Intuitively, the grayscale factor could be assumed as being equal to the grayscale value of the image, i.e. the percentage of white pixels in the designed image, G, and independent of the pixel distribution. This assumption was tested and the results are shown in Figure 3.2.

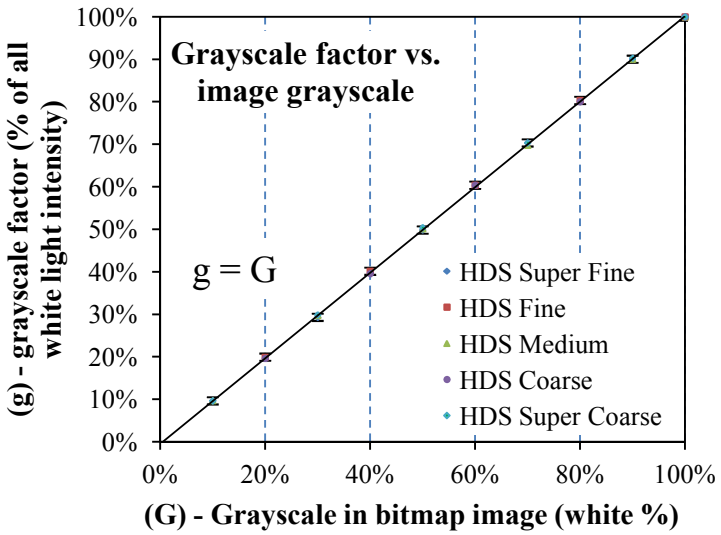

Figure 3.2: Comparison of the grayscale factor resulting from a screened grayscale image at different screening resolutions

The grayscale factor was determined using a photodetector provided by the supplier of the optical scanning system. First, the current from a full projection was measured, which corresponds to the total light power delivered to the photodetector. The exposure area was held constant throughout the experiment to give a direct relationship to the light intensity. Next, the current resulting from projected grayscale images at different screening resolutions and grayscale values was measured. The screening process was accomplished using Harlequin RIP by Global Graphics, details can be found elsewhere [45]. The screening technique used was Harlequin Dispersive Screening (HDS), which is a proprietary screening technique. Screening resolutions were varied from HDS super fine to HDS super coarse; here HDS super fine has the highest screening resolution (1x1 pixel half-tone cells) and HDS has the lowest screening resolution (4x4 half-tone cells). Examples of HDS screening were shown in Figures 2.5 (d) and 2.6 (a) and (b). The grayscale factor was determined by dividing the grayscale current by the full exposure current. The error associated with this measurement technique was determined to be ±1%. Results show the validity of the assumption that the grayscale factor, g, is equivalent to the grayscale of the projected image, G. From Figure 3.2, the slope and intercept of the linear fit were found to be 1.004 and -0.003, respectively. Considering the error in the experimental procedure, it is reasonable to assume a slope of ~1 and intercept of ~0. From this experiment, it can be concluded that the average grayscale light intensity incident on the surface of the PCMS, I_{gr}, is equal to the all white light intensity multiplied by the grayscale value of the projected image, G. This result is summarized by equations 3.2 and 3.3.

$$g = G \tag{3.2}$$

$$I_{gr} = I_o G \tag{3.3}$$

3.2 Light Intensity Distribution Characterization

In addition, to the averaged effects of grayscale exposure, it is also important to consider the "true" distribution of light intensity projected onto the PCMS. This was accomplished through the use of a charge-coupled device (CCD) BeamGage® Laser Beam Measurement system supplied by Ophir-Spiricon to measure the light intensity distribution. The spectral range of this profilometer is 190-1320nm with ±1% linearity with power. The size of each pixel in the CCD is 4.4μm, which enabled sub-pixel level measurement of the SLM light output. The profilometer provides information about the optical profile in counts per second per pixel, which is analogous to light intensity. With this setup, the light intensity distribution can be determined. However, due to the lack of a calibration system, the actual magnitude of the light intensity at each individual pixel cannot be directly determined. This limitation can be overcome by measuring all optical profiles under identical conditions and camera settings to enable the determination of trends in the light intensity distribution of different pixel patterns.

Figure 3.3a shows the light intensity distribution at the focal plane resulting from one pixel of the DMD being projected. The top panel shows the light intensity plotted in the x-y plane, which is parallel with the PCMS surface, where reds correspond to high light intensity and blues correspond to low light intensity. Previous reports have described the intensity distribution for a single pixel as Gaussian [21].

$$I(x,y) = I_o e^{-\frac{(x^2+y^2)}{r^2}} \tag{3.4}$$

where I_o is the peak light intensity and r is the Gaussian radius.

The bottom panel of Figure 3.3a shows a plot of the cross-sectional profile of the projected pixel. The curve fit shown in the profile was obtained through a two-dimensional Gaussian regression. From this regression, the Gaussian radius was determined to be ~8.3μm, which is consistent with a pixel resolution of 17μm. The maximum measured value of intensity for a single pixel exposure was 3601counts/px-sec. The statistical error from the measurement was determined to be ±85 counts/px-sec and the horizontal error bars show the dimensions of the CCD for which the data points were averaged. In order to better understand the light intensity distributions resulting from SLM projections, additional pixel patterns were investigated. Figures 3.3b-f shows the intensity distributions and profiles of 2, 3, 4, 5 and 10 pixel lines, respectively. Sun et al. also suggest that projections of additional pixels can be treated as the sum of Gaussian intensity distributions [21]. Therefore, each distribution was regressed as a summation of 2, 3, 4, 5, and 10 two-dimensional Gaussian distributions, respectively. The averaged Gaussian radius from all the projections investigated was 8.6μm with a standard deviation of 1μm. However, additional trends are observed that a superposition of Gaussian distributions with a constant radius could not describe. In Figure 3.3f, trends in the valleys can be seen, where a minimum is reached in the center of the 10 pixel line, which can be attributed to diffraction. This indicates that a more detailed optical analysis is required. However, conventional techniques for modeling cure depth in stereolithography use the peak intensity of the laser to predict the cure depth [13]. Therefore, for this study it is sufficient to assess the trends in peak intensity resulting from the various intensity distributions. From these experiments, it can be seen that the

peak intensity remains constant with each of the lines investigated. The maximum intensity measured from the 10 pixel line was 3683 counts/px-sec, which shows an increase of only ~2% from that for a single pixel projection.

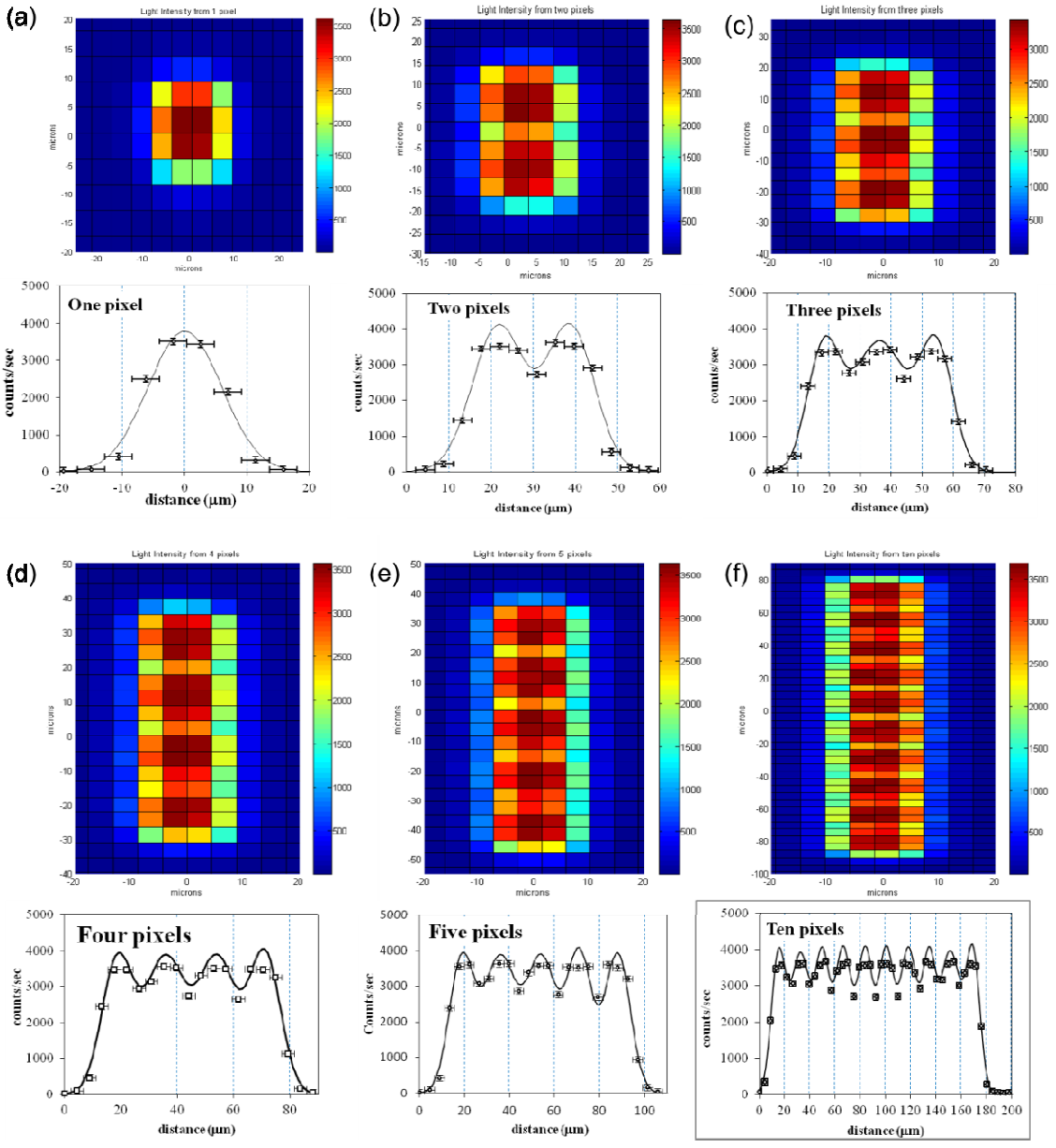

Figure 3.3: Intensity distributions and profiles for (a) 1 pixel, (b) 2 pixel, (c) 3 pixel, (d) 4 pixel, (e) 5 pixel, and (f) 10 pixel line projections from the SLM.

The above results suggest that the pixel distribution has little effect on the peak light intensity. In an effort to verify this, all the pixels of the SLM were projected. A profile of this exposure is shown in Figure 3.4. The maximum intensity was found to be 3959 counts/px-sec, which indicates that the peak light intensity for single pixel exposure decreases only ~10% from that for a flood exposure. Additionally, Figure 3.4 shows the underlying complexity of the optical projection which is being neglected due to its negligible influence on the peak intensities. A periodic distribution in the intensity of the valleys is observed, which has a period of ~220μm and may be a result of diffraction.

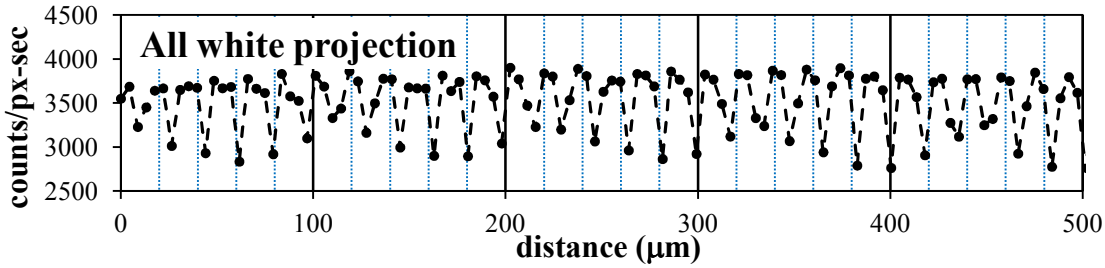

Figure 3.4: Light intensity distribution resulting from an all white projection.

3.3 Conclusions

From these experimental investigations, certain simplifying assumptions can be made into the optical characteristics. In Section 3.1 it was shown that projection of grayscale images effectively reduced the average light intensity by the grayscale value of the projected image. It was also shown that the screening resolution of the projected grayscale image has a negligible influence on the averaged light intensity. However, Section 3.2 showed that the peak light intensity remains relatively unaffected by the quantity and distribution of projected pixels. As a result, it can be assumed that the peak light intensity resulting from a single pixel is equivalent to the peak intensity measured from an all white projection, which was 1.6W/cm^2.

CHAPTER 4

EXPERIMENTAL CHARACTERIZATION OF GRAYSCALE EXPOSURE

Chapter 4 investigates the curing characteristics of grayscale exposure through cure depth measurements. Section 4.1 characterizes the reduction of cure depth resulting from grayscale images with a high screening resolution. The hypothesis that the grayscale exposure effectively reduces the light intensity experienced by the material system proportional to the grayscale value of the projected image is proposed. Section 4.2 characterizes the effects of a true reduction in light intensity to provide a comparison with grayscale exposures. Section 4.3 investigates the effects of grayscale exposure at high screening resolutions and the light intensity reduction hypothesis is assessed. Section 4.4 explores the effect of screening resolution on the cure depth and curing parameters. The spatial limits of grayscale exposure, full intensity exposure and the transition between the two modes are characterized.

4.1 Cure Depth Measurements of Grayscale Exposure

When considering grayscale exposure, the material system could cure according to the local, averaged or an intermediate light intensity incident to the surface. In chapter 3 it was shown that the distribution of projected pixels does not significantly alter the maximum incident light intensity. Therefore, if the cure depth resulting from grayscale exposure is similar to the cure depth resulting from an all white exposure, then it can be concluded that the PCMS cures according to the local light intensity. However, if the cure depth resulting from grayscale exposure is lower than the cure depth of an all white

exposure, then the curing behavior of the PCMS can be modeled as an effective light intensity reduction. To investigate the response to grayscale exposure, cure depth measurements were conducted at a fixed exposure time and screening resolution and the grayscale was varied from 30% to 90% white. The exposure time used was 600ms and the screening resolution was HDS super fine. The resulting films were homogenously smooth with no evidence of the pixel distribution utilized in the grayscale exposure. The cure depth measurements in Figure 4.1 clearly show that in addition to the homogeneity of the films produced from grayscale exposure, the cure depth decreases with a decrease in grayscale. This indicates that the light intensity has been effectively smoothed and reduced. From the findings in Figure 4.1, it can be hypothesized that grayscale exposure causes the PCMS to cure as though the light intensity was reduced in proportion to the grayscale value of the projected image. The validity and the limits of this hypothesis are the focus of the following sections.

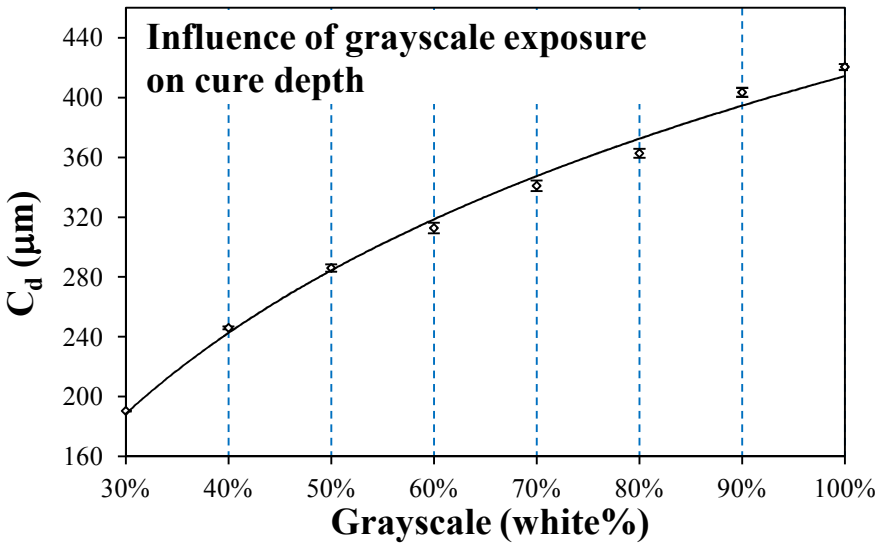

Figure 4.1: Cure depth measurements conducted at 600ms exposure time for grayscale exposures from 30% white to 100% white at a screening resolution of HDS Super Fine.

4.2 Working Curves for Different Light Intensities

Reports by Atencia et al. suggest that grayscale exposure with a sufficiently high screening resolution results in an effective reduction in intensity which corresponds to the grayscale of the projected image [11]. This result was summarized by equation 3.3. In order to relate the curing behavior to a grayscale light intensity, the effect of altering the "true" light intensity on the curing parameters must be determined. This was accomplished through the use of UV neutral density (ND) filters, which act to uniformly attenuate light intensity over a specified range of wavelength. UV-VIS ND filters of a nominal optical density (OD) of 0.3 and 0.5 were purchased from Edmund Optics to uniformly attenuate wavelengths from 200nm to 700nm. The transmission of the filters was measured using a technique similar to that used for determining the grayscale factor. First, an all white image was projected onto the photodetector and the resulting current was measured. Next, the ND filters were placed between the light source and the photodetector and the current from an attenuated all white projection was measured. The ratio of these two current measurements provides the transmission for each filter. The percent transmitted for the 0.3 and 0.5 OD filters measured were 56% and 32%, which corresponds to a light intensity of 896mW/cm^2 and 512mW/cm^2, respectively as compared to 1.6W/cm^2 for unfiltered light. To expose the PCMS to a reduced light intensity, the ND filter was placed on top of the glass slide as shown in Figure 4.2.

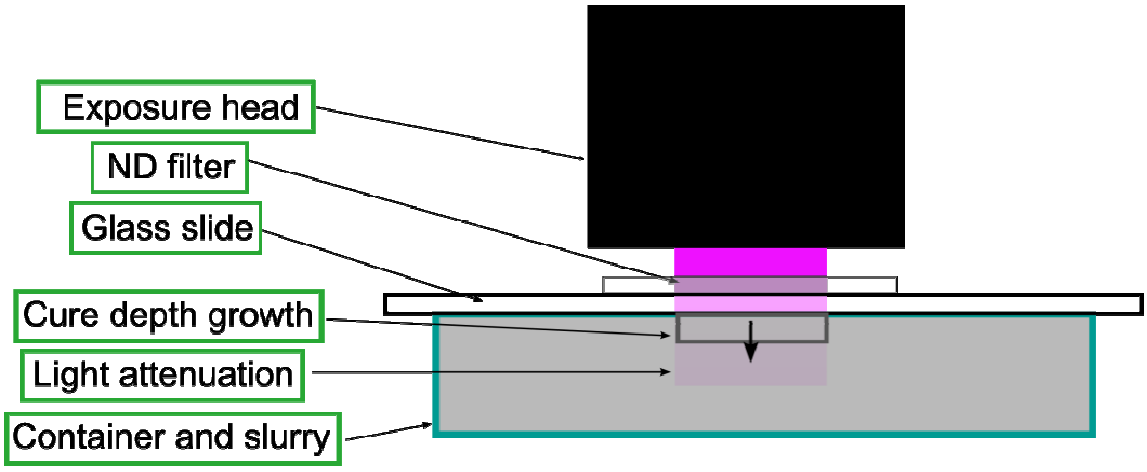

Figure 4.2: Schematic of cure depth measurements with the incorporation of neutral density filters to determine the curing characteristics at different light intensities.

Cure depth measurements were conducted for each of the different light intensities at multiple exposure times to develop working curves. The exposure times were selected to investigate a consistent range of energy dose for the different light intensities. Figure 4.3 shows the resulting working curves. The working curve resulting from an unfiltered light intensity of 1.6W/cm^2 is also shown for comparison. It can be seen that the cure depth for a constant energy dose increases when the light intensity decreases. As a result, the cure depth from the highest source of light intensity resulted in the lowest cure depth. Consequently, the critical energy decreases with a decrease in light intensity. While at first counterintuitive, it should be noted that for a constant energy dose, the exposure time must increase for a lower intensity, i.e. there is more time for photopolymerization to proceed. From Figure 4.3, it can also be seen that the slopes resulting from each light intensity curve remain constant, which indicates that the resin sensitivity has little dependence on light intensity under these exposure conditions.

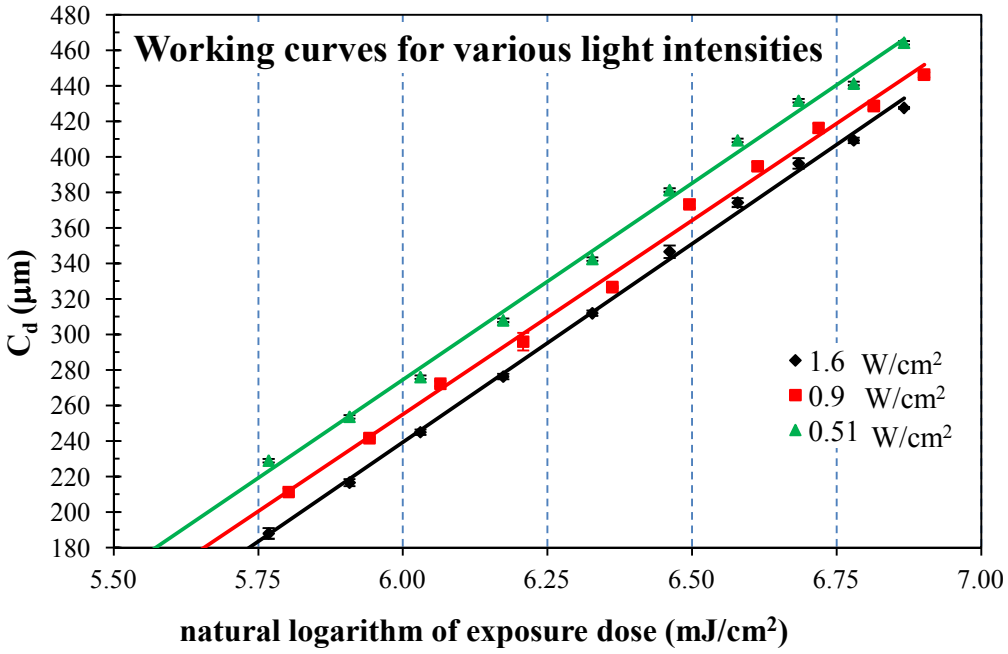

Figure 4.3: Working curves of the PCMS with exposure to different light intensities

Figure 4.4 shows a summary of the dependence of the critical energy and resin sensitivity on light intensity. The linear regression of the critical energy resulted in the following empirical relationship.

$$E_c = 18.31 * I + 109 \qquad 4.1$$

Where E_c is in units of mJ/cm^2, I is in units of W/cm^2 and the slope is in units of ms. From this regression, R^2 was determined to be 0.999. This indicates that the critical energy has a strong linear dependence with light intensity. It is important to note that neither the Jacobs' equation (eq 2.9) nor the inhibitor equation (eq. 2.12) predicts this behavior. Rather, both models assume that the curing parameters are constant for a given material system and independent of how the energy is delivered to the material system. Results from a linear regression of the resin sensitivity show a near horizontal slope,

indicating that the resin sensitivity is relatively independent of light intensity, which follows the Jacobs equation.

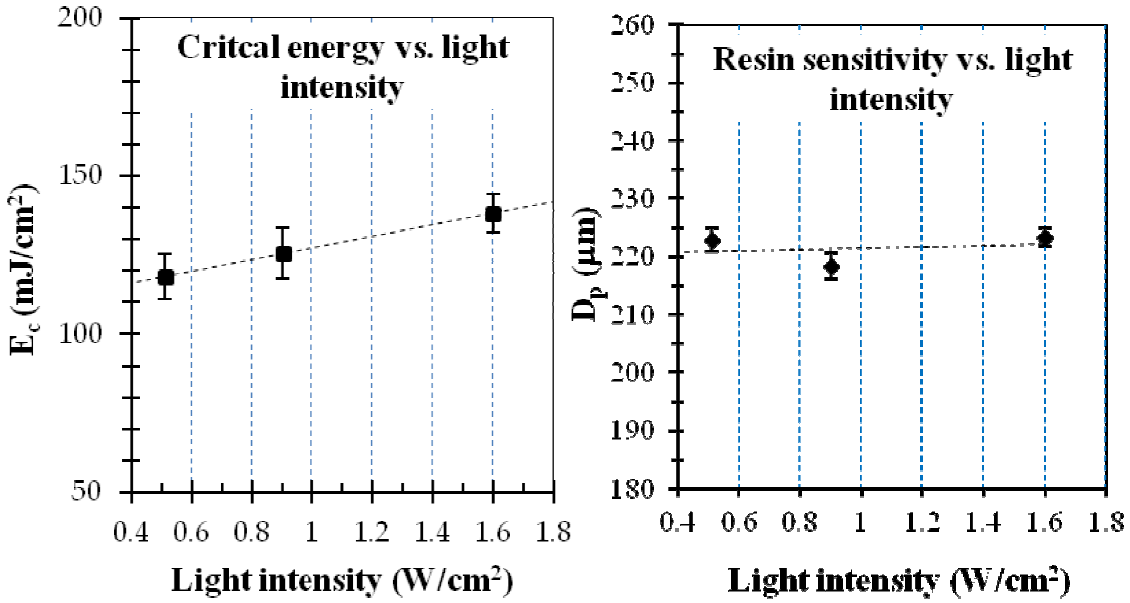

Figure 4.4: Summary of light intensity dependence of the curing parameters

4.3 Working Curves for Grayscale Exposure

For grayscale exposure to be equivalent to an effective reduction in light intensity proportional to the grayscale value of the projected image, trends observed with grayscale exposure must be similar to trends observed with true light intensity reduction, i.e. the critical energy should have a strong linear dependence with the grayscale factor and the resin sensitivity should be relatively independent of the grayscale factor. One method for evaluating the validity of the light intensity reduction hypothesis is to assume that the hypothesis is true and compare the behavior of the curing parameters resulting from grayscale exposure to the behavior observed for a true reduction in light intensity. If the behaviors are similar, then the light intensity reduction model can be used to predict the curing characteristics of grayscale exposure. To test this hypothesis, numerous grayscale

exposure cure depth experiments were conducted. Grayscale images from 20% to 90% white were designed at five different screening resolutions: HDS super fine, fine, medium, coarse and super coarse. Working curves for each of the grayscale values and screening resolutions were developed by measuring the cure depth at different exposure times. The range of energy dose investigated under the light intensity reduction hypothesis for each grayscale exposure was 320mJ/cm^2 to 1920mJ/cm^2. Figure 4.5 shows a sample of the working curves resulting from grayscales of 50%, 40%, and 20% white and with HDS super fine screening.

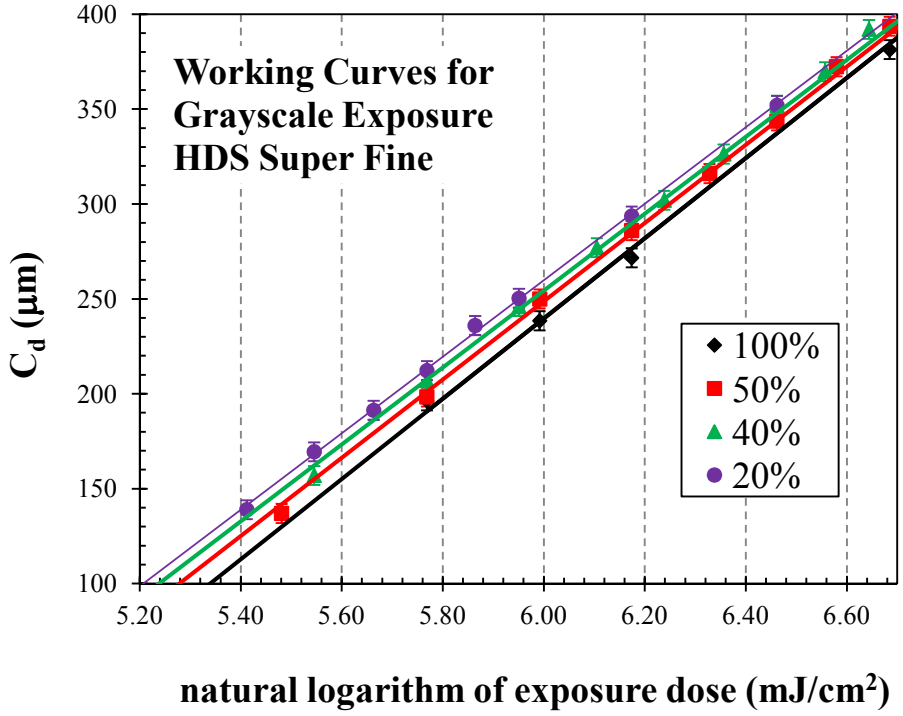

Figure 4.5: Working curves resulting from grayscale exposure of 50% (■), 40% (▲), and 20% (●) white at a screening resolution of HDS super fine. The working curve from a full exposure, 100% white (♦), is also shown for reference.

From Figure 4.5 trends similar to a true reduction in light intensity can be seen. As the grayscale decreases, so does the critical energy. This is evidenced by a shift in the x-intercept and an increase in cure depth resulting from an equivalent energy dose.

However, it can be noted that the resin sensitivity also shows a slight decrease with a decrease in grayscale, which deviates from the light intensity reduction hypothesis. This is evidenced by a decrease in the slope with a decrease in grayscale. These results suggest that the critical energy resulting from grayscale exposure behaves in a manner similar to a true reduction in light intensity. However, additional phenomena may affect the resin sensitivity since its trends deviates from a true light intensity reduction.

Through the continued investigation of grayscale exposures, it was found that the curing parameters showed similar trends for each screening resolution investigated. This is shown in Figure 4.6. Films of uniform thickness were produced for all the HDS screening resolutions investigated. At each grayscale value, similar values for the critical energy and resin sensitivity were obtained regardless of the screening resolution. This indicates that the PCMS behaves in a similar manner for a range of screening resolutions and that the intensity reduction assumption is valid for each screening resolution. Figure 4.6 quantifies the trends observed in Figure 4.5. It can be seen that a linear regression of the critical energy accurately describes the variation with grayscale, which is evidenced by the high R^2 values. This indicates that the critical energy for grayscale exposure at different screening resolutions varies in a manner similar to its variation with uniform light intensity. Additionally, a linear regression of non-horizontal slope accurately described the resin sensitivity, which deviates from the trends observed for varying light intensity. Since the trends in resin sensitivity and critical energy are within the error determined for each screening resolution, the results can be combined to obtain a better regression of the trends in curing parameters, which can help provide a better

understanding of the curing characteristics when homogenous films are produced from grayscale exposure.

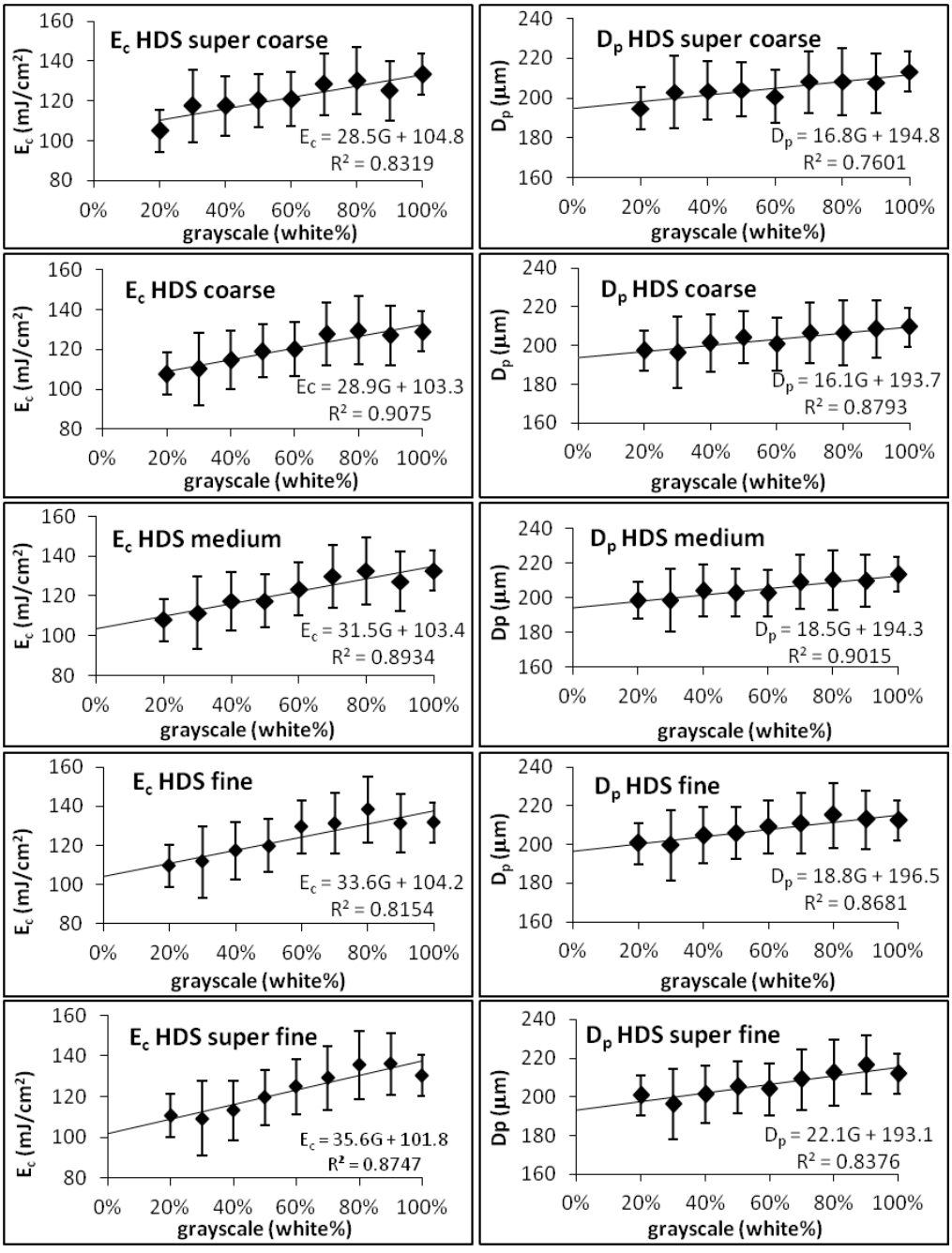

Figure 4.6: Summary of the critical energy and resin sensitivity for grayscales of 20% - 90% white with screening resolutions from HDS super fine to HDS super coarse.

The trends in curing parameters from homogenous grayscale exposure are shown in Figure 4.7. In this figure, the image grayscale was converted to its effective intensity in order to compare the results with the critical energies obtained from a true reduction in light intensity. Both the critical energies from grayscale exposure and true intensity measurements were plotted. From Figure 4.7 it can be seen that the grayscale exposure critical energies are within the error of the critical energies obtained from true intensity measurements. This shows that the critical energy resulting from grayscale exposure behaves as a true reduction in light intensity. The regression obtained for the influence of grayscale exposure on the critical energy was:

$$E_c = 19.6 * I + 103.7 \quad 4.2$$

Here, I was obtained by multiplying the all white light intensity by the grayscale of the image. The R^2 value obtained for this regression was 0.92, which indicates that the regression is a good fit of the data. Also, it can be noted that the slope with light intensity varies by only 1.3mJ/W and the critical energy at zero light intensity varies by only 5.3mJ/cm^2, which is within the average confidence interval of 5.6mJ/cm^2 obtained during the grayscale exposure measurements. In addition to E_c, the resin sensitivity also shows a strong linear dependence on light intensity.

$$D_p = 11.3 * I + 194.8 \quad 4.3$$

From this regression, R^2 was determined to be 0.94, which shows that the regression is an adequate representation of the influence of grayscale light intensity on the resin sensitivity.

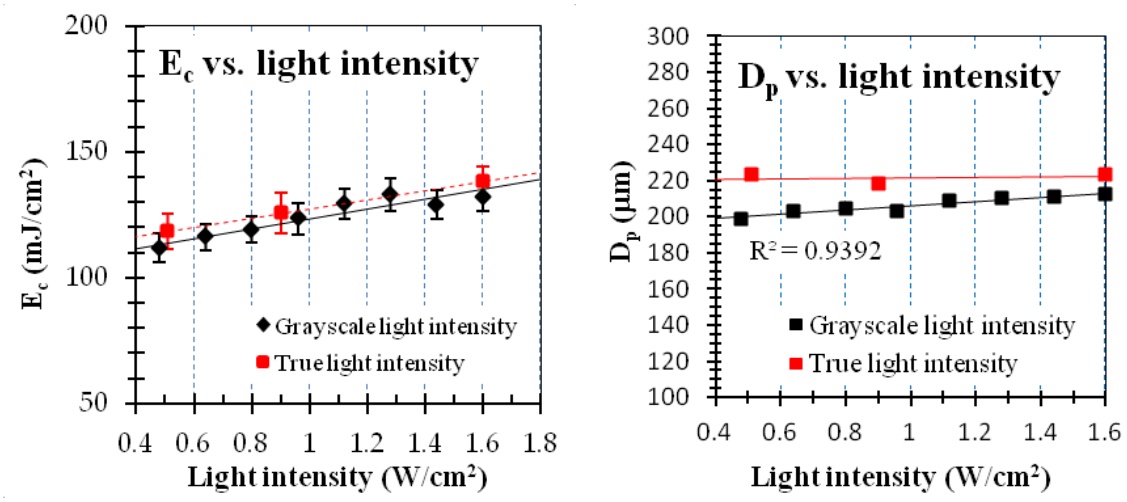

Figure 4.7: Summary of the influence of the light intensity on the curing characteristics resulting from homogenous grayscale exposure. The left panel shows the similar effect of a grayscale reduction in light intensity and a true light intensity reduction on the critical energy. The right panel shows the influence of grayscale light intensity reduction on the resin sensitivity.

4.4 Characterization of Homogenous Transition Exposure

In the present grayscale investigation, only the screening resolutions resulting in a homogenous film have been considered. However, intuitively if sufficiently large collections of exposed and unexposed pixels are projected onto the PCMS, film homogeneity will be lost and regions of cure depth with all white exposure will develop accompanied with regions of uncured resin. To date, few reports have characterized the cure depth within the homogenous transition. However, the homogenous transition is a region of interest in the investigation of methods to mitigate polymerization shrinkage stress. Reports by Ganahl show that for a given material system, there exist optimal dimensions of line width and line spacing to reduce the stress in a photopolymerized film [42]. It can also be noted that the films generated by Ganahl were not uniform nor were cured regions completely isolated from each other. Rather, the film contained regions of a larger cure depth connected by regions of partially cured resin with a lower cure depth.

This corresponds to the homogenous transition, which corresponds to dimensions of exposed and unexposed regions for which the material system cannot create distinct regions of cured polymer separated by distinct regions of uncured monomer. This spatial modulation of the degree of conversion reduced shrinkage stress in the material system investigated by Ganahl, which indicates that it may reduce shrinkage stress in the PCMS used in LAMP.

In order to incorporate features containing dimensions within the homogenous transition in multilayer builds, the cure depth must be predicted to ensure proper binding to the previous layer. The investigation of the homogenous transition was accomplished through the selection of one grayscale value. Also, the screening technique was converted to a well-defined pattern in order to easily extract dimensional information. The pattern chosen was a "checkerboard," which is shown in Figure 4.8.

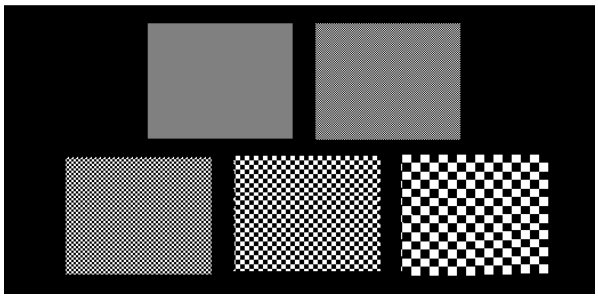

Figure 4.8: The screening technique used to investigate the homogenous transition. A checkerboard pattern was selected to enable a direct method for determining dimensional information.

The checkerboard pattern consists of alternating squares of exposed and unexposed regions. To investigate the influence of screening resolution, the length of the square primitive was successively increased. The range of square lengths investigated was from 1 pixel to 80 pixels, which corresponds to 17μm to 1360μm. Each checkerboard pattern has an image grayscale value of 50%. However, as the screening

resolution decreases, the image visually appears less gray and more as a pattern of distinct black and white squares. Similarly, as the screening resolution decreases, the light intensity reduction assumption of grayscale exposure breaks down.

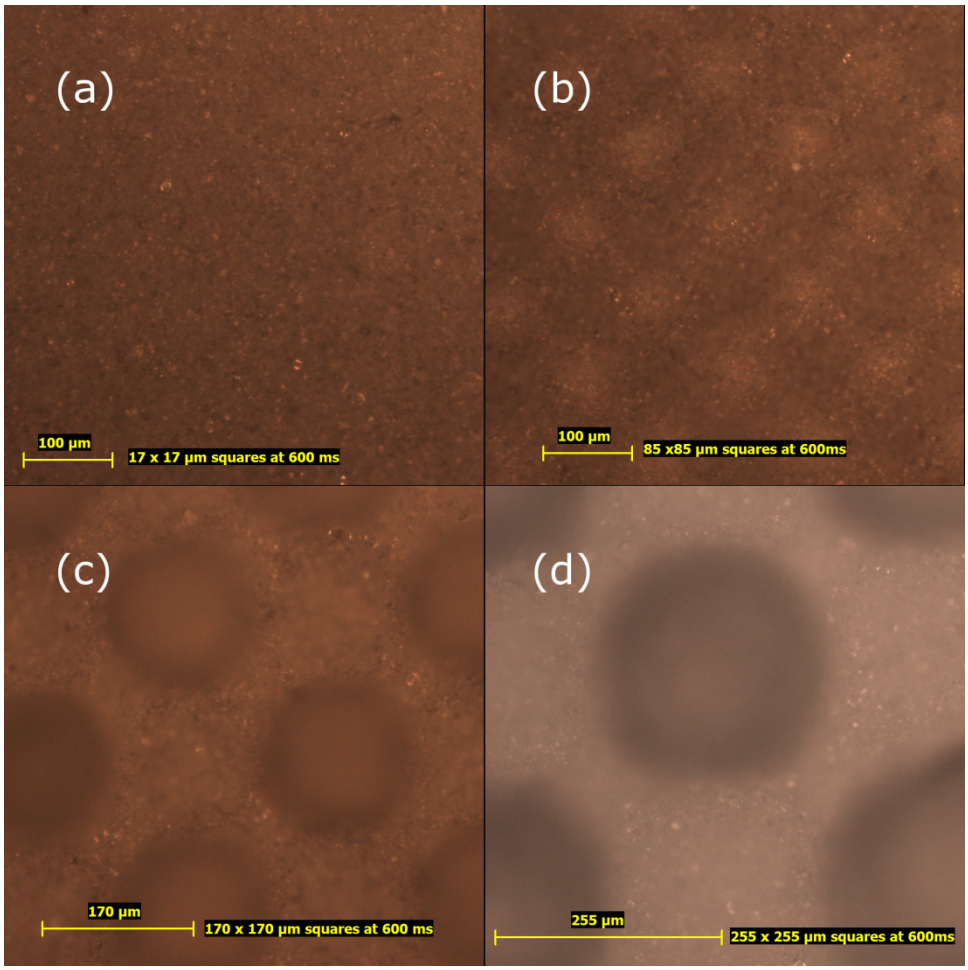

Figure 4.9: Images of checkerboard exposure at 600ms with squares lengths of (a) 17µm, (b) 85µm, (c) 170µm, and (d) 255µm to show the homogenous transition.

Images in Figure 4.9 show the homogenous transition for a 600ms exposure. It can be seen in (a) that a checkerboard exposure with a square length of 17µm results in a film with uniform thickness. However, when the square length reaches 85µm in (b), inhomogeneities in the film thickness are observed. This represents the onset of the homogenous transition. Images (c) and (d) depict the continued deviation from

homogeneity for square lengths of 170μm and 255μm. As the homogenous transition progresses, the cure depth of the exposed regions increases and that of the unexposed regions decreases.

When characterizing the effect of the homogenous transition on the cure depth, it can be seen in Figure 4.10 that the homogenous transition separates two regions of constant and homogenous cure depth. The region with lower cure depth occurs when square length of the checkerboard exposure pattern is small, which corresponds to grayscale exposure. The region with a higher constant cure depth is from an all white exposure. These two regions are separated by the homogenous transition where the cure depth increases as the square length of the checkerboard increases for a given exposure time. One interesting aspect of the results shown in Figure 4.10 is the shifting of the homogenous transition to the right with an increase in exposure time. The center of the sigmoid regression increases with an increase in exposure time to larger square lengths. The center of the 200ms exposure time was at a square length of 172μm, while the center of the 900ms exposure was at a square length of 330μm. From these cure depth measurements, it was observed that the average square length range of the homogenous transition was from ~100μm to 450μm.

This time dependent aspect of the homogenous transition is further demonstrated in Figure 4.11, which shows a checkerboard exposure with a square length of 170μm. At an exposure time of 250ms, it is clear that the film is not homogenous. The side length was measured to be 156μm. As the exposure time increases, the side length increases to 173μm at 400ms, and 203μm at 800ms. However, at a sufficiently high exposure time of 2400ms, a homogenous film of uniform thickness is developed.

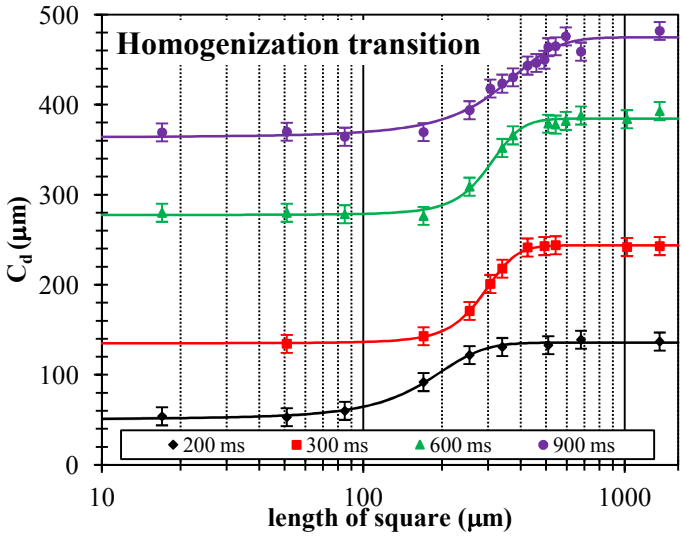

Figure 4.10: Homogenous transition of the PCMS resulting from a checkerboard exposure pattern. The transition was monitored for exposure times of 200ms (♦), 300ms (■), 600ms (▲), and 900ms (●).

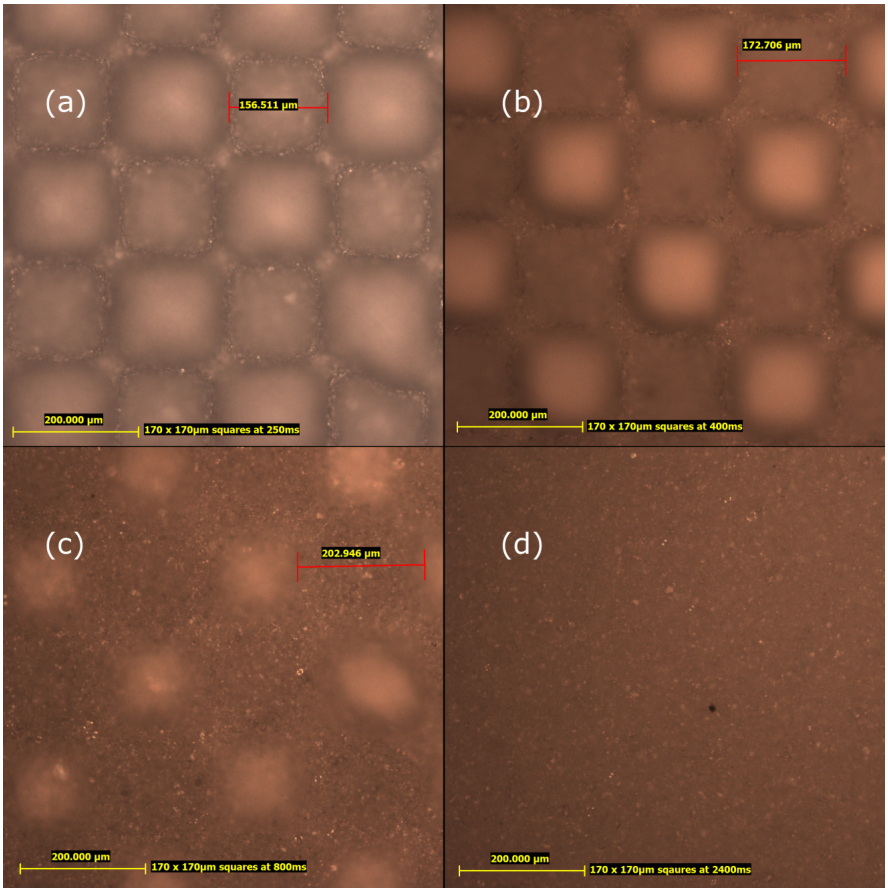

Figure 4.11: Demonstration of the time dependence of the homogenous transition. The images are of cured films with checkerboard exposure of 170µm square length at exposure times of (a) 250ms, (b) 400 ms, (c) 800ms, and (d) 2400ms.

These results show the dimensional and exposure time limits for the grayscale intensity assumption as well as the limits for an all white intensity assumption. For the cure depth to increase with a constant exposure time, the effective intensity must also increase. As a result, the intensity within the homogenous transition is not well defined and depends on the separation length as well as the size of exposed regions. Consequently, the Jacobs equation cannot directly be used because the light intensity cannot be determined. However, in order to obtain a predictive cure depth model, the Jacobs equation can be modified to ignore the light intensity and consider only the exposure time, which is shown in equations 4.4 - 4.7.

$$E = I * t \tag{4.4}$$

$$E_c = I * t_c \tag{4.5}$$

$$C_d = D_p \ln \frac{E}{E_c} = D_p \ln \frac{I * t}{I * t_c} \tag{4.6}$$

$$C_d = D_p \ln \frac{t}{t_c} \tag{4.7}$$

Here, D_p is equivalent to the resin sensitivity in the unmodified Jacobs equation, t is the exposure time, t_c is the critical exposure time, and I is the maximum effective light intensity. This equation is only applicable to the light source used. However, it can accurately predict the cure depth, which allows the implementation of exposure patterns within the homogenous transition in LAMP. The critical exposure time, t_c, can be determined by the same method use to determine E_c. Exposure time working curves of selected checkerboard square lengths are shown in Figure 4.12. From these results, it can be seen that as the square length of the checkerboard pattern increases, the slopes (resin sensitivity) first decrease, reach a minimum and then increase. A similar pattern is also

demonstrated in the x-intercepts (critical exposure time). Both minimums in the resin sensitivity and the critical exposure time occur at a similar checkerboard pattern.

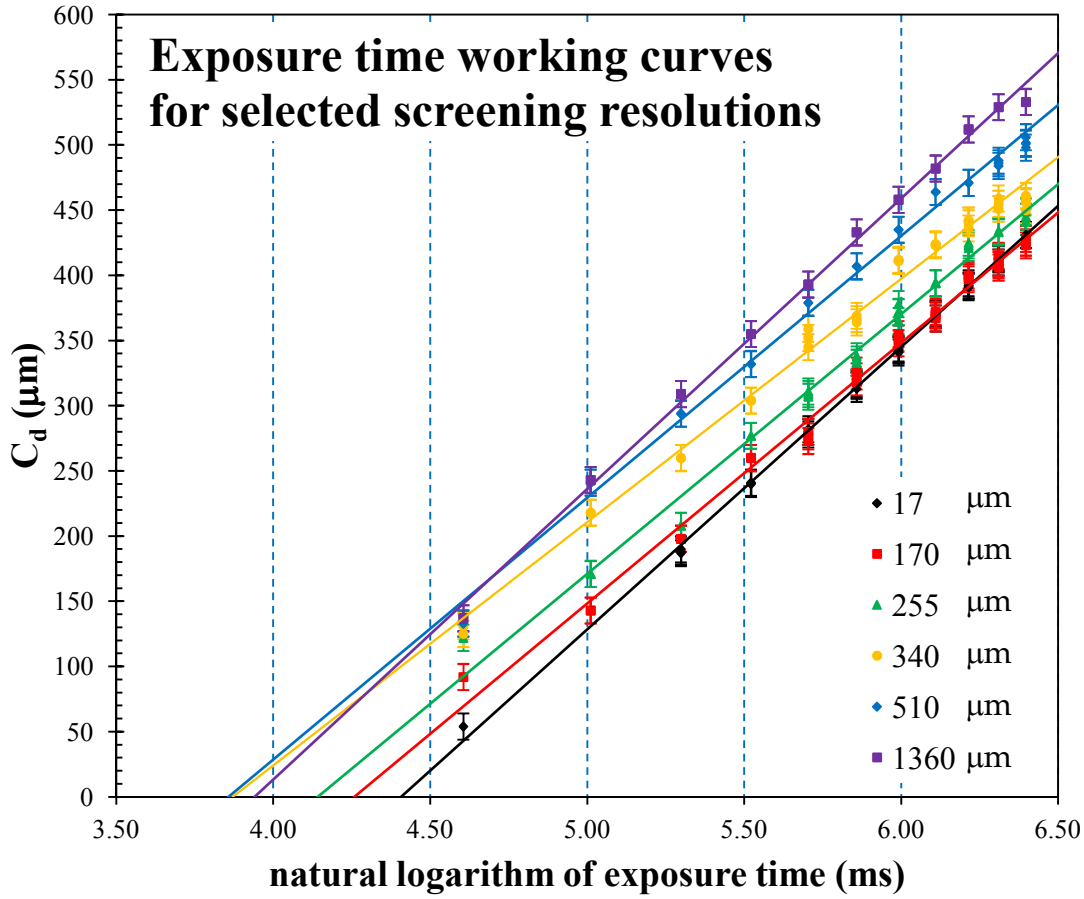

Figure 4.12: Exposure time working curves within the homogenous transition from checkerboard exposure with square lengths of 17µm (♦), 170µm (■), 255µm (▲), 340µm (●), 510µm (♦), 1360µm (■).

These phenomena are investigated further in Figure 4.13 where a summary of the curing parameters obtained within the homogenous transition are provided. When the square length is 85µm and lower, the curing parameters are constant, indicating that grayscale light intensity assumptions can be made. Also, when the square length is 1360µm and greater, the curing parameters reach all white intensity values and a full intensity assumption can be made to accurately predict the cure depth. It can be seen that

within the transition from grayscale exposure to all white exposure a minimum exists in both the critical exposure time and resin sensitivity at a square length of 425μm. It is interesting to note that at this screening resolution, curing will begin sooner than an all white exposure. However, due to the minimum in resin sensitivity, the cure depth growth rate is much slower than an all white exposure.

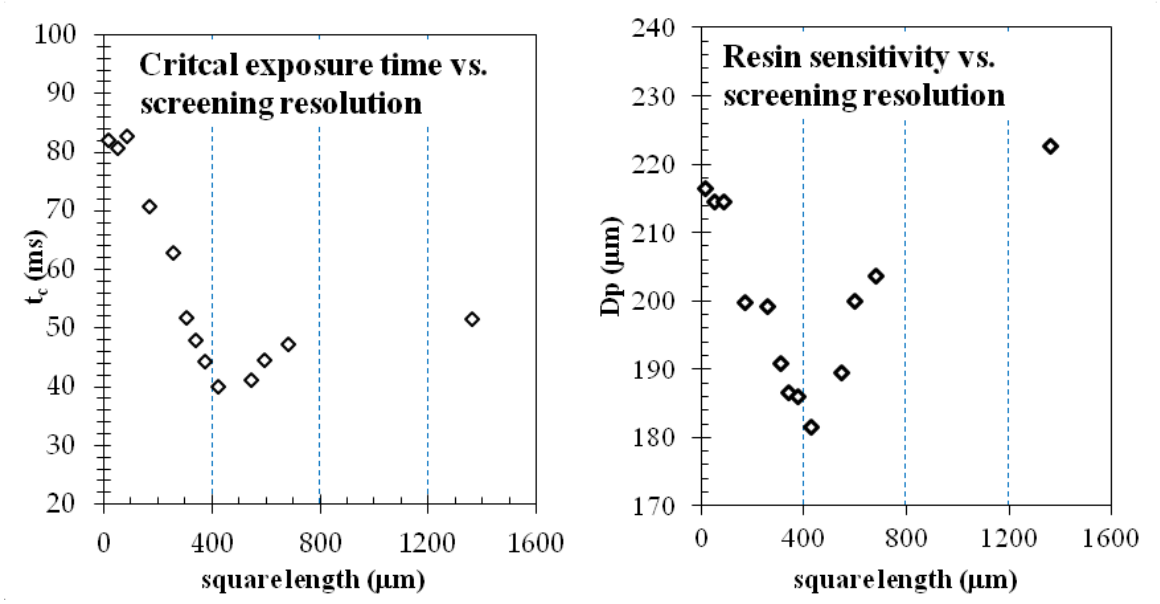

Figure 4.13: Summary of the trends in the critical exposure time and resin sensitivity at screening resolutions within the homogenous transition.

4.5 Conclusions

The objective of Chapter 4 was to investigate grayscale exposure, evaluate the assessment that grayscale exposure acts as an effective reduction in light intensity proportional to the grayscale value of the projected image, and define the screening resolution limits and time dependence of grayscale exposure. It was shown that grayscale exposure produces a lower cure depth than an all white exposure, which indicates that grayscale acts to reduce the light intensity for which the material system responds. The

magnitude of the reduction in light intensity was assessed and it was found that screening resolution determined the extent of light intensity reduction. If the screening resolution was sufficiently high, grayscale exposure developed and the intensity was effectively reduced to the grayscale value of the projected image. An additional exposure region was determined, which was termed homogenous transition exposure. This region was highly dependent on the dimensions of the exposed features. Interesting trends in curing parameters were revealed for this exposure region, where a minimum for both critical exposure time and resin sensitivity were observed for a checkerboard pattern with a square length of 425μm.

CHAPTER 5

THE INFLUENCE OF GRAYSCALE EXPOSURE AND SCREENING RESOLUTION ON CURE DEPTH

From the results in Chapter 4, it can be seen that two factors influence the cure depth resulting from projected grayscale images. These are the grayscale value of the image and the screening resolution used to convert the image to a distribution of black and white pixels. Based on these results, three distinct exposure types emerge: all white exposure, homogenous transition exposure, and grayscale exposure. Chapter 5 focuses on discussing and assessing models for predicting the critical energy and resin sensitivity for grayscale exposures and the light intensity experienced by the material system within homogenous transition exposure. Section 5.1 investigates models presented to describe the dependence of curing parameters on uniform light intensity variation and discusses their relation to the grayscale value of the projected image. Section 5.2 develops the scattering length pixelation model to predict the cure depth when operating within homogenous transition exposure. Section 5.3 summarizes the results of the predicted models.

5.1 Effects of Grayscale Exposure on Curing Parameters

The standard method for predicting the cure depth is dependent on the total energy dose and is independent of light intensity [13]. However, results from chapter 4 distinctly contradict this assessment for a reduction in uniform light intensity as well as grayscale light intensity. In the case of uniform light intensity reduction, it was determined that the manner in which the energy is delivered to the PCMS effects the

critical energy, wherein increasing light intensity increases the critical energy. This effect was also observed with grayscale exposures and as a result, concepts used to predict and explain the critical energy variation with uniform light intensity can also be used to predict the critical energy variation with grayscale light intensity. Recently, the light intensity dependence of the critical energy has been recognized by others and models have been developed in an effort to describe this phenomena [18, 46]. When the intensity of light incident on the PCMS is increased, the rate of initiation of primary radicals is directly affected, which is shown in equation 2.2. If the light intensity is increased, more primary radicals are generated for polymerization. A higher rate of initiation will increase the rate of polymer chain propagation [16].

$$R_p = k_p[M]\left(\frac{R_i}{2k_t}\right)^{\frac{1}{2}} \tag{5.1}$$

Where k_p and k_t are the rate constants of propagation and termination, which are considered material properties independent of the initiation rate. Therefore, the variation in cure depth with light intensity can be considered a result of competition between initiation, propagation and termination reaction rates [18]. This concept was the basis for a simplified radical depletion model developed by Halloran et al. [46]. Conceptually, if the radical initiation rate is high due to a high light intensity and compared to k_p, an excess of free radicals will arise in the PCMS and the potential for radical depletion reactions such as recombination, trapping and de-excitation will increase. As a result, a portion of the generated radicals will not contribute to polymerization. Therefore, at higher light intensities, more photons (higher energy dose) are required to develop an equivalent cure depth. These concepts can be expressed by equation 5.2 [46].

$$E_c(I) = E_{c,DE} + E_{c,excess}(I) \tag{5.2}$$

Where $E_{c,DE}$ is the "dose equivalent" critical energy, which corresponds to the range of light intensities where the critical energy is constant and independent of light intensity and $E_{c,excess}(I)$ is the increase in critical energy resulting from exposure to light intensities greater than the dose equivalent intensity range. The dose equivalent critical energy can be predicted by the inhibitor exhaustion model in equation 2.12. Since HDDA is a fast reacting monomer, it was found that at low light intensities, the PCMS shows dose equivalence. This is expressed by equation 5.3 and in equation 5.4 an expression for a minimum light intensity was proposed [46].

$$E_c = E_{c,DE}\left(1 + \frac{I}{I_{min}}\right) \tag{5.3}$$

$$I_{min} = k_p[M]fh\nu \tag{5.4}$$

Where I_{min} is the transition light intensity for describing dose equivalence, k_p is the propagation rate constant, $[M]$ is the monomer concentration, f is a proportionality factor, h is Planck's constant and ν is the frequency of the incident light. If the light intensity is lower than I_{min} the system behaves independent of light intensity and if the light intensity is greater than I_{min} the system depends on the light intensity. The change in critical energy with light intensity was proposed to be described by equation 5.5 [46].

$$\frac{\delta E_c}{\delta I} = (1 - \Phi)\left(\frac{\gamma_{INH}c_{INH} + \gamma_A c_A}{\Omega f k_p[M]\varepsilon_p}\right)\left(\frac{1}{c_p}\right) \tag{5.5}$$

Where γ_{INH} and γ_A is the effectiveness of the inhibitors and absorbers, c_{INH} and c_A are the concentrations of inhibitors and absorbers, and f is a proportionality factor. From this equation, it is predicted that the change in critical energy will be inversely proportional to photoinitiator concentration and directly proportional to inhibitor and

absorber concentration. However, for a selected formulation, the change in critical energy is expected to be linear. The linear trends found for the critical energy with grayscale and uniform light intensity suggest that this model can be used to predict the dependence of critical energy on light intensity. However, it should be noted that the predicted values deviate from the measured values. Values for the change in critical energy with light intensity presented by Halloran et al. were between 0.08mJ/mW and 0.1mJ/mW [46], which contrast with the values of 0.02mJ/mW obtained in this study shown in equation 4.2. This indicates that there may be additional effects contributing to the light intensity dependence of the critical energy. Some additional factors which could be considered are the variation in the range of investigated exposure dose and the use of different light sources. The cure depths measured in Chapter 4 were at higher energy doses than those used by Halloran et al. Therefore, differences could have developed due to the different stages of photopolymerization. At low exposure dose, the PCMS is in the initiation phase whereas at a higher dose, polymerization is in the propagation and termination stages. As a result, factors such as reduced mobility of propagating chains may influence the dependence on light intensity. The use of different light sources may alter the efficiency of initiation of primary radicals. A light source with a lower efficiency of initiating primary radicals may decrease radical depletion reactions and result in less variation with light intensity.

When investigating the influence of true light intensity variation on the resin sensitivity, it was found to behave independently of light intensity, which is consistent with Halloran's results [46]. However, it can be seen from Figure 4.7 that grayscale exposure produces a variation in resin sensitivity, where the resin sensitivity decreases

with a decrease in grayscale light intensity. This shows that while the critical energy can be treated as a function of true reduction in light intensity, the resin sensitivity cannot. Due to the complexity associated with light scattering in highly loaded ceramic suspensions [22, 47], numerical simulations would be required to fully investigate this phenomenon. However, a potential explanation for this effect could be found in the differences of the exposure technique. When a uniformly distributed light intensity is projected onto the PCMS, absorption can only develop vertically. This is contrasted with grayscale exposure, where incident light intensity is not uniform. As a result of scattering, absorption may be distributed both with depth and width. When the percentage of white pixels is high in the projected image, most of the absorption is with depth. However, as the grayscale value decreases, the percentage of regions with lateral absorption increases. This increase in lateral absorption could reduce the vertical absorption. Since the working curve measures only the cure depth, the determination of resin sensitivity is of vertical absorption. This could be the basis for scattering effects producing a dependence of resin sensitivity on the grayscale value of the projected image.

5.2 Predicting Cure Depth for Homogenous Transition Exposure

When the screening resolution of a grayscale image projected onto the PCMS is within the homogenous transition, neither the grayscale light intensity nor the all white light intensity can accurately predict the resulting cure depth. When considering exposure features within this length scale, it is important to consider how grayscale exposure could develop from fully exposed regions separated by unexposed regions. In Chapter 3, it was shown that the peak intensity from a one pixel projection is ~90% of the peak intensity resulting from an all white projection where every pixel of the DMD was switched on.

Similarly, the peak intensity resulting from the checkerboard exposure pattern was measured and it was verified to have peak light intensities within ~90% of the fully projected intensity as well.

As a result, the prediction of the cure depth from grayscale exposure deviates from the common method for predicting the cure depth in stereolithography, which uses the peak intensity of the laser beam to predict the depth of cure [13]. In contrast, grayscale exposure cures according to the grayscale value of the projected image, which corresponds to the average light intensity incident to the PCMS. When the screening resolution enters the homogenous transition, the PCMS begins to deviate from this averaging effect. This indicates that the PCMS has some critical dimension for which the light intensity is distributed or averaged. Conceptually, it could be interpreted that the material system has its own "pixel," where the power input to the "pixel" divided by its area is the resultant light intensity that causes curing in the PCMS. It can be hypothesized that for scattering systems, the dimensions of the material system's pixel are determined by the scattering length. Due to ceramic particle loading, light may be scattered instead of being absorbed by the photoinitiator. As a result, the light intensity is spread laterally to unexposed regions. To predict the scattering length and subsequent lateral resolution of the PCMS, the resin sensitivity equation can be considered, which is shown in equation 2.11 and can be rearranged to solve for scattering length [43].

$$l_{sc} = \left(\frac{1}{D_p} - (1 - \Phi)(c_P \varepsilon_P + c_A \varepsilon_A) \right)^{-1} \tag{5.6}$$

This equation enables the prediction of the light intensity for which the PCMS cures for any length scale. Figure 5.1 shows a schematic for how the light intensity within the PCMS can be predicted by the "scattering length pixelation model." In this model, the

PCMS resolution is defined as the scattering length, which translates into the radius of the PCMS "pixel." The light intensity input into this pixel is averaged over the pixel area to obtain an effective light intensity at the pixel's center. Then the pixel's center is translated an incremental distance from the previous location and the intensity is averaged over the scattering length pixel area for the new center. This process is repeated over the entire exposure area and acts to smooth out the light intensity by increasing the light intensity in unexposed regions and decreasing the light intensity in exposed regions.

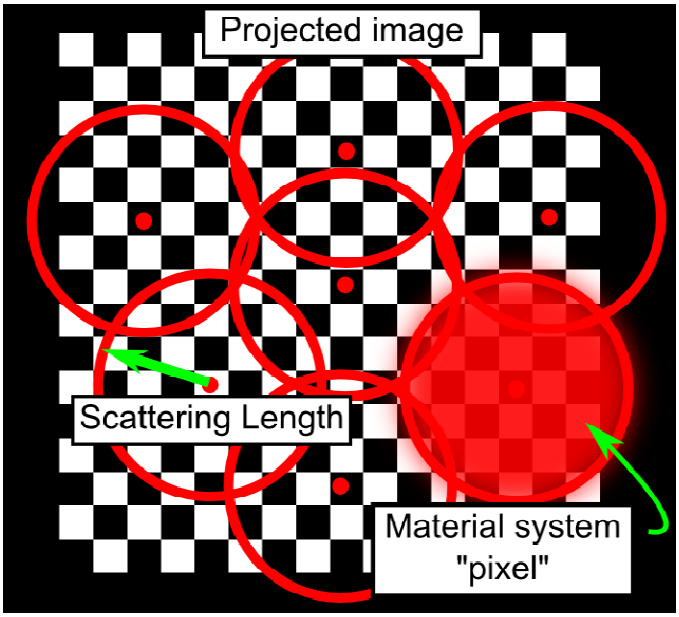

Figure 5.1: Schematic of material system resolution, where the projected pattern has features finer than the "pixel" of the material system, which can be defined by the scattering length

In order to properly predict the light intensity, the correct resin sensitivity must be selected to determine the proper scattering length. During homogenous transition exposure the resin sensitivity varies with the length of the square length in the checkerboard pattern. This variation may be described by the same mechanisms proposed to explain the decrease in resin sensitivity observed in grayscale exposure. As the

separation between exposed regions increases from grayscale exposure, more absorption is permitted to occur laterally due to scattering, which results in a decrease in D_p. However, as the pixel distribution approaches near all white exposure, lateral absorption is reduced, and the vertical absorption increases to the all white exposure resin sensitivity. Therefore, to predict the cure depth within homogenous transition exposure, the resin sensitivity values for each particular screening resolution must be used.

In addition to selecting the proper resin sensitivity input for equation 5.6, the molar extinction coefficients must be known. Estimates of these values can be obtained from the literature [43]. A summary of the parameters used to predict the light intensity distribution for various screening resolutions are shown in Table 5.1. The pixel averaging technique shown in Figure 5.1 was used to predict the light intensity distribution experienced by the PCMS resulting from homogenous transition exposure.

Table 5.1: Summary of the properties used in the calculation of scattering length based on equation 5.6.

Material properties used for predicting the scattering length

ε_p ε_A	80 2300	*(L/mol-cm)*	[43]
c_p c_A	0.102 0.002	*(mol/L)*	Chapter 2
Φ	.55	*vol%*	

Scattering length for investigated checkerboard screening resolutions

Square length (μm)	D_p (μm)	l_{sc} (μm)
17	216.6	247
170	199.9	226
340	186.6	209
510	200.8	227

Results from these simulations are shown for selected checkerboard screening resolutions of 17μm, 170μm, 340μm, and 510μm in Figure 5.2. Initially, when the square length of the checkerboard image is small, the result is a uniform reduction in light

intensity at the grayscale value of the projected image, which for the checkerboard exposure pattern is 50%. As the square length of the checkerboard pattern increases the light intensity increases in the exposed regions and decreases in the unexposed regions. Once the square length is sufficiently large the light intensity reaches the all white exposure intensity.

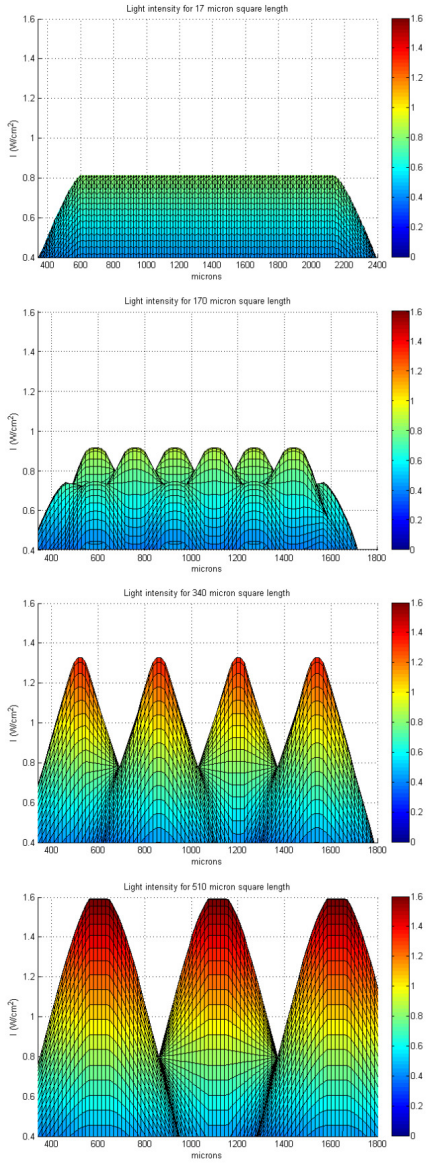

Figure 5.2: Simulated light intensity distribution experienced by the PCMS based on the scattering length pixel model for checkerboard exposure with square lengths of 17μm, 170μm, 340μm, and 510μm from top to bottom.

From Figure 5.2 it can be seen that when the square length approaches 510μm, the peak light intensity reaches the all white exposure intensity. This simulated result has a strong experimental validation, which was shown in Figure 4.10 where the cure depth plateaus with an increasing square length. This is a result of reaching the peak all white light intensity. While light scattering in a highly loaded ceramic suspension is complicated, this scattering length pixelation model indicates that it may provide an accurate estimate of the scattered light intensity distribution incident on the PCMS.

When considering experimental cure depth measurements, the cure depth will be determined by the maximum thickness of the cured sample, which will result from the maximum incident light intensity experienced by the PCMS. From the simulations in Figure 5.2, the maximum light intensity was determined and the cure depth is predicted by equation 5.7 as follows

$$C_{d,max} = D_{p,sr} \ln \frac{I_{max} * t}{E_c(I)} \tag{5.7}$$

Where $D_{p,sr}$ is the resin sensitivity for the selected screening resolution, $E_c(I)$ is the intensity dependent critical energy shown in equation 4.2, I_{max} is the maximum light intensity obtained from the simulations, and t is the exposure time. Results from these simulations are compared with the experimental working curves in Figure 5.3. It can be seen that the scattering length pixel model accurately predicts the maximum light intensity, The R^2 values obtained from these simulations ranged from 0.89 to 0.99. Due to these high R^2 values, this indicates that the scattering length pixelation model accurately simplifies the complex phenomena of light scattering in ceramic loaded suspensions. In addition, this model introduces new length scales which can be used in LAMP to fabricate features within the homogenous transition. However, the limitation of the model

is the need to determine the effective resin sensitivity for the target screening resolution. This limitation could be overcome by the development of a method to approximate the resin sensitivity or scattering length within the homogenous transition.

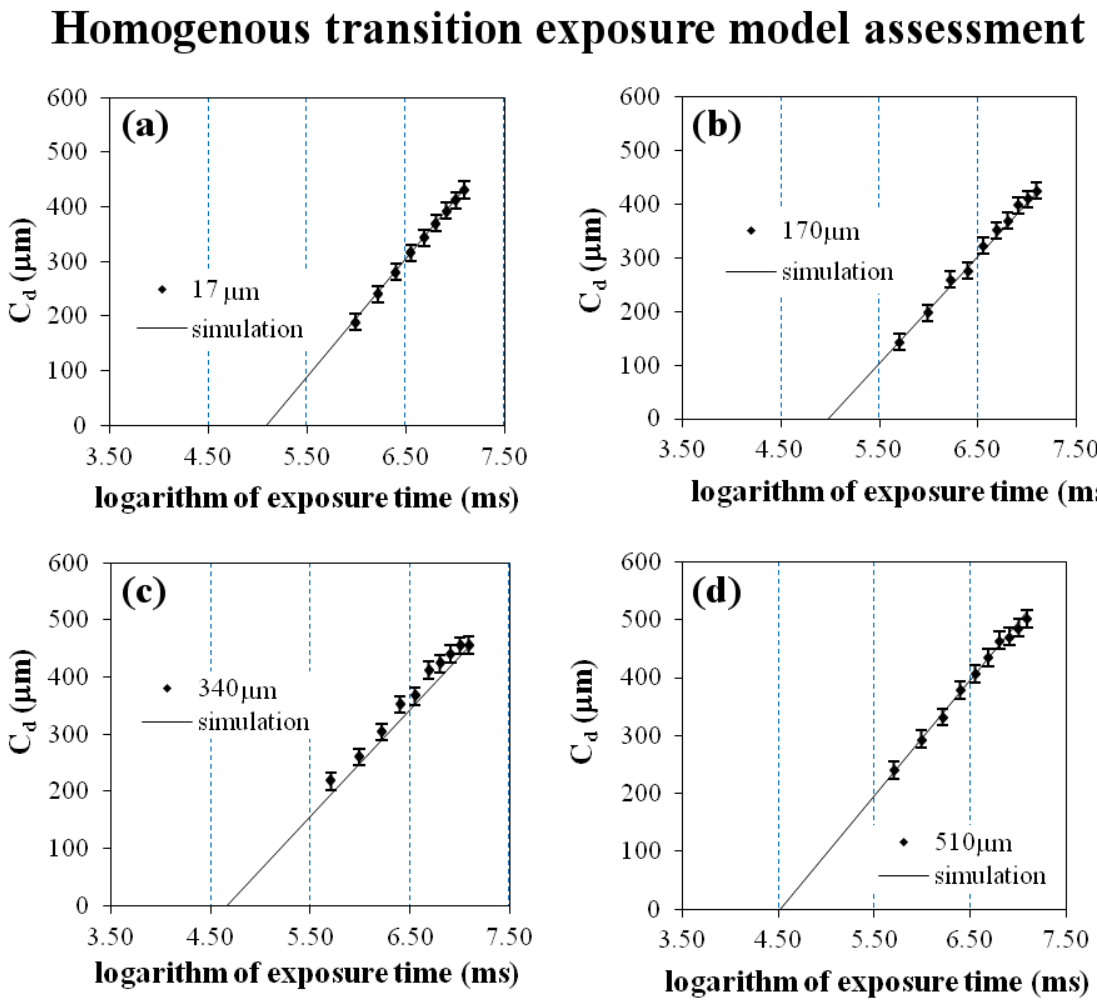

Figure 5.3: Comparison of experimental cure depth measurements with the scattering length pixel model for predicting the light intensity for grayscale and homogenous transition exposure. The screening resolutions tested were a checkerboard exposure with square lengths of (a) 17µm, (b) 170µm, (c) 340µm, (d) 510µm.

In addition to homogenous transition exposure transforming the light intensity experienced by the PCMS, it was also shown in Figure 4.10 and 4.11 that the homogenous transition is dependent on exposure time. This can be attributed to cure

width growth. While the light intensity distribution experienced by the PCMS can be assumed to be independent of exposure time, the cure width from regions of high light intensity will grow into regions of lower light intensity, which can be described by an adapted Jacobs' cure width equation [13], which is shown in equation 5.8.

$$C_w = B\sqrt{\ln\frac{I_{max}t}{E_c(I)}} \tag{5.8}$$

Where C_w is the cure width and B is the diameter of the PCMS pixel, which is $B = 2l_{sc}$. As the exposure time increases, eventually the cure width will overlap with the cure width from an adjacent projected region. Consequently, screening resolutions within the homogenous transition at low exposure times may be homogenous layers with uniform thickness at high exposure times. This is demonstrated in Figure 4.11 for a square length of 170μm.

5.3 Conclusions

Chapter 5 investigated the mechanisms of grayscale and homogenous transition exposure. In Section 5.1 the causes for the variation of the curing parameters with grayscale light intensity were investigated. It was concluded that the critical energy behaves equivalently to trends for variation in uniform light intensity, which may be adequately predicted by the radical depletion model presented by Halloran [46]. The critical energy was found to vary linearly with light intensity which is predicted in the radical depletion model. However, the magnitude of the variation was not accurately predicted, which could be related to differences in the energy dose range investigated as well as differences in the light source. The resin sensitivity was found to decrease with a

decrease in grayscale light intensity, which deviates from the behavior for uniform light intensity variation. This was proposed to be related to the differences in the exposure method, where the screening technique used in grayscale exposure enables lateral scattering and subsequent absorption, which may reduce vertical absorption measured by cure depth working curves. In section 5.2, the mechanisms behind homogenous transition exposure were investigated and the "scattering length pixelation model" was proposed to predict the light intensity experienced by the PCMS during homogenous transition exposure. The model treats the scattering length as the critical resolution of the material system, where the light intensity of the "pixel center" is obtained by the total incident power within the scattering length divided by the scattering length area. The effectiveness of the model was assessed at selected checkerboard exposure patterns and it was found to predict the cure depth to a high level of accuracy. The time dependence of the homogenous transition was discussed and it was proposed to be related to the cure width where the diameter of the exposure is twice the scattering length.

CHAPTER 6

APPLICATIONS OF GRAYSCALE EXPOSURE FOR LARGE AREA MASKLESS PHOTOPOLYMERIZATION

Chapter 6 presents the incorporating results of in LAMP to fabricate unsupported geometries and to reduce defects which arise during BBO due to internal stresses resulting from polymerization shrinkage stress. Section 6.1 reports the trends observed in the degree of conversion due to grayscale exposure, wherein the effect of grayscale exposure and screening resolution are presented and compared to an all white exposure. Section 6.2 presents a framework for utilizing grayscale exposure to fabricate unsupported features. The effectiveness of generating grayscale support structures (GSS) is presented and the results are discussed. Section 6.3 presents a framework for reducing defects in LAMP using grayscale exposure. The effectiveness of this framework is presented and the influence of grayscale on other types of defects is discussed.

6.1 Degree of Conversion Characterization for Grayscale and Homogenous Transition Exposure

The development of a cure depth model is crucial for the incorporation of grayscale exposure in LAMP. It enables the prediction of exposure dose or exposure time to generate the desired cure depth to ensure adhesion to the previous layer. However, the cure depth model provides no information on the degree of polymerization, which is crucial for making decisions as to which grayscales are appropriate to address the challenges facing LAMP. FTIR measurements can provide information about the degree of monomer conversion, which is directly related to the degree of polymerization. For the

fabrication of unsupported geometries, grayscale exposure must be applied to the surrounding regions in order to provide a GSS, where a particular degree of conversion will correspond to an appropriate support structure. Additionally, volumetric shrinkage and shrinkage stress information can be obtained from degree of conversion and rate of conversion measurements.

When considering the influence of grayscale exposure on the degree of conversion, two factors can play an important role in modulating the degree of conversion from an all white exposure, which are the grayscale value and the screening resolution of the projected image. First, the influence of homogenous grayscale exposure was investigated. The degree of conversion was calculated from the resulting FTIR spectra according to equation 2.13. The grayscale values investigated were 20%, 40%, 60% and 80%. Also, the degree of conversion for an all white, 100% exposure was investigated to serve as a reference. The degree of conversion was measured for each grayscale value at various exposure times so as to maintain a constant range of energy dose. Results of the degree of conversion measurements are shown in Figure 6.1. Reports by Ogliari et al. show that the degree of conversion measurements can be regressed by Hill's three parameter nonlinear regression with R^2 values of 0.99 [48]. Likewise, each grayscale exposure was regressed to Hill's equation and R^2 values greater than 0.98 were obtained. As a result, these curves can be used to gain an understanding of the trends and rates of polymerization.

Photopolymerization can be described in three phases, which are initiation, propagation and termination [14]. These stages are observed in Figure 6.1. Initially, at low exposure times the degree of conversion slowly increases, which is due to the limited

mobility of initiated radical species. After initiation, the monomer is rapidly converted to increase the molecular weight and form a cross-linked polymer network, which occurs during the propagation stage. The termination stage experiences autodeceleration, where chain propagation becomes diffusion controlled and the mobility of propagating radical chains is reduced. In the use on multifunctional acrylates such as HDDA, this causes the final conversion to not reach 100%, rather the degree of conversion plateaus at ~82%. This indicates that residual monomer is retained in the PCMS.

From Figure 6.1 it can be seen that grayscale exposure prolongs the initiation and propagation stages. This can be seen from a lower degree of conversion for a lower grayscale at a given exposure dose when the exposure time is lower than 2000ms. However, grayscale exposure does not change the final conversion of the polymer; rather, grayscale primarily affects the rates of polymerization. This is shown in the bottom panel of Figure 6.1, where the derivatives of the regressed models are plotted. It can be seen that as the grayscale value decreases, so does the maximum rate of monomer conversion. Additionally, the maximum rate of polymerization is delayed to higher exposure times, with the exception of 80%, which occurs at an exposure time similar to 100% white. This indicates that an 80% grayscale exposure does not significantly modulate the degree of conversion from an all white exposure. However, when the grayscale value is lower than 80% white, the reduction in polymerization rate is more severe. Additionally, it can be noted that the maximum rate of polymerization is shifted to higher exposure times for grayscale values of 60% or less.

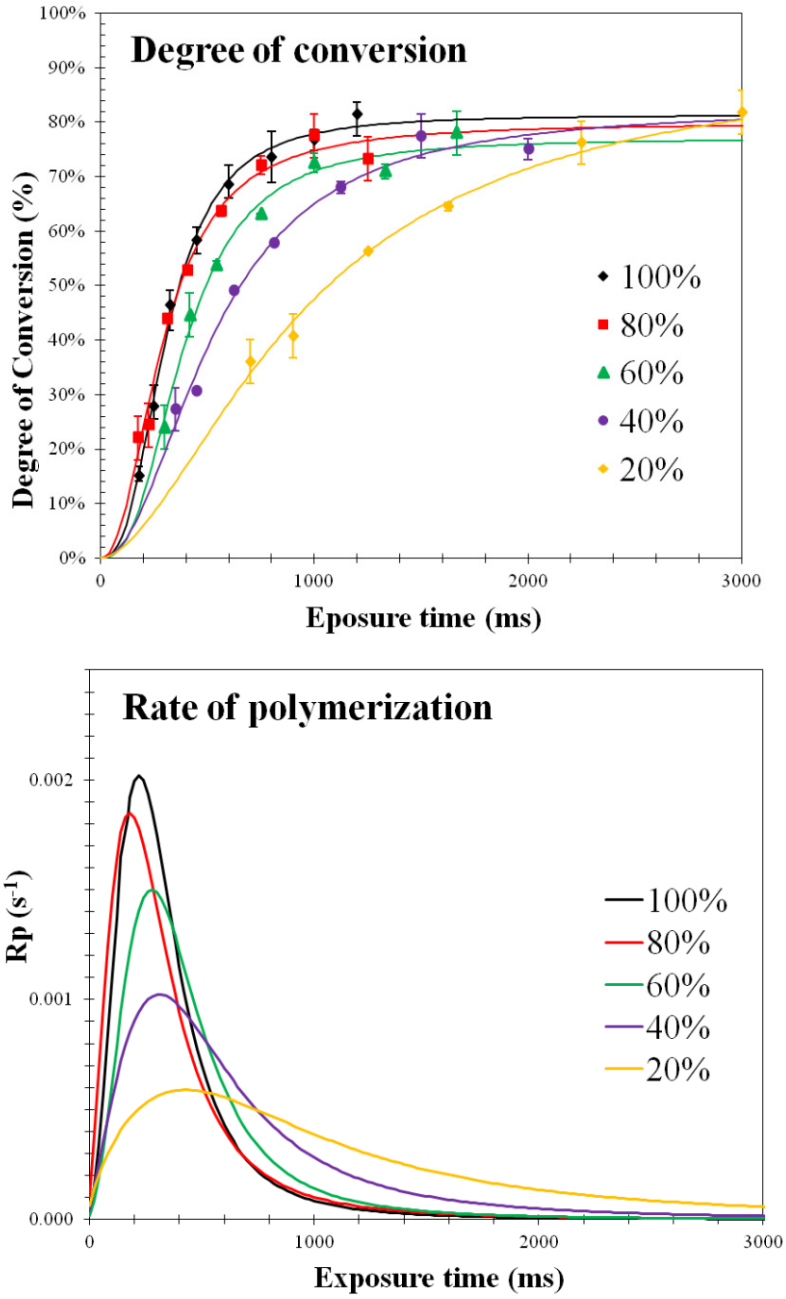

Figure 6.1: Degree of conversion and rate of polymerization for the PCMS at selected grayscale intensities of 100% (♦), 80% (■), 60% (▲), 40% (●), and 20% (♦) white.

In addition to considering grayscales within the homogenous region, it is also necessary to characterize the degree of conversion resulting from grayscale exposure within the homogenous transition, which is shown in Figure 6.2. To characterize the

effect of the homogenous transition on the degree of conversion, an exposure time of 600ms and a grayscale value of 50% white were examined. The checkerboard pattern was used as the screening technique and the square length of the primitives was varied from 17μm to 1360μm. It can be seen that there exists a minimum in the degree of conversion as the square lengths increase through the homogenous transition, which follows a similar trend to that seen in the resin sensitivity in Figure 4.13.

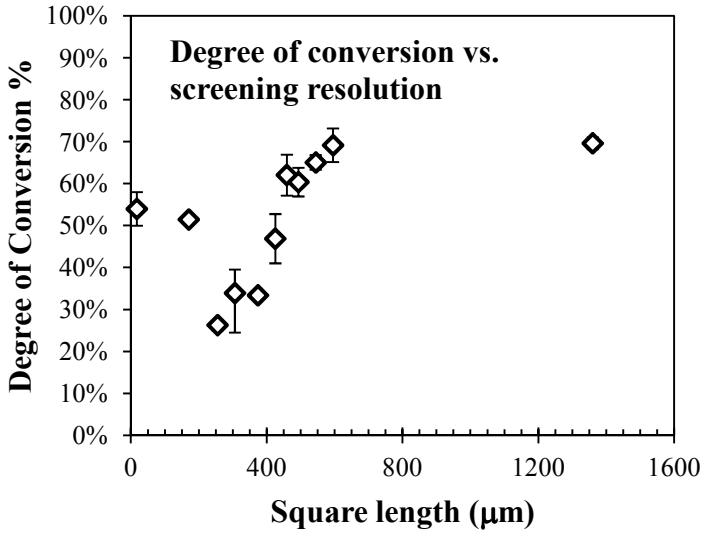

Figure 6.2: Characterization of the influence of screening resolution on the degree of conversion

Results from the dependence of the degree of conversion on the screening resolution can be separated into three regions, which are grayscale exposure, homogenous transition exposure, and all white exposure. Within the grayscale exposure region, the degree of conversion is found to be constant. A constant degree of conversion is obtained since any screening resolution with dimensions smaller than the scattering length acts to effectively reduce the light intensity to the grayscale of the projected image. When the square length is within the homogenous transition, the degree of conversion drastically decreases. This is anomalous behavior since the homogenous

transition is a result of grayscale light intensity increasing to all white light intensity. Due to this behavior of the homogenous transition, it was expected that the degree of conversion would also increase with the transition from grayscale exposure to all white exposure. However, while the light intensity is increasing in the exposed regions of the checkerboard pattern, the light intensity is decreasing in the unexposed regions. Consequently, residual and partially polymerized monomer becomes trapped between the exposed regions within the film. It is important to note that FTIR-ATR provides an averaged spectrum of the conditions of the investigated surface. Therefore, the average degree of conversion decreases upon entering the homogenous transition from the grayscale exposure region. However, the actual state of the investigated layer consists of regions with high and low degree of conversion, which corresponds to the exposed and unexposed regions, respectively. As the square lengths increase and exit the homogenous transition the degree of conversion increases and exceeds the degree of conversion obtained from grayscale exposure. This gradual increase in degree of conversion is related to the increased ability to remove residual monomer from the unexposed holes in the film. As the square length continues to increase, the degree of conversion eventually reaches a constant value. This region corresponds to the all white exposure region and the degree of conversion measured for this region is consistent with the degree of conversion measured for the 100% white exposure sample shown in Figure 6.1.

6.2 Fabrication of Unsupported Geometries with Grayscale Exposure

When considering grayscale exposure as a technique for constructing GSS in LAMP, three aspects must be considered: (a) the GSS must be strong enough to survive material recoating, (b) the GSS must be rigid enough to maintain the spatial location and

geometry of the unsupported feature, and (c) the GSS must be easily removed by development with an appropriate solvent after completion of the build. Each aspect can be related to the degree of conversion. As the degree of conversion increases, both the viscosity and hardness increase [27, 28]. For the grayscale layer to survive material recoating, the degree of conversion must be sufficiently high, i.e. the viscosity and hardness must reach a critical value or else the partially polymerized region will be removed or shifted from the intended location. Similarly, the degree of conversion must be high enough to ensure accuracy of the target feature. However, to contrast the requirements of a sufficiently high degree of conversion, the viscosity and hardness must be low enough to be easily removed after completion of the build in order to fabricate only the intended feature. The result of these two competing requirements is a target window within which the degree of conversion must be within for the successful fabrication of GSS. Additionally, it is possible that the degree of conversion required to survive material recoating is higher than the degree of conversion which satisfies an easy removal of the GSS after the fabrication is complete, which prevents the use of GSS.

Typically, a constant exposure time is used in LAMP for photopolymerizing individual layers throughout an entire build, which is determined by calculating the exposure time required to produce a cure depth of 135μm – 155μm. A cure depth larger than the layer thickness is used to ensure proper adhesion to the previous layer. These exposure times typically range from 120ms to 180ms based on the material formulation and age of the light source. As a result, this provides an exposure time range for which the cure depth and degree of conversion from grayscale exposure must be considered. Both the cure depth model and degree of conversion measurements can be used to

determine the appropriate range of grayscale values to investigate for GSS fabrication. If the critical energy dose for a selected grayscale value is greater than the grayscale energy dose, then no curing will occur, which indicates that this grayscale is not appropriate for GSS. However, if grayscale exposure produces a cure depth of 100μm or greater, then this indicates that GSS may be not be easily removed after the build is complete. Based on this rationale the appropriate grayscale range for GSS was determined to be between 46% and 82% by incorporating equations 4.2 and 4.3 into Jacobs' equation.

$$C_d = D_p(I) \ln \frac{E}{E_c(I)} \tag{6.1}$$

$$C_d = (11.3 * I_o * g + 194.8) \ln \frac{I_0 * g * t}{19.6 * I * g + 103.7} \tag{6.2}$$

In addition to considering the cure depth equation, the degree of conversion can also aid in the selection of an appropriate grayscale for GSS. From Figure 6.1 it can be seen that at an exposure time of ~170ms, the degree of conversion is ~14%. As a result, the grayscale used must produce a degree of conversion lower than that of the all white exposure. Grayscale values near 80% produces a degree of conversion similar to that for an all white exposure, which indicates that an 80% grayscale value will produce mechanical properties similar to an all white exposure during a build. Consequently, a grayscale value of 80% is not appropriate for GSS. From Figure 6.1 it can be seen that grayscale values of 60% and below produce a degree of conversion notably lower (~5%) than an all white exposure. Based on these findings accompanied with cure depth predictions, the range of grayscales appropriate for GSS fabrication in LAMP can be predicted to fall between 46% and 60%.

It can be noted that a degree of conversion of 14% is below the gel point, which is defined as the degree of conversion where the maximum rate of polymerization is

reached [26]. This indicates that when a layer is first exposed to UV light in LAMP, the viscosity and modulus are low compared to the completed airfoil mold. The maximum rate of polymerization for an all white exposure was shown to occur at ~27% ±2%, which is consistent with the literature [26]. Since the green body molds resulting from LAMP retain accurate geometries, this indicates that much of the photopolymerization occurs after the first exposure via "print-through." Kambly reports that print-through can propagate up to 4 to 6 layers beneath the exposed surface [9]. When considering the fabrication of GSS, techniques must be developed to reduce incremental curing from print-through in order to maintain the degree of conversion at or below the gel point.

In addition to selecting the grayscale values appropriate for GSS, it is also necessary to choose a proper screening resolution, i.e. to determine if the exposure technique should be a grayscale exposure or within the homogenous transition. The rationale behind fabricating GSS is to uniformly increase the viscosity of the region surrounding the unsupported feature. Therefore, it is appropriate to select a screening resolution within the grayscale exposure region, as the homogenous transition does not produce uniform layers. Therefore, the screening resolution used for all investigations of GSS was HDS super fine to guarantee grayscale exposure.

To evaluate the effectiveness of GSS in LAMP, a challenge component was designed. The side and front views of the challenge component are shown in Figure 6.3a, where the build direction is from the bottom up and the white regions correspond to areas to be solidified by UV exposure. The test component consists of a base, side wall, overhang and an unsupported square column. As the build progresses there will eventually be an unsupported feature for which the effectiveness of GSS can be assessed.

The unsupported feature was a square column which has a square side length of 1360μm and column height of 3mm. The column was separated from the base by a distance of 1mm, the side wall by 3.06mm and the unsupported structure connects to the part through an overhang.

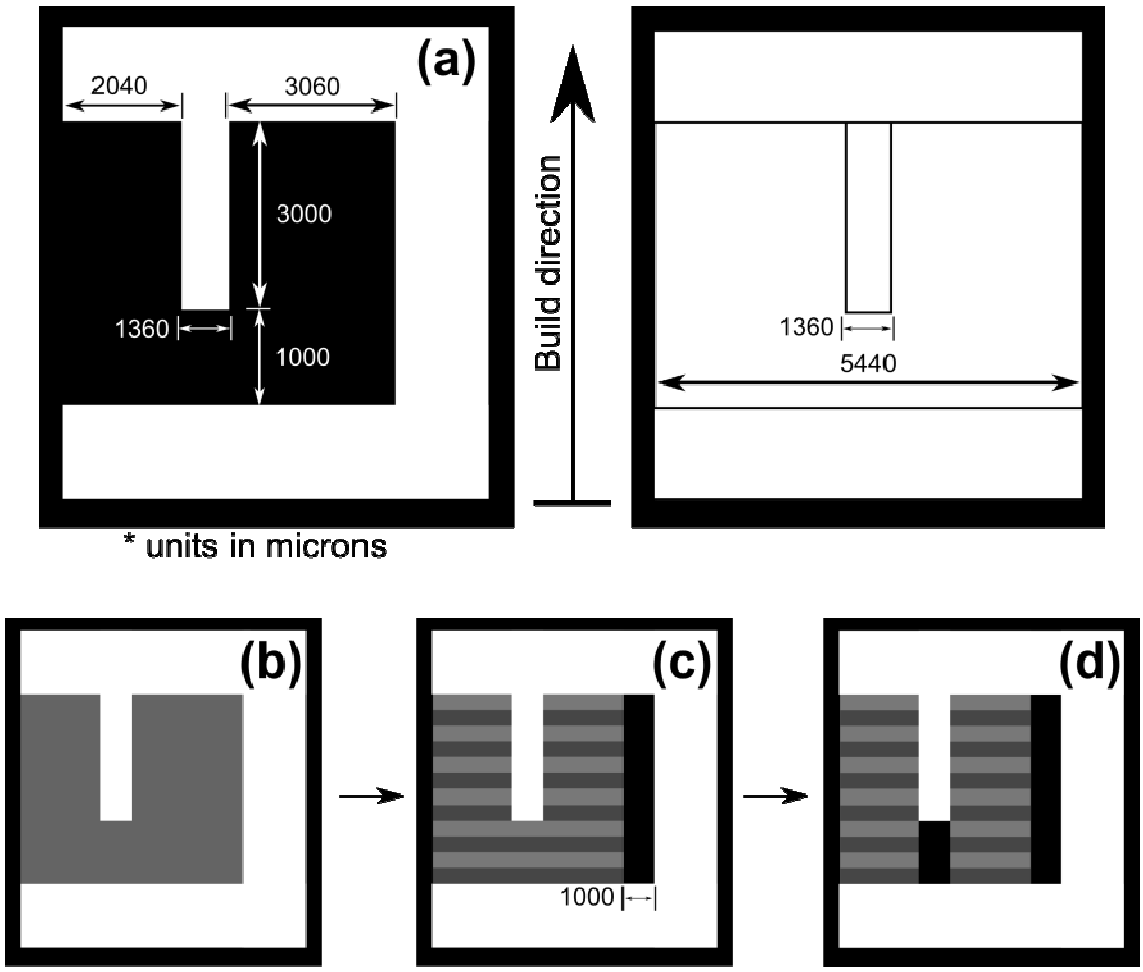

Figure 6.3: Iteration steps in the development of grayscale support structures (GSS). (a) shows the challenge structure designed for evaluating the effectiveness of GSS, (b) is the initial design of a GSS using a grayscale throughout the build, (c) incorporates the design of alternating grayscales between individual layers with the GSS, (d) is a print-through mediated alternating GSS.

Overhanging structures also present a challenge for LAMP. However, the focus of this thesis is on entirely unsupported features. Therefore, when the build reached the overhanging structure, additional exposures were conducted to ensure the overhang

would not obstruct the assessment of GSS for unsupported features. Figure 6.3b shows the first method employed for GSS. In this GSS, one grayscale level is selected for each layer and grayscale exposure surrounds the entire column. The grayscale exposure region connects to the base, side wall overhang and unsupported feature.

Results from the first trial are shown in Figure 6.4. Based on the prediction from the cure depth equation and degree of conversion measurements, the grayscale values investigated were 50%, 54%, 56%, 58% and 62% at a screening resolution of HDS super fine. The build parameters, such as material recoating speed and exposure time were set to 30mm/s and 170ms, respectively. From these results, an "all or nothing" behavior was observed. For this trial, grayscale values of 50% and 54% were unable to fabricate any component of the unsupported column. However, when the grayscale value was increased to 56%, nearly all the grayscale region polymerized to a degree of conversion which could not be easily removed. This trend continued to the 58% white grayscale value, where it can be seen that an even larger amount of GSS remained well adhered to both the side wall and the unsupported feature. For the grayscale value of 62%, the GSS is nearly a solid block. This result demonstrates good agreement with the predictions based on the degree of conversion measurements. A grayscale value of 60% was predicted to be the upper limit for GSS and it can be seen that a grayscale value of 62% may have mechanical properties too similar to the test component. This "all or nothing" behavior can be related to print-through and material recoating speed. A grayscale value of 54% for these build parameters was not viscous enough to adhere to the previous layer and survive recoating. As a result, the GSS became an unsupported feature in the following layer and was accordingly removed during recoating. This indicates that the

GSS must be successful for each layer. When grayscale values of 56% and greater were used, the GSS was strong enough to survive the material recoating process. Each additional layer induced incremental polymerization in the previous layers due to print-through. Since, the degree of conversion from a single layer is below the gel point, the PCMS is within the autoacceleration stage of polymerization. This causes the degree of conversion to rapidly increase with minimal energy dose. As a result, the degree of conversion within the GSS approaches a value similar to an all white exposure.

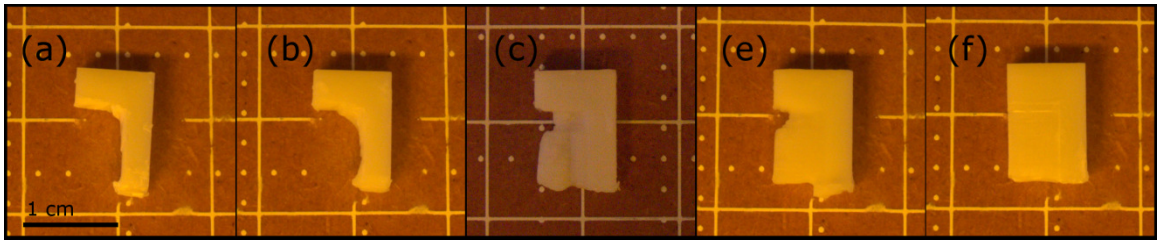

Figure 6.4: First trial of fabricating unsupported geometries using grayscale support structures with grayscale values of 52% (a), 54% (b), 56% (c), 58% (e), and 62% (f).

Reports by Xia and Fang demonstrate similar behavior in their investigation of GSS for projection microstereolithography [32]. In their test component, the GSS was bonded to the test component. However, the GSS was able to be removed through a piranha solution, which preferentially etched the partially polymerized support structure at a faster rate than the test component. In light of these findings, selective etching was investigated for the challenge component with a GSS of 56% to determine if this technique was suitable for LAMP. Two solvents appropriate for LAMP were tested, which were acetone and 3D101. Etching was conducted through sonication at room temperature for one hour.

Results from the etching investigation are shown in Figure 6.5. The test component in Figure 6.5a shows the condition and dimensions of the component prior to

etching. Individual components were used for each etching experiment. Figure 6.5b and 6.5c show the condition of the component after etching with acetone and 3D101, respectively. From these results, it can be seen that neither of the two etching techniques completely removed the GSS. In each case, the GSS remained bonded to the side wall and a significant portion of GSS surrounded the unsupported column. However, while portions of the GSS were etched, so was a proportional amount of the test component. It was found that as much as 1.25mm of the test component was etched from ultrasonic cleaning with acetone as well as 3D101. This shows that print-through can increase the degree of conversion in the GSS similar to that of the test component. As a result, the GSS could not be selectively etched. Rather, both the GSS and test component were etched at a similar rate.

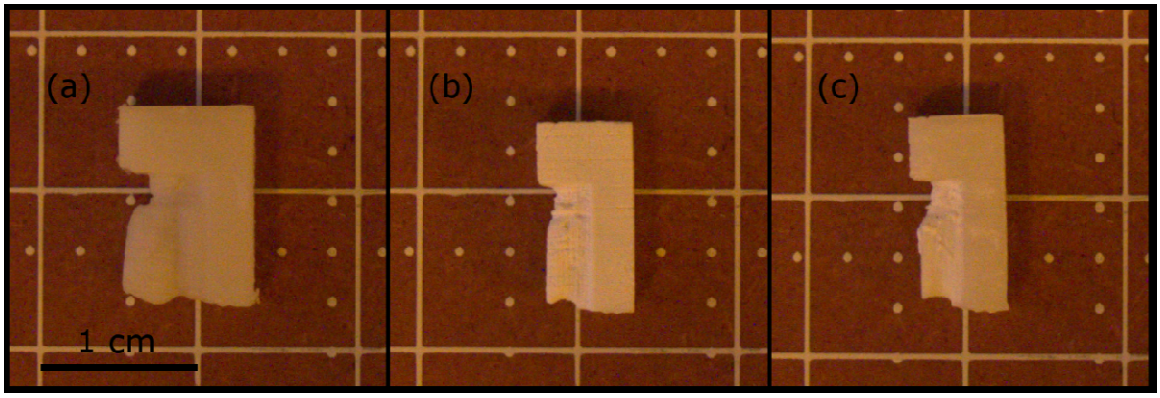

Figure 6.5: Images displaying the effectiveness of etching grayscale support structures. (a) shows the test component prior to etching, (b) shows the result of etching with acetone, and (c) shows the result of etching with 3D101 by ultrasonic cleaning for 1 hour.

Important observations can be made from these initial GSS investigations. First, it can be seen that the GSS formed at grayscale values of 56% possessed a degree of conversion too high to be easily removed and the GSS could not be differentiated from the test component. Consequently, a lower grayscale is needed to generate a GSS with a

lower degree of conversion. Second, a GSS could not be formed for grayscale values lower than 56%. From this result, it could be interpreted that the ideal grayscale for fabricating support structures is between 54% and 56% or it could be interpreted that the degree of conversion for easy removal after fabrication is below the minimum degree of conversion required to survive material recoating for the given build parameters. Third, during etching much of the GSS remained bonded to the sidewall.

In consideration of these observations, three improvements to the fabrication of GSS were made. First, the recoating speed was reduced from 30mm/s to 10mm/s and the exposure time was increased from 170ms to 218ms. A lower recoating speed acted to lower the minimum degree of conversion required to survive material recoating and increasing the exposure time enabled a larger difference in the degree of conversion between grayscale exposure and all white exposure. Second, a novel technique of alternating grayscale values between successive layers was developed to minimize print-through in the GSS. This technique is depicted in Figure 6.3c. The technique consists of alternating the grayscale values between successive layers from a high grayscale value to a low grayscale value. For instance, consider the GSS of 56% presented in Figure 6.4. The high degree of conversion generated from print-through could be reduced by reducing the grayscale of every other layer within the GSS. When the degree of conversion is below the gel point, due to autoacceleration, a lower degree of conversion has a lower corresponding polymerization rate, which is demonstrated in Figure 6.1. As a result, the lower degree of conversion acts as a barrier to mediate incremental polymerization throughout the fabrication of GSS. In addition to developing this method for print-through mediation, the connection of the GSS to the side wall was removed in

order to increase the surface area which can be developed after completion of the build. The gap separation between the GSS and the side wall was set to 1mm, and 2mm of GSS surrounded the column in all directions.

Results from these modifications are shown in Figure 6.6. For this experiment in alternating grayscale, the low grayscale value was held constant at 50% and the high grayscale value was investigated at 52% (b), 53% (c), 54% (d), and 56% (e). In addition, to the alternating GSS, a constant GSS of 50% is also shown in (a). The first row shows the test components before developing with 3D101. It can be seen that the GSS appears much less viscous than GSS formed in the first trial shown in Figure 6.3. The second row shows the test component after rinsing with a water jet using 3D101, which is a typical technique used to remove residual monomer. It can be seen that removal of the GSS reveals the successful fabrication of the grayscale supported test component.

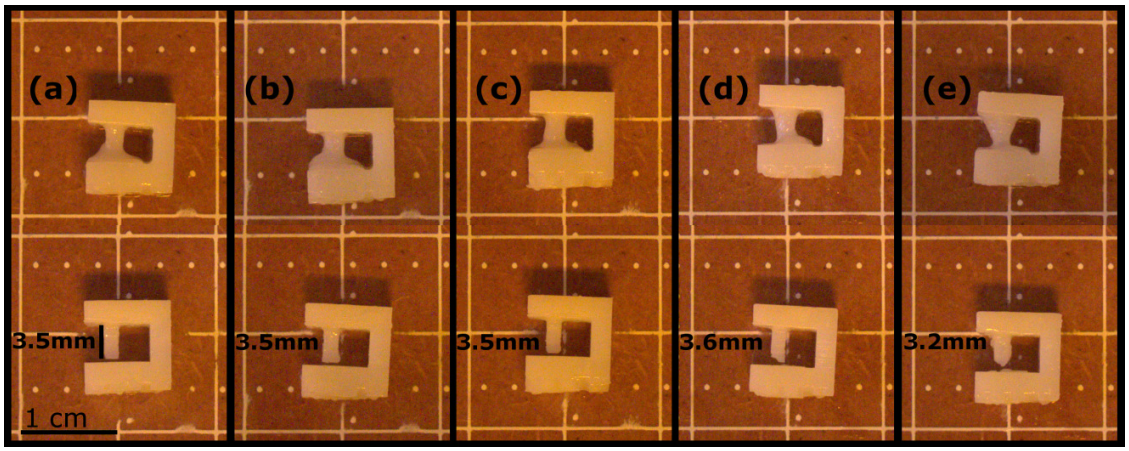

Figure 6.6: Fabrication of the test component using alternating GSS before (top row) and after (bottom row) rinsing with 3D101. The low grayscale was held constant at 50% and the high grayscale was varied from (a) 50%, (b) 52%, (c) 53%, (d) 54% and (e) 56%.

The success can be attributed to reducing the recoating rate, which reduces the minimum degree of conversion required to survive the recoating process. Figure 6.6a shows that a GSS of 50% can fabricate an unsupported column. This shows that

alternating GSS are not necessary to fabricate unsupported features. Rather, the critical parameter was the material recoating speed. However, it is demonstrated that alternating grayscale exposure within the GSS is an effective method for fabricating unsupported geometries as well. The advantage of alternating GSS is the mitigation of "all or nothing" behavior. Figure 6.6 showed that alternating grayscale GSS expands the range of grayscale that can be used to fabricate the unsupported column. This is evidenced by Figure 6.6e, where an alternating GSS of 50% and 56% was used. Previously, a GSS with the use of a single grayscale value at 56% was unable to be easily removed, due to significant print-through. However, inserting a grayscale value of 50% every other layer within the GSS enabled the successful fabrication of the unsupported feature and easy removal of the GSS with standard development techniques. This shows the ability of alternating grayscale to mitigate residual curing from print-through. This aspect increases the reliability of fabricating unsupported geometries and can allow for more variation in build parameters.

One aspect of the test component which must be noted is that the height of the column. The column height was designed to be 3mm, yet for each GSS, the height of the column was ~3.5mm. This can be related to print-through causing curing up to 5 layers beneath the column. When an all white exposure is projected on the layer above a grayscale exposure, the susceptibility of print-through is increased due to a higher light intensity. Grayscale exposure consumes many of the inhibitor species typically present in unexposed monomer. As a result, any additional exposure dose goes directly to polymerization, which causes the column to be longer than the design value.

In order to produce more accurate unsupported features an additional design revision to the GSS was performed, which can be seen in Figure 6.3d. In this design, grayscale exposure is removed from directly underneath the unsupported feature. This design feature attempts to mitigate print-through since the inhibitors in the PCMS must be consumed before curing can occur. As a result, the probability of developing additional thickness beneath the exposed layer is reduced, which could result in a more accurately built test component. Results from a print-through mediated alternating GSS is shown in Figure 6.7. The test component shown was fabricated with alternating grayscale values of 50% and 70%. The image in Figure 6.7a and 6.7b show the GSS before development and shows the unsupported column which appears after development, respectively.

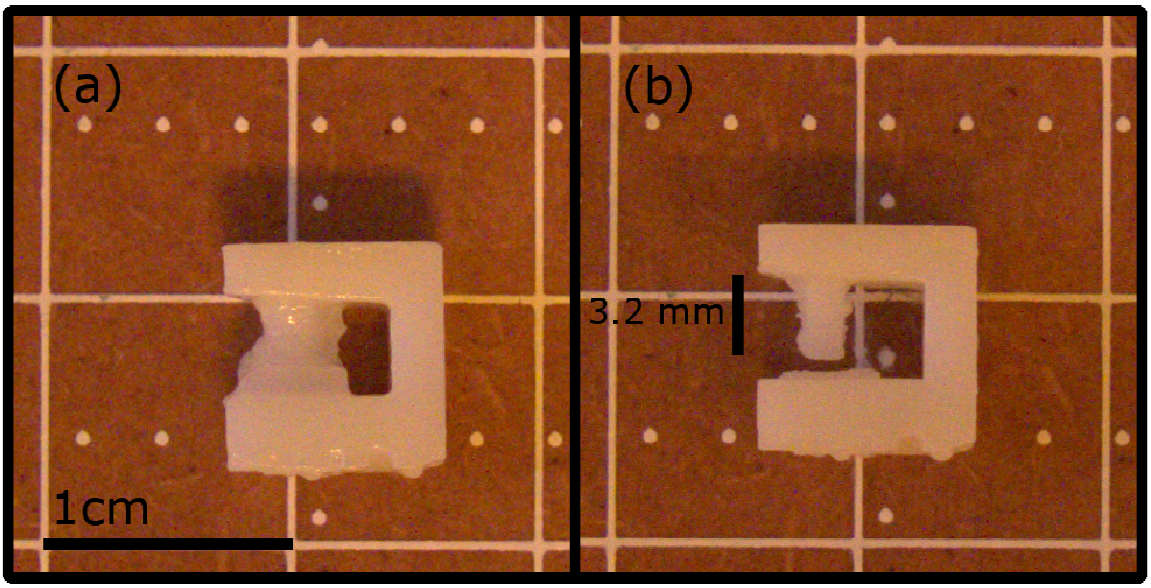

Figure 6.7: Results from print-through mediated alternating GSS. (a) shows the GSS prior to rinsing with 3D101 and (b) shows the fabrication of the unsupported geometry after rinsing with 3D101.

The alternating grayscale values for the print-through mediated GSS is more severe than the typical alternating GSS, which can be related to the volume reduction of

the grayscale support. From this result, a larger gap between the base and the unsupported feature can be seen, which results in a higher accuracy in the build direction. The column height was measured to be 3.2mm. This indicates that print-through develops additional thickness corresponding to two layers beneath the column in the absence of grayscale support directly beneath the column, as opposed to 5 layers when grayscale is beneath the column.

It was noted that more shifting occurred during the fabrication of the column, which resulted in a variable cross-section through the length of the grayscale supported column. In addition, it can be seen that some roughness in the base layer developed due to print-through from the higher alternating grayscale value. These effects could be mediated by increasing the dimensions of the surrounding grayscale. This could enable a smaller difference in the alternating grayscales, and the high grayscale used could be reduced, which would eliminate bonding to the base layer. A lager volume of GSS surrounding the column could also prevent shifting during material recoating.

6.2.1 Conclusions

The results of grayscale exposure for the fabrication of unsupported geometries in LAMP were presented and it was shown that grayscale support structures can be used to fabricate unsupported geometries while being easily removed after completion of part fabrication using standard development techniques. It was shown that techniques used in microstereolithography such as selective etching are not applicable for GSS in LAMP. However, with the incorporation of novel GSS designs such as alternating grayscale and print-through mediation, reliable and accurate unsupported features can be obtained. Additionally, the GSS can be easily removed after part completion without mechanical

methods, which is important for applications to LAMP. Many of the unsupported geometries encountered in airfoil molds are within the internal features of the mold. This technique of grayscale support structures holds promise for successfully fabricating unsupported features within airfoil molds and thus expanding the versatility of LAMP.

6.3 Influence of Homogenous Transition Exposure on Defects Generated During Binder Burnout

When an airfoil mold is successfully fabricated with LAMP, very few cracks are observed in the green bodies. As a result, the majority of defects generated during LAMP occur during binder burnout and sintering. BBO is a sensitive process of removing the structural component to form a fragile ceramic powder component ready for sintering. Some defects which can be generated during BBO are spalling, cracking, blisters, and voids [49]. To reduce these defects, the material composition must be carefully considered and heating rates must be sufficiently low [50]. Additionally, it is important to remove all the binder before sintering to higher temperatures. Mitigation of defects during binder burnout and sintering has been the focus of many studies and the results indicate that polymerization shrinkage may be the primary contributing factor [3, 5, 10, 50, 51].

Reports by Bae and Halloran investigated the formation of cracks during BBO and sintering in ceramic stereolithography, where dependence on hatch spacing and retracted hatch were investigated [5]. From their results, it was found that a larger retracted hatch produced more cracks. This was attributed to residual uncured monomer near the surface of the mold. The mechanism associated with this observation was thermal initiation of radical species inducing polymerization of the uncured monomer,

which caused shrinkage and sites for defect propagation. Interestingly, little dependence on hatch spacing could be associated to the observed horizontal and vertical cracks.

In LAMP, a uniform light intensity exposure is applied to a large area, which causes anomalous defects to form during BBO. One of these behaviors is “fissures,” which is shown in Figure 6.8. While large-scale defects that prevent functionality of the mold for casting are not present in green bodies, fissure precursors can be seen, which are shown in Figure 6.8A. Fissures formed during BBO are straight and parallel with the LAMP layers. Additionally, a periodicity of every 4, 6 and 8 layers is observed throughout the airfoil mold [3]. The origin of these fissures with temperature was reported and evidence of these features can be seen at temperatures as low as 148°C with cracks first appearing at 220°C. Interestingly, this corresponds to the temperature range where the ketone initiator undergoes thermal decomposition to form radicals, which may polymerize residual uncured monomer within the mold [51]. It can also be noted that significant weight loss does not occur until 300°C. This indicates that the resulting fissures are not due to pyrolysis. Figure 6.8B shows the state of the mold after heating to 193°C. From this image it appears that the fissures are formed during BBO, yet before significant weight loss has occurred, corresponding to the potential fissure precursors observed in the green body, which is confirmed in Figure 6.8C. For closer inspection, Figure 6.8D shows an expanded view of a typical fissure with a 6 layer period.

These observations provide a strong indication that the observed fissures are a result of polymerization shrinkage and the stress resulting thereof. During exposure of a single layer, the degree of conversion will vary with depth. Consequently, a large gradient in degree of conversion could exist at the interface of adjacent layers. When the

green body mold reaches temperatures sufficient to decompose the ketone initiators, regions of lower degree of conversion polymerize and shrink away from the adjacent layers. This effect is observed in Figure 6.8D by the lines between each layer.

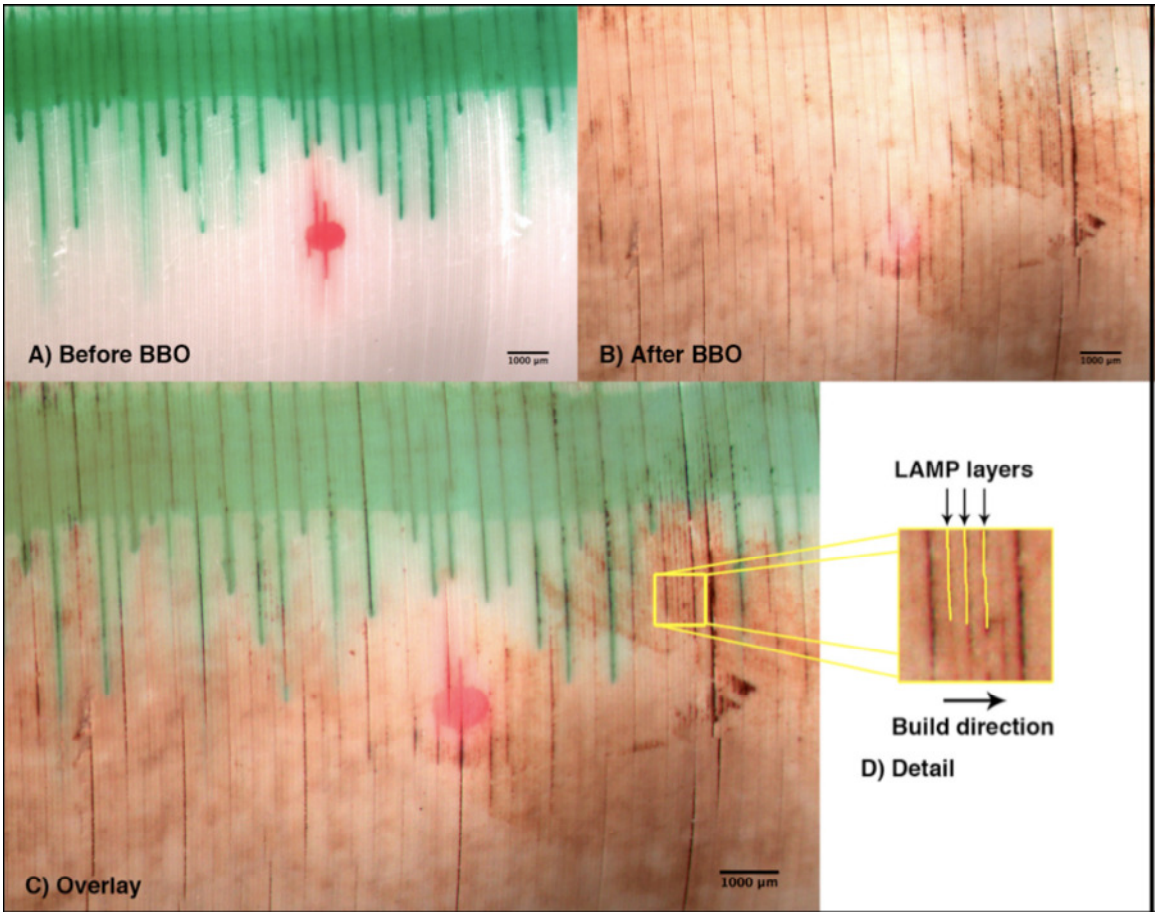

Figure 6.8: Stereomicroscope images of an airfoil mold before BBO (A) and after BBO (B). (C) shows an overlay of (A) and (B) to compare fissure development. (D) shows an expanded view of a typical fissure [3].

In addition to polymerization shrinkage, it is also important to consider polymerization shrinkage stress. From Figure 6.8A it can be seen that periodic fissure precursors exists in the green body mold and BBO only propagates the pre-existing defect. These fissures may be related to shrinkage stress. In LAMP, two aspects contribute to stress development from shrinkage, which are single layer shrinkage stress

and multiple layer shrinkage stress. Schematics of these two mechanisms are shown in Figure 6.9. When UV light is exposed to the PCMS, an incremental depth is polymerized and undergoes shrinkage. As the exposure progresses, an additional incremental element is polymerized. If there are no boundary conditions applied, the linear contraction from polymerization shrinkage in the second incremental element will induce a curvature away from the light source. This effect is demonstrated in Figure 6.9a and has been observed experimentally in Figure 6.10. However, in LAMP, a boundary condition is placed on the layer to remain flat. As a result stress is generated between adjacent layers.

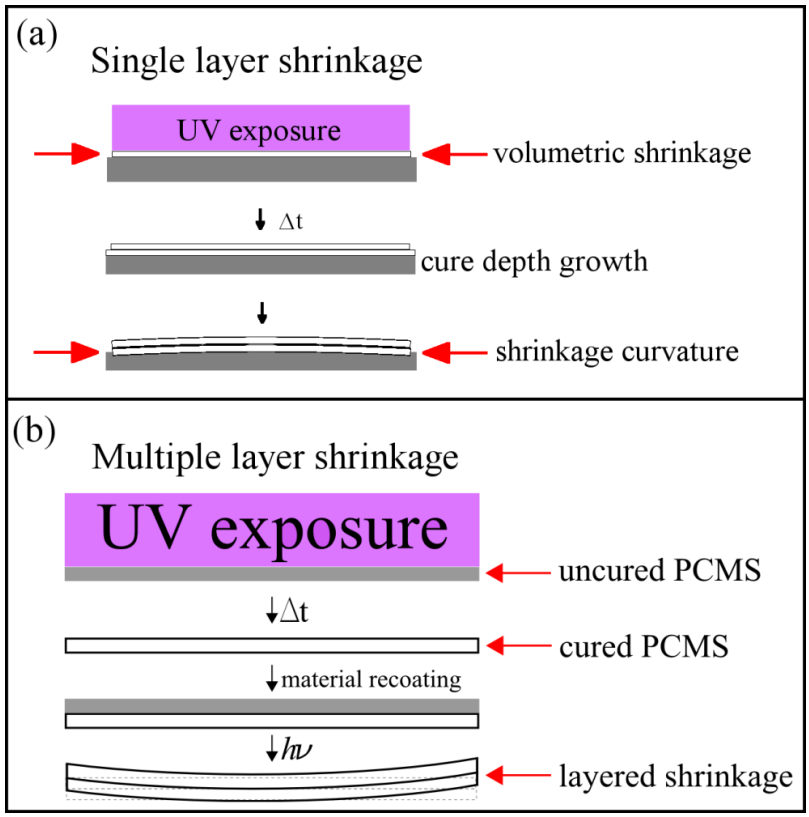

Figure 6.9: Schematic of the shrinkage mechanisms occurring in LAMP. (a) shows the shrinkage response to UV light for a single layer. (b) shows the shrinkage response for multiple layers.

The second mechanism of stress generation develops with the exposure of multiple layers, which is shown in Figure 6.9b. When an additional layer of PCMS is

exposed to UV light, the linear contraction interacts with the preceding layer. If no boundary conditions are applied curvature develops towards the light source. Multiple layer shrinkage stress will continue to develop deeper into the build due to print-through. It is interesting to note that print-through in LAMP can penetrate up to ~6 layers deep [9], which quite similar to the periodicity observed in the fissures. It can be hypothesized that the fissures are the result of a stress relaxation from the accumulation of shrinkage stress across multiple layers due to print-through.

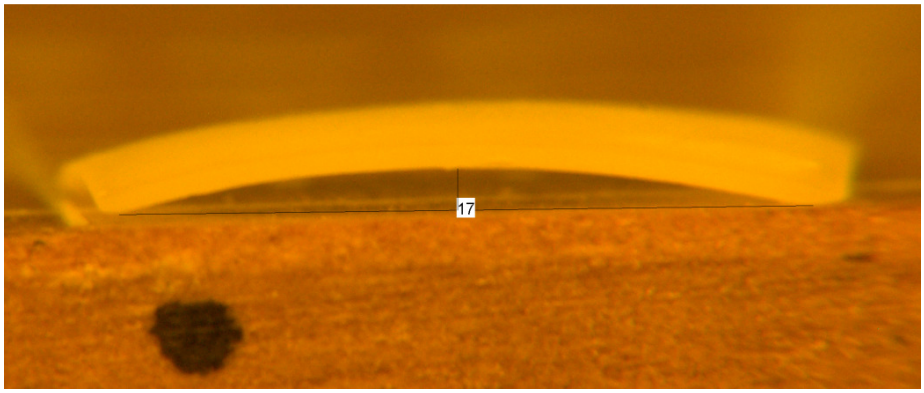

Figure 6.10: Demonstration of curvature induced by UV illumination within a single layer exposure.

In order to test this hypothesis, methods to reduce polymerization shrinkage and polymerization shrinkage stress through grayscale were investigated. Polymerization shrinkage has been directly related to the degree of conversion, where a high degree of conversion corresponds to a large volumetric shrinkage [52]. Therefore, it could be concluded that to reduce the negative effects of polymerization, the degree of conversion must be kept low. However, during BBO uncured and partially cured monomer can potentially polymerize due to thermal decomposition of the photoinitiator generating free radicals for polymerization, and due to the nature of BBO, volumetric changes should be minimized to reduce defects. In addition, a high degree of conversion is necessary to

ensure accuracy of the airfoil mold dimensions. Due to these considerations, reducing the degree of conversion is not a viable method for mitigating potential shrinkage related defects resulting from BBO and sintering. Consequently, mitigation of shrinkage defects must be addressed through a novel technique to obtain a high degree of conversion while mitigating volumetric shrinkage. This can be accomplished through exploitation of exposure patterns within the homogenous transition.

When the exposure pattern projected onto the surface of the PCMS is within the homogenous transition, the average degree of conversion can decrease by more than 50% as compared to an all white exposure, which is demonstrated in Figure 6.2. This indicates that the net mitigation of volumetric shrinkage may also be greater than 50%. When exposure patterns are within the homogenous transition, uncured or partially cured monomer is retained within the layer, which was shown to reduce volumetric shrinkage stress through monomer migration [42]. With the prospect of homogenous transition exposure mitigating the net effect of volumetric shrinkage and reducing shrinkage stress, this shows promise for reducing defects in the green body mold. Since the origin of fissures and delaminations was observed to depend on the state of the green body mold, reducing defects in the green body could ensure that BBO and sintering do not produce these types of defects.

To investigate the effectiveness of this technique for mitigating these types of defects, a test component was designed. The test component was a hollow cylinder, which is shown in Figure 6.11a. The outer diameter of the cylinder was set to 22mm with a thickness of 3mm and height of 24mm to simulate nominal dimensions used in airfoil molds. The hollow cylinders were fabricated with all white exposure and with three

screening resolutions within the homogenous transition. The screening techniques utilized were checkerboard patterns with square lengths of 170μm, 255μm and 425μm, which correspond to screening resolutions near grayscale exposure, in the middle of the homogenous transition, and near all white exposure, respectively. For each screening resolution, the layers were exposed in a staggered pattern so that the exposed region was unexposed in the following layer and vice versa, which is shown in Figure 6.11b.

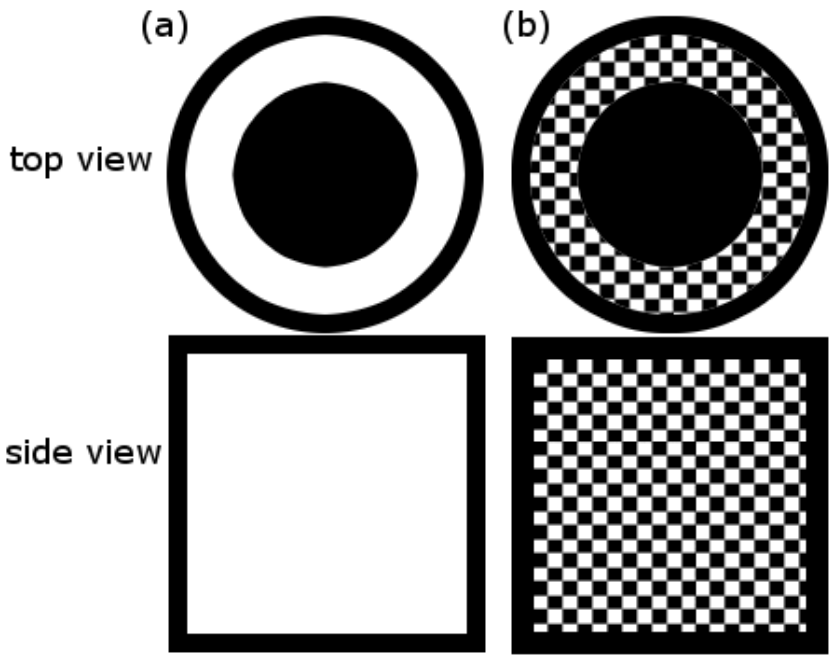

Figure 6.11: Schematic of hollow cylinder design used to investigate methods to reduce defects in LAMP components subjected to binder burnout and sintering. (a) shows an all white exposure technique and (b) shows a staggered checkerboard exposure technique

The exposure times selected to ensure proper bonding between layers were 278ms, 274ms and 274ms for square lengths of 170μm, 255μm, 425μm, respectively. Four samples for each screening resolution were examined to obtain a statistical information and four all white cylinders were fabricated with an exposure time of 170ms to serve as a reference. After fabrication, each mold was developed with 3D101.

Following development, the test cylinders were subjected to BBO and sintering, where the heating schedule is shown in Table 6.1. After sintering was complete, the mold was cooled to room temperature in one hour.

Table 6.1: Heating schedule for binder burnout and sintering

heating rate (°C/min)	peak temperature (°C)	holding time (hours)
5	260	0
3	300	0
0.5	350	2
0.5	475	0
3	600	0
12.5	1350	2

Figure 6.12 shows the result from fabrication of a test cylinder with all white exposure. The image in (a) shows the green body mold illuminated to enhance the detection of defects. The mold contained a smooth surface, but distinct defects were present in the green body. Figure 6.12b shows an expanded view of a section of the surface with enhanced contrast to demonstrate the fissure precursor. It can be seen that a similar periodicity to the mold shown in Figure 6.8A develops in the all white test cylinder. This indicates a high probability that fissures will develop during BBO. In addition to the fissure precursors, a defect related to “shuffle” can be seen, which is related to the serpentine path traversed in LAMP during large area exposure. From these defects in the green body, it can be expected that fissures will develop in the regions shown in Figure 6.12b and the shuffle defect will become more apparent during BBO and sintering due to thermally initiated polymerization and subsequent shrinkage..

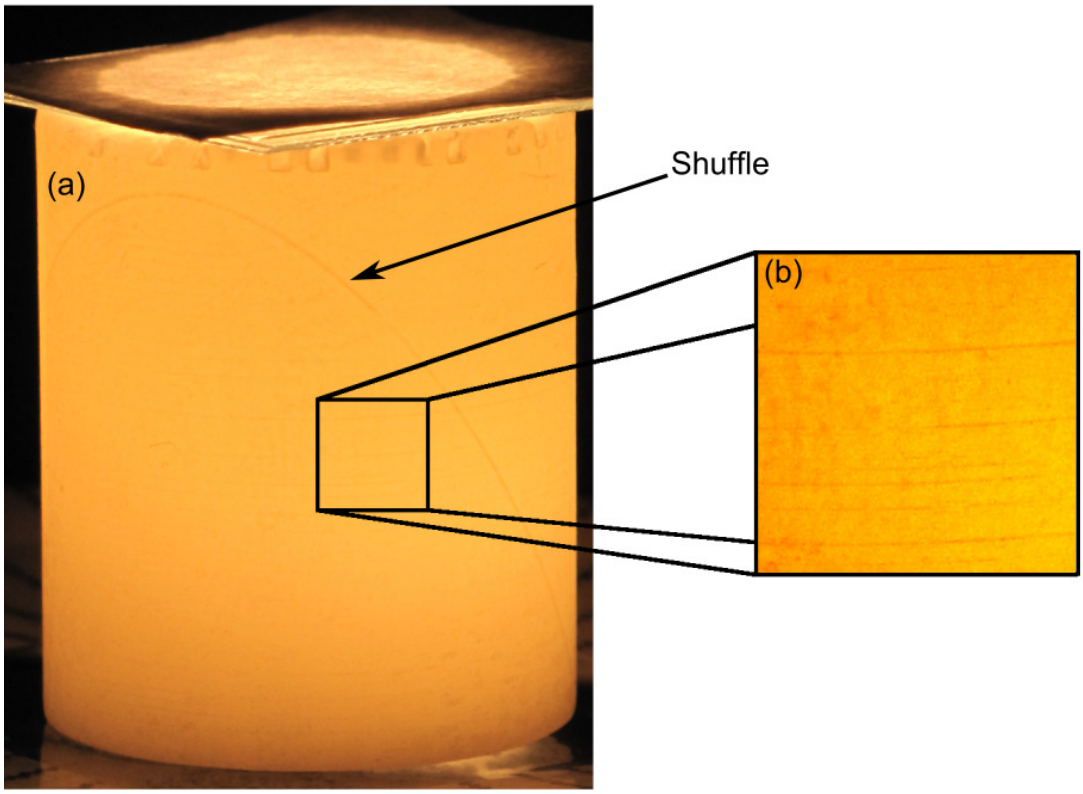

Figure 6.12: Test cylinder for characterizing mitigation of fissures and defects. (a) shows the green body mold fabricated with an all white exposure, (b) shows an expanded view with enhanced contrast to show fissure precursors.

This expectation is verified in Figure 6.13, which shows numerous horizontal defects resulting from BBO and sintering of the all white exposure test cylinder. The brightness from these fissures is higher compared to those in the green body, which indicate a larger defect. In this sample there were 4 horizontal defects which propagated throughout the circumference of the cylinder accompanied with many localized fissures. It can be seen that fissures occur throughout the height of the test cylinder, where the severity of the defect varies, yet the spacing remains constant. Figure 6.12B shows the regular spacing of 4, 6, or 8 layers.

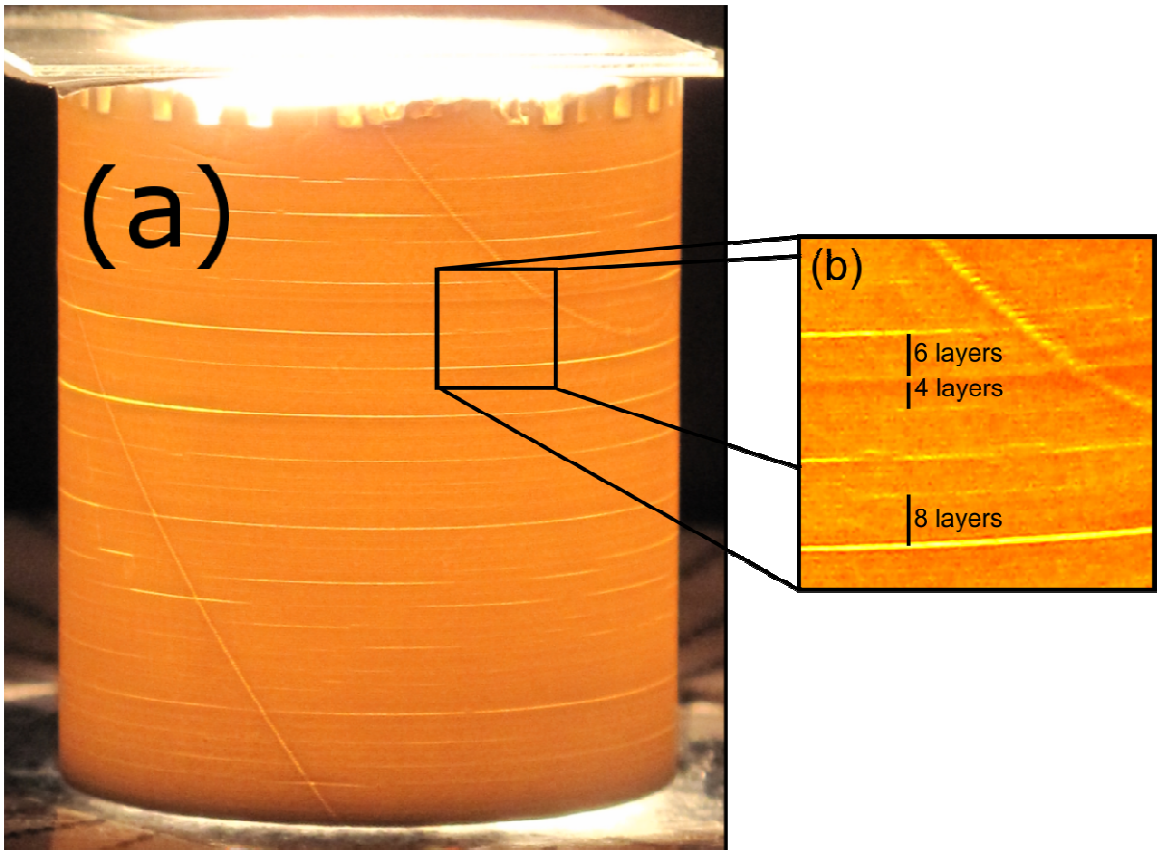

Figure 6.13: Test cylinder with all white exposure after BBO and sintering. (a) shows the side view with illumination to enhance the observation of defects, (b) shows an expanded view for a portion of the surface with enhanced contrast to demonstrate fissures.

The results from Figure 6.13 show that fissures occur in the test cylinder during BBO and sintering, which was predicted from the existence of fissure precursors in the green body. Therefore, this enables comparisons to be made regarding the effectiveness of homogenous transition exposure for reducing or enhancing these defects. Figure 6.14 shows the green body molds for cylinders fabricated with checkerboard exposure at square lengths of 170μm (a), 255μm (b), and 425μm (c). In each screening resolution the surface roughness increased compared to the all white cylinder. In addition, spalling is observed and portions of the outer surface were removed during development. These effects result due to limited connectivity of the cured portions within the cylinder and the

lack of a smooth outer surface. However, no fissure precursors could be discerned from the captured images. This indicates that fissures will not develop during BBO and sintering.

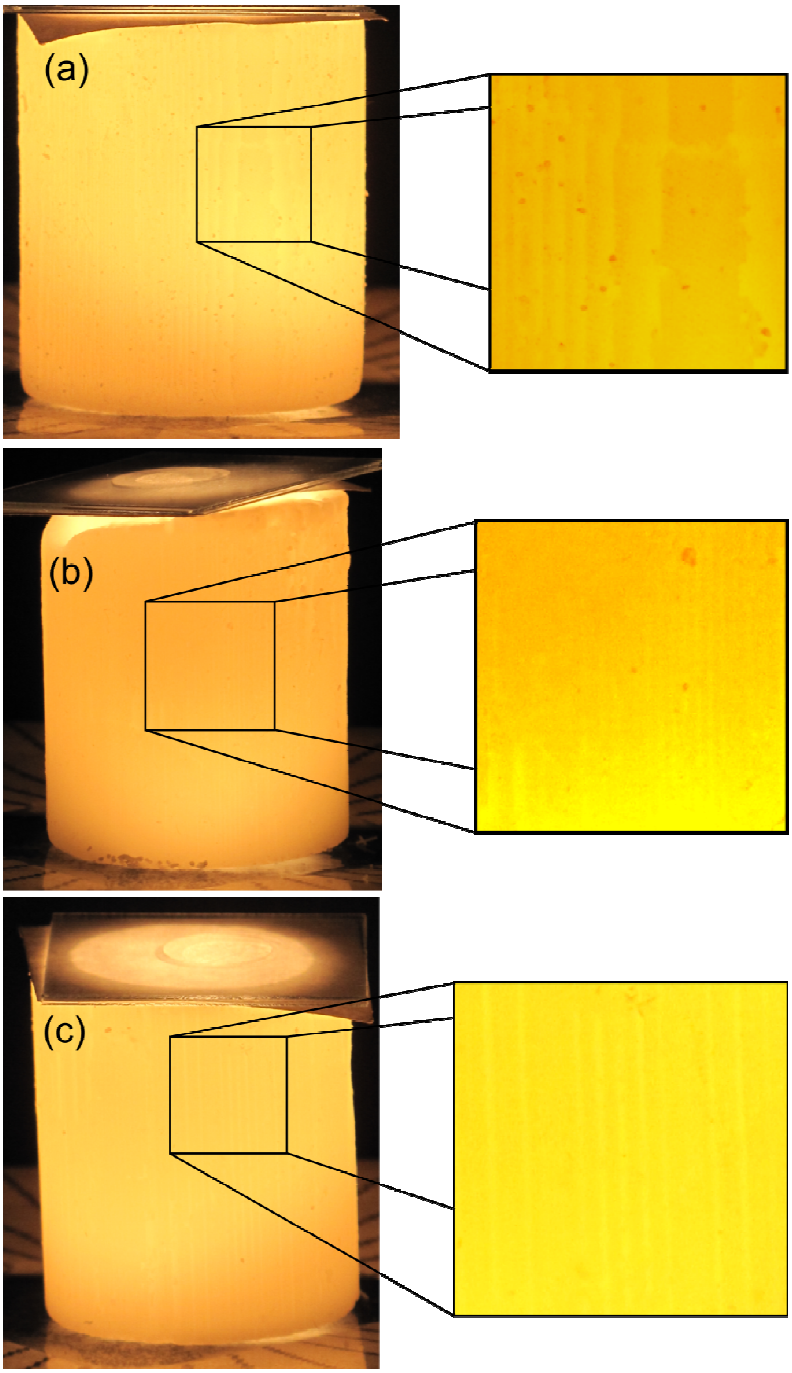

Figure 6.14: Green body test cylinders fabricated with alternating checkerboard exposure of square lengths (a) 170µm, (b) 255µm, and (c) 425µm.

In addition to the absence of fissure precursors in the green bodies, the absence of a shuffle pattern defect can also be noted. By observing the expanded views and enhancing the contrast, it can be seen that vertical lines appear on the cylinder surfaces, which could lead to the formation of vertical defects during BBO and sintering. The vertical features resulting from a square length of 170μm appear less straight compared to cylinder with a square length of 255μm and 425μm and irregularly spaced. For the square lengths in Figure 6.14b-c, the spacing is constant and the lines are straight and parallel to the build direction. Also, it can be seen that the spacing between vertical lines is larger and with higher contrast for a square length of 425μm compared to a square length of 255μm. The length of the spacing was found to be equivalent to the square length utilized in the exposure method, which indicates that the lines are a characteristic of the exposure technique.

These observations from the green body cylinders show promise for mitigating fissures and shuffle defects since their precursors were not observed. However, the exposure pattern introduced vertical lines and an uneven surface into the green bodies, which could cause the formation of other defects apart from fissures and shuffle. Figure 6.15 shows the effects of BBO and sintering on the test cylinders fabricated using a staggered checkerboard exposure with square length of 170μm (a), 255μm (b), and 425μm (c). Immediately, it can be seen that each screening resolution has notably fewer long range horizontal fissures. Figure 6.15a shows greatest number of long range horizontal fissures. However, these were the primary horizontal defects observed, which is contrasted with the all white exposure where numerous horizontal defects of smaller

length were observed. When examining the screening resolution with a square length of 255μm and 425 μm, no long range horizontal defects were observed.

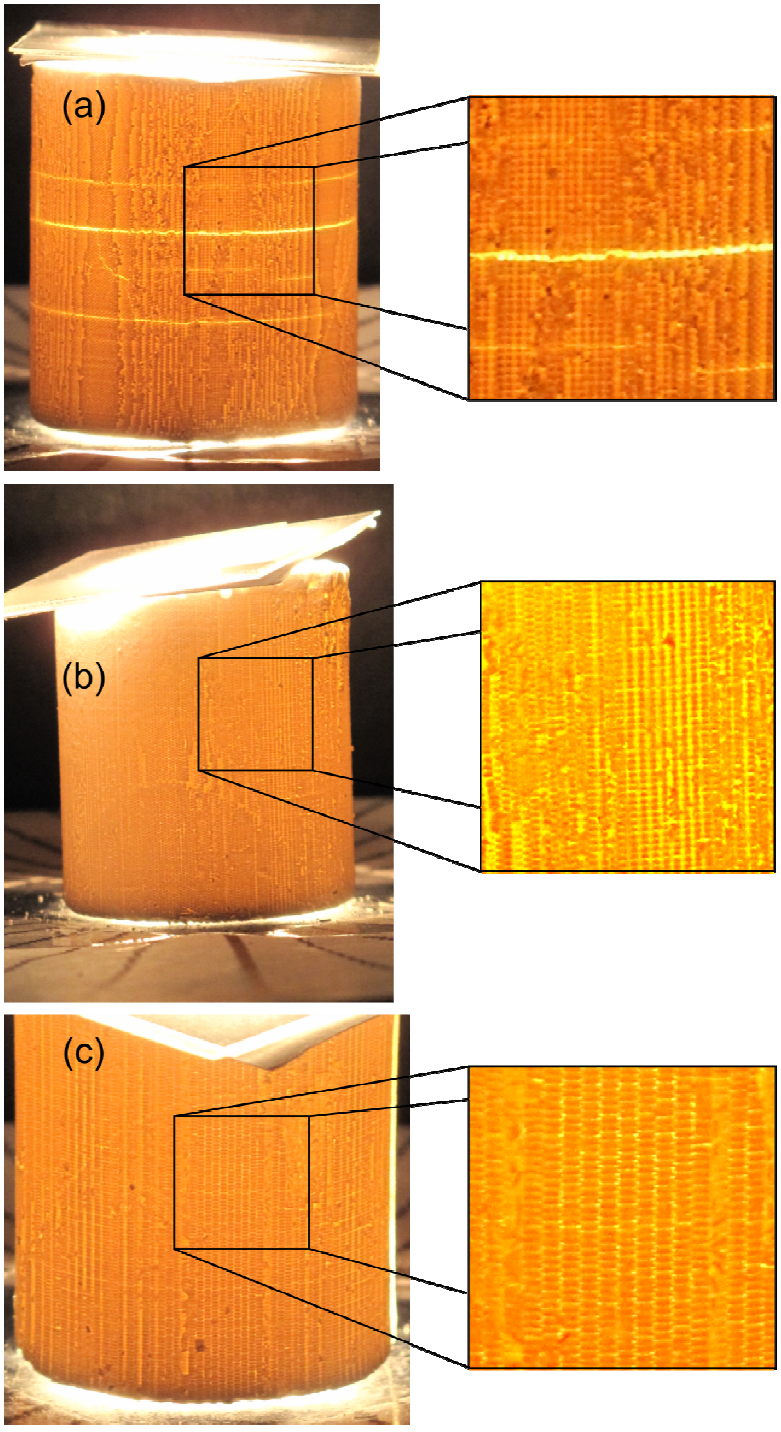

Figure 6.15: Test cylinders after BBO and sintering fabricated with alternating checkerboard exposure of square lengths (a) 170μm, (b) 255μm, and (c) 425μm.

Further inspection of the cylinder with a square length of 425μm shows that short range fissures may have developed. For both 170μm and 425μm square length screening resolution, the film is approaching homogeneity. In the case of 170μm square length, the layer is near a homogenous grayscale exposure and for a 425μm square length, the layer is near a homogenous all white exposure. From this consideration, a 455μm may have mitigated features most efficiently due to its location in the center of the homogenous transition. These results indicate that a proper selection of homogenous transition exposure may be a viable technique for reducing fissures and delaminations. For the examined screening resolution, a square length of 255μm performed most efficiently at reducing all types of defects including fissures.

When considering the other defects, it can be seen that while the shuffle defect was not observed in the green body cylinders, the defect develops in each investigated screening resolution. However, the intensity of the light projecting for the shuffle defect is less than the intensity seen in the all white cylinders and the feature is more poorly defined. As a result, homogenous transition exposure did not eliminate the shuffle defect, but it may have reduced it effects, which could be attributed to local shrinkage. Another effect which was not detected in the green test cylinder is shown in the expanded views of Figure 6.15. In the green cylinders with alternating checkerboard exposure, “continuous” vertical lines were observed. However, a transformation to “dotted” lines occurred as a result of BBO and sintering. This effect can be attributed to polymerization shrinkage resulting from thermal initiation of radicals and polymerization prior to pyrolysis. As a result, homogenous transition exposure may have converted the large

scale fissures seen in all white exposure to isolated “micro-fissures,” which prevented the accumulation of shrinkage to produce larger defects.

Due to the vertical ordering of these micro-fissures, stress relaxation may occur vertically. Investigations into vertical cracks are shown in Figure 6.16 which shows test cylinders where significant vertical cracks developed for each exposure technique. The largest vertical cracks occurred for screening resolutions with a square length of 455µm (Figure 6.16d) where vertical cracks acted to split the test cylinder in 2 of the 4 investigated samples at that screening resolution. Checkerboard patterns with square lengths 170µm (Figure 6.16b) also resulted in long range cracks. For this sample it appears that a horizontal defect prevented further propagation of the vertical crack. For the all white exposure cylinder many horizontal fissures occupied the sample, which is shown in Figure 6.16a. As a result, large scale vertical cracks were mitigated and the sample contained many small vertical cracks. Figure 6.16c showed the least large and small scale vertical cracks, which corresponds to a checkerboard exposure with a square length of 255µm

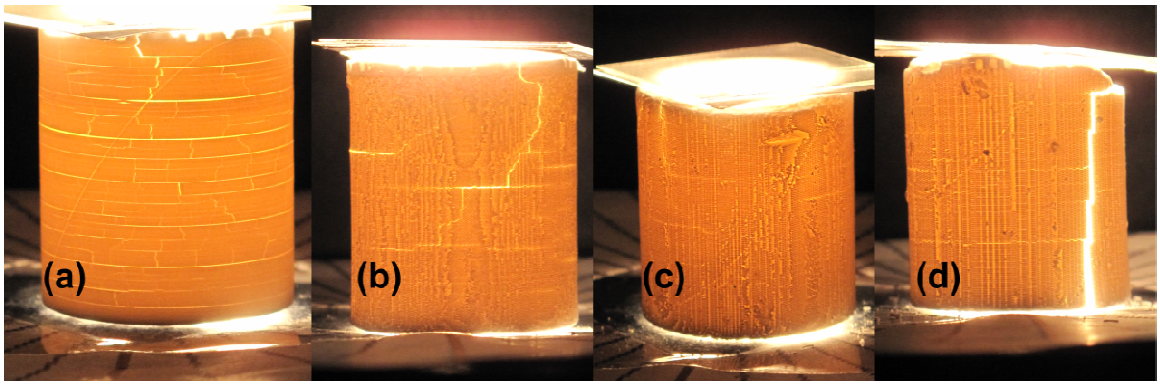

Figure 6.16: Test cylinders exhibiting vertical cracks, where (a) shows a test cylinder using all white exposure for reference. A checkerboard exposure pattern with a square lengths of (b) 170µm, (c) 255µm, and (d) 455µm was utilized.

6.3.1 Conclusions

From these results, it can be seen that a screening resolution in the center of homogenous transition exposure produced the most promising results for mitigating both horizontal and vertical defects. Screening resolutions in the center of the homogenous transition were shown in Chapter 4 to produce a minimum in the resin sensitivity, and in Chapter 6 showed a minimum in the degree of conversion. Low resin sensitivity reduces print-through by increasing the attenuation of the light source, which helps to reduce the accumulation of print-through related stresses. Additionally, a low average degree of conversion reduces volumetric shrinkage during LAMP, which helps reduce the shrinkage stress and reduce the development of fissure precursors.

CHAPTER 7

SUMMARY AND CONCLUSIONS

This thesis conducted fundamental investigations essential to advancing the capabilities of LAMP and demonstrated successful incorporation into LAMP to solve persistent challenges associated with fabricating unsupported geometries and mitigating defects arising during BBO and sintering of the green body molds. The technique explored to address these challenges simultaneously was grayscale exposure. Chapter 1 provided an overview of LAMP, which uses a scanning spatial light modulator to selectively cure a large area of PCMS with fine feature resolution by maskless projection of UV light. Chapter 1 also discusses the ability of LAMP to produce integrally-cored airfoil molds for investment casting. Challenges facing LAMP for this application were addressed and the rationale for grayscale exposure was presented. Chapter 2 provided a detailed background on photopolymerization, the PCMS used in LAMP, and photopolymerization characterization techniques such as cure depth measurements and FTIR-ATR. Chapter 2 also presented a literature review of grayscale exposure techniques incorporated into photocuring for single layer and multiple layer fabrications, and methods for characterizing volumetric shrinkage and shrinkage stress which results from photopolymerization. Chapter 3 provided an optical analysis of the UV projected from the SLM. It was found that grayscale images reduce the average light intensity by the grayscale value of the projected image and was independent of the screening resolution and technique used. However, it was found that the peak intensities are relatively unaffected by grayscale exposure and the peak intensity of one projected pixel is

approximately equivalent to the peak intensity resulting the projection of every pixel. Chapter 4 characterized the influence of grayscale exposure and homogenous transition exposure on the cure depth. It was found that the cure depth from grayscale exposure responds to the average light intensity incident to the surface, which is equivalent to the grayscale value of the project image. Comparisons between grayscale exposure and uniform light intensity variation were made. It was found that the critical energy varies with uniform light intensity and similar trends were found for grayscale exposure. However, the trends in resin sensitivity with grayscale exposure deviated from the trends in uniform light intensity variation. Chapter 4 also investigated the dimensional limits of grayscale. It was found that there exists a range of feature sizes that produce cure depths that cannot be described by grayscale exposure or all white exposure, which was called homogenous transition exposure. This region was characterized by an adapted exposure time working curve. Through cure depth experiments it was observed that the critical exposure time and resin sensitivity exhibited minimums for specific lengths of exposure features. Chapter 5 discussed the results from Chapter 4. The radical depletion model was used to interpret the dependence of critical energy on light intensity and its predictions were compared to grayscale exposure. Homogenous transition exposure was discussed and a new model based on scattering length pixelation was introduced to predict the light intensity distribution based on the length scale of the projected features. The model was assessed and excellent agreement between experimental results and theory was displayed. Chapter 6 applies the results of Chapter 4 and 5 to LAMP. Novel techniques based on grayscale exposure were developed to fabricate unsupported geometries and reduced defects with arise during BBO and sintering. Grayscale exposure demonstrated the

successful ability to fabricate unsupported geometries. Homogenous transition exposure at a specified length scale of projected features was found to reduce long range horizontal defects during BBO. However, long range defects may have been interchanged with micro-defects.

7.1 Contributions

This thesis provided contributions by charactering the effects of grayscale exposure and homogenous transition exposure. This thesis also developed a deeper understanding of cure depths resulting from different length scales of exposure features, through the introduction of the scattering length pixelation model. Additionally, breakthroughs were made in the advancement of LAMP to fabricate unsupported geometries without the need for support structures. A rationale for using GSS was introduced and a novel method of "print-though mediated alternating GSS" was developed to accurately and reliably fabricate unsupported features using grayscale exposure. GSS enables the fabrication of unsupported features in internal passages where typical support structures cannot be used. This thesis also developed a technique to reduce long range horizontal defects which arise during BBO and sintering through utilizing homogenous transition exposure.

7.2 Future Work

Due to the many successes presented, there are many avenues to expand research efforts. The scattering length pixelation model successfully predicted the light intensity distribution resulting within homogenous transition exposure. However, the model could not predict the resin sensitivity, so experimental resin sensitivity values were used. Therefore, future work could pursue the development of a simple technique to predict the

resin sensitivity or scattering length based on the dimensions of exposure features. This thesis also successfully demonstrated the fabrication of unsupported features using GSS on a test component. The true test of GSS would be to incorporate GSS into the fabrication of integrally-cored airfoil molds. Homogenous transition exposure was shown to reduce horizontal defects generated during BBO and sintering. However, the surface quality of the test component was reduced and the test component was prone to vertical defects and cracks. Therefore, the test components could be redesigned to investigate the influence of including an all white edge to the surface. This may assist in reducing vertical defects and maintain a smooth outer surface. Results from this thesis and the proposed additional investigation could be assessed and the optimal design could be determined for use in integrally-cored airfoil molds to reliably produce molds with minimal defects.

APPENDIX

Summary of Gaussian Regressions of Light Intensity Profiles

$$I(x,y) = \sum_{i}^{n} I_i exp\left(-\left(\frac{(x-\mu_{x,i})^2}{{r_{x,i}}^2} + \frac{(y-\mu_{y,i})^2}{{r_{y,i}}^2}\right)\right) \quad \text{A.1}$$

Table A.1: Summary of the regression parameters obtained from the Gaussian regressions of light intensity profiles in Chapter 3

n	i	1	2	3	4	5	6	7	8	9	10
10	I	3766	4028	3614	4083	4015	4005	4083	3419	4054	3764
	μ_x	16.21	16.13	16.21	16.26	16.26	16.26	16.30	16.28	16.29	16.26
	μ_y	14.95	32.72	50.33	66.41	83.94	100.79	118.34	134.09	151.54	169.62
	r_x	8.38	8.44	8.44	8.45	8.46	8.46	8.47	8.48	8.44	8.35
	r_y	7.73	11.49	7.79	9.18	8.68	8.57	9.40	7.36	12.13	7.65
5	I	3851	3911	3860	4028	4028					
	μ_x	19.15	19.08	19.13	19.08	19.08					
	μ_y	18.73	35.76	54.17	70.99	87.99					
	r_x	8.45	8.49	8.53	8.41	8.41					
	r_y	7.82	10.01	9.31	7.90	7.90					
4	I	3851	3911	3860	4028						
	μ_x	19.15	19.08	19.13	19.08						
	μ_y	18.73	35.76	54.17	70.99						
	r_x	8.45	8.49	8.53	8.41						
	r_y	7.82	10.01	9.31	7.90						
3	I	3440	3783	3490							
	μ_x	19.20	19.15	19.08							
	μ_y	18.10	36.20	54.56							
	r_x	8.47	8.54	8.47							
	r_y	7.43	12.39	7.57							
2	I	4185	4216								
	μ_x	19.03	19.07								
	μ_y	38.77	21.73								
	r_x	8.39	8.37								
	r_y	8.01	8.73								
1	I	4407									
	μ_x	19.46									
	μ_y	25.21									
	r_x	8.35									
	r_y	8.20									

Summary of Curing Parameters from Grayscale Exposure and Homogenous Transition Exposure

Table A.2: Summary of the curing parameters and confidence interval calculated for grayscale exposure.

	Summary of Critical Energy (mJ/cm^2) for Grayscale Exposure																	
	100%		90%		80%		70%		60%		50%		40%		30%		20%	
screening technique	**Ec**	**CI**	**Ec**	**CI**	**Ec**	**CI**	**Ec**	**CI**	**Ec**	**CI**	**Ec**	**CI**	**Ec**	**CI**	**Ec**	**CI**	**Ec**	**CI**
HDS super fine	130.5	10.2	136.0	15.0	135.4	16.9	129.0	15.6	124.8	13.5	119.4	13.5	113.2	14.7	109.2	18.3	110.7	10.6
HDS fine	131.6	15.1	131.1	12.6	138.3	15.2	131.3	11.6	129.6	10.7	119.8	9.1	117.0	8.0	111.5	8.5	109.4	6.3
HDS medium	132.7	11.3	127.3	10.8	132.7	13.2	129.7	11.6	123.5	14.3	117.5	11.8	117.5	9.5	111.5	10.3	107.9	8.9
HDS coarse	129.0	13.7	127.1	12.9	129.7	13.1	127.8	16.4	120.2	18.0	119.3	13.6	114.9	15.6	110.3	11.1	107.8	15.4
HDS super coarse	133.4	11.4	125.0	13.7	130.2	14.9	128.2	14.8	120.8	13.7	120.1	11.6	117.4	12.0	117.3	17.7	104.8	19.3
Cumulative	**132.0**	**5.6**	**129.0**	**5.9**	**132.9**	**6.4**	**129.1**	**6.0**	**123.5**	**6.3**	**119.0**	**5.3**	**116.1**	**5.1**	**111.9**	**5.7**	**108.7**	**4.8**

	Summary of Resin Sensitivity (µm) for Grayscale Exposure																	
	100%		90%		80%		70%		60%		50%		40%		30%		20%	
screening technique	**D_p**	**CI**	**D_p**	**CI**	**D_p**	**CI**	**D_p**	**CI**	**D_p**	**CI**	**D_p**	**CI**	**D_p**	**CI**	**D_p**	**CI**	**D_p**	**CI**
HDS super fine	212.0	2.5	216.6	3.5	212.4	4.0	209.0	3.7	203.9	3.3	205.1	3.4	201.2	3.9	196.2	5.0	200.7	3.2
HDS fine	212.3	3.6	212.7	3.1	215.0	3.5	210.9	2.8	208.9	2.6	205.8	2.3	204.7	2.1	199.4	2.3	200.5	1.8
HDS medium	213.5	2.7	209.6	2.7	210.1	3.1	208.9	2.8	202.6	3.5	202.9	3.0	204.2	2.5	198.5	2.8	198.5	2.5
HDS coarse	209.4	3.3	208.4	3.2	206.5	3.2	206.5	4.0	200.6	4.5	204.1	3.5	201.4	4.1	196.5	3.0	197.4	4.5
HDS super coarse	213.3	2.7	207.5	3.4	208.3	3.6	208.1	3.6	200.8	3.4	204.2	2.9	203.6	3.1	202.9	4.6	194.9	5.5
Cumulative	**212.5**	**1.3**	**210.8**	**1.4**	**210.2**	**1.5**	**208.6**	**1.4**	**203.1**	**1.5**	**204.2**	**1.3**	**203.2**	**1.3**	**198.7**	**1.5**	**199.0**	**1.4**

Table A.3: Summary of the critical curing parameters obtained for Homogenous Transition Exposure curing the checkerboard exposure pattern of variable square length.

Square Length (µm)	t_c (ms)	D_p (µm)
17	82.1	216.6
51	80.7	214.5
85	82.6	214.6
170	70.7	199.9
255	62.9	199.3
306	51.9	190.8
340	48.0	186.6
374	44.3	186.0
425	40.1	181.6
544	41.1	189.5
595	44.5	200.1
680	47.2	203.8
1360	51.4	222.8

MATLAB Program for the Scattering Length Pixelation Model

```
clc

clear all

tic

% Program to Simulate the Light Intensity Distribution Experienced by
the

% Photocurable Material System


% Import the desired projected image

A = imread('50%_30x30.bmp');

size_a = size(A);

n=size_a(1);

m=size_a(2);

Cell_1=cell(n,m,1);

Io=1.6;                % Experimental All White Light Intensity

px=17;                 % Pixel size in microns

int = 1;               % Number of cells per pixel

for i=1:1:n

    for j=1:1:m

        Cell_1{i,j,1}=repmat(A(i,j),int,int);

    end

end

% Assume constant all white light intensity for each projectd pixel

Ii=Io*cell2mat(Cell_1);


X=1:px/int:(n)*px;  % Convert image to the proper length scale

Y=1:px/int:(m)*px;

[x, y] = meshgrid(X,Y);

n=length(X);

m=length(Y);
```

```
I_1 = 0;


% material properties
Dp = 200.8; % dependent on the exposure feature length scale
% determine scattering length from material properties and Dp
l_sc_1=(10000/Dp-5.724)^(-1)*10000
l_sc = round(l_sc_1/px*int);


% light intensity that the material sees
clear i j
size_2 = size(Ii);
N_2 = size_2(1);
M_2 = size_2(2);
I_2=zeros(N_2,M_2);
a=zeros(N_2,M_2);
% Find the average light intensity developed at each projected pixel
for i = l_sc+1:1:N_2-l_sc
    for j = l_sc+1:1:M_2-l_sc
        a = Ii((i-l_sc):1:i+l_sc , (j-l_sc): 1 :j+l_sc );
        size_a = size(a);
        n_a=size_a(1);
        m_a=size_a(2);
        for k=1:1:n_a
            for l=1:1:m_a
%               Determine the power input into the material system pixel
                if sqrt((k-(l_sc))^2+(l-(l_sc+1))^2)<=l_sc
                    a(k,l) = a(k,l);
                else
                    a(k,l)=0;
                end
```

```
%                 Determine the light intenisty at the pixel center by
%                 dividing the total power input to the material system
%                 pixel by the pixel area
                I_2(i,j) = sum(sum(a))/(pi*l_sc^2);
            end
        end
    end
end
figure(2)
surfc(X,Y,I_2)
xlabel('microns')
ylabel('microns')
zlabel('I (W/cm^2)')
title('Light intensity for 510 micron square length')
% Predict the resultant cure depth and working curve
t=300:100:1200
% find the maximum intensity developed within the material system
I_2max=max(max(I_2))
% Write the data to excel
I_max=I_2max*ones(length(t))
l_sc_2=l_sc*ones(length(t))
% Use the experimental intensity dependent critical energy dose
Ec=19.6*I_2max+103.7;
% calculate the cure depth for various exposure times
Cd=Dp*log(I_2max*t/Ec)
data=[l_sc_2;I_max;t;Cd]
xlswrite('C:\Users\mconrad3\Documents\MATLAB15x15_2',data)
toc
```

Summary of Hill's Three Parameter Regression of the Degree of Conversion

$$\alpha(t) = \frac{at^b}{c^b + t^b} \qquad \text{A.2}$$

Table A.4: Summary of the regression parameters and coefficient of determination determined for the degree of conversion measurements at different grayscale values (G) with a screening resolution of HDS super fine.

G	100%	80%	60%	40%	20%
a	0.813	0.798	0.770	0.827	0.920
b	2.660	2.206	2.617	2.069	1.705
c	309	295	390	533	962
R^2	0.980	0.984	0.984	0.983	0.991

REFERENCES

[1] R. F. Smart and B. P. R., *Investment Casting (Materials Science)*: Maney Materials Science, 1995.

[2] S. Kalpakjian and S. R. Schmid, *Manufacturing Processes for Engineering Materials*, 5 ed.: Prentice Hall, 2008.

[3] P. Dodge, "Cracks in Large Area Maskless Photopolymerization Molds," Undergraduate Project Report, Materials Science and Engineering Department, Univeristy of Michigan, 2011.

[4] S. Das, J. Halloran, and W. Baker, "Direct Digital Manufacturing of Airfoils," Proposal to DARPA DSO, 2008.

[5] C.-J. Bae, "INTEGRALLY CORED CERAMIC INVESTMENT CASTING MOLD FABRICATED BY CERAMIC STEREOLITHOGRAPHY," PhD, Materials Science and Engineering, University of Michigan, 2008.

[6] D. Yuan, P. Cilino, A. Rudraraju, T. Wu, T. R. Alabi, M. Conrad, V. Tomeckova, S. Gentry, R. Breneman, P. Dodge, W. Baker, D. Deptowicz, J. Halloran, and S. Das, "Recent Progress on Direct Digital Manufacturing of Airfoils using Large Area Maskless Photpolymerization," in *22nd Annual SFF Symposium*, Austin, TX, 2011.

[7] P.-T. Lan, S.-Y. Chou, L.-L. Chen, and D. Gemmill, "Determining fabrication orientations for rapid prototyping with Stereolithography apparatus," *Computer-Aided Design,* vol. 29, pp. 53-62, 1997.

[8] P. Karrer, S. Corbel, J. C. Andre, and D. J. Lougnot, "SHRINKAGE EFFECTS IN PHOTOPOLYMERIZABLE RESINS CONTAINING FILLING AGENTS - APPLICATION TO STEREOPHOTOLITHOGRAPHY," *Journal of Polymer Science Part a-Polymer Chemistry,* vol. 30, pp. 2715-2723, Dec 1992.

[9] K. Kambly, "Characterization of Curing Kinetics and Photopolymerization Shrinkage in Ceramic-Loaded Photocurable Resins for Large Area Maskless Photopolymerization," M.S. Thesis, Mechanical Engineering, Georgia Institute of Technology, Atlanta, 2009.

[10] P. Dodge, "First Batch of Molds; Observations," J. Halloran, S. Gentry, and R. Breneman, Private Communication, 2011.

[11] J. Atencia, S. Barnes, J. Douglas, M. Meacham, and L. E. Locascio, "Using pattern homogenization of binary grayscale masks to fabricate microfluidic structures with 3D topography," *Lab on a Chip,* vol. 7, pp. 1567-1573, 2007.

[12] C. L. Davidson and A. J. Feilzer, "Polymerization shrinkage and polymerization shrinkage stress in polymer-based restoratives," *Journal of Dentistry,* vol. 25, pp. 435-440, 1997.

[13] P. F. Jacobs, *Rapid Prototyping and Manufacturing: Fundamentals of Stereolithography*: Society of Manufacturing Engineers, 1992.

[14] C. Decker, "Photoinitiated crosslinking polymerisation," *Progress in Polymer Science,* vol. 21, pp. 593-650, 1996.

[15] E. Andrzejewska, "Photopolymerization kinetics of multifunctional monomers," *Progress in Polymer Science,* vol. 26, pp. 605-665, May 2001.

[16] J. H. Lee, R. K. Prud'homme, and I. A. Aksay, "Cure depth in photopolymerization: Experiments and theory," *Journal of Materials Research,* vol. 16, pp. 3536-3544, Dec 2001.

[17] G. Odian, "Radical Chain Polymerization," in *Principles of Polymerization*, ed: John Wiley & Sons, Inc., 2004, pp. 198-349.

[18] A. Boddapati, "Modeling cure depth during photopolymerization of multifunctional acrylates," M.S. Thesis, Chemical Engineering, Georgia Institute of Technology, Atlanta, 2010.

[19] N. Fang, C. Sun, and X. Zhang, "Diffusion-limited photopolymerization in scanning micro-stereolithography," *Applied Physics A: Materials Science & Processing,* vol. 79, pp. 1839-1842, 2004.

[20] C. E. Hoyle, C. H. Chang, and M. A. Trapp, "Laser-initiated polymerization of methyl methacrylate: effect of pulse repetition rate and photoinitiator concentration on polymerization efficiency," *Macromolecules,* vol. 22, pp. 3607-3611, 1989/09/01 1989.

[21] F. N. Sun C, Wu D M and Z. X, "Projection micro-stereolithography using digital micro-mirror dynamic mask," *Sensors and Actuators,* vol. 121, p. 113, 2005.

[22] K. C. Wu, K. F. Seefeldt, M. J. Solomon, and J. W. Halloran, "Prediction of ceramic stereolithography resin sensitivity from theory and measurement of diffusive photon transport," *Journal of Applied Physics,* vol. 98, Jul 2005.

[23] C. Sun and X. Zhang, "Experimental and numerical investigations on microstereolithography of ceramics," *Journal of Applied Physics,* vol. 92, pp. 4796-4802, Oct 2002.

[24] V. Tomeckova and J. W. Halloran, "Predictive models for the photopolymerization of ceramic suspensions," *Journal of the European Ceramic Society,* vol. 30, pp. 2833-2840, Oct 2010.

[25] V. Tomeckova and J. W. Halloran, "Critical energy for photopolymerization of ceramic suspensions in acrylate monomers," *Journal of the European Ceramic Society,* vol. 30, pp. 3273-3282, Dec 2010.

[26] K. C. Wu and J. W. Halloran, "Photopolymerization monitoring of ceramic stereolithography resins by FTIR methods," *Journal of Materials Science,* vol. 40, pp. 71-76, 2005.

[27] F. Jack L, "Correlation between hardness and degree of conversion during the setting reaction of unfilled dental restorative resins," *Dental Materials,* vol. 1, pp. 11-14, 1985.

[28] R. P. Slopek, "In-situ Monitoring of the Mechanical Properties during the photopolymerization of acrylate resins using particle tracking microrheology," Ph.D. Thesis, Chemical and Biomolecular Engineering, Georgia Institute of Technology, Atlanta, 2008.

[29] G. Gal, "Method for fabricating microlenses," United States Patent 5310623, 1994.

[30] Y. T. Lu, C. S. Chu, and H. Y. Lin, "Characterization of the gray-scale photolithography with high-resolution gray steps for the precise fabrication of diffractive optics," *Optical Engineering,* vol. 43, pp. 2666-2670, Nov 2004.

[31] Y. Oppliger, P. Sixt, J. M. Stauffer, J. M. Mayor, P. Regnault, and G. Voirin, "One-step 3D shaping using a gray-tone mask for optical and microelectronic applications," *Microelectronic Engineering,* vol. 23, pp. 449-454, 1994.

[32] C. G. Xia and N. Fang, "Fully three-dimensional microfabrication with a grayscale polymeric self-sacrificial structure," *Journal of Micromechanics and Microengineering,* vol. 19, Nov 2009.

[33] Y. Lu and S. C. Chen, "Direct write of microlens array using digital projection photopolymerization," *Applied Physics Letters,* vol. 92, Jan 2008.

[34] L. A. Mosher, "Double Exposure Gray-Scale Photolithography," M.S. Thesis, Electrical and Computer Engineering, University of Maryland, 2008.

[35] J. W. Stansbury, M. Trujillo-Lemon, H. Lu, X. Z. Ding, Y. Lin, and J. H. Ge, "Conversion-dependent shrinkage stress and strain in dental resins and composites," *Dental Materials,* vol. 21, pp. 56-67, Jan 2005.

[36] J. W. Stansbury and S. H. Dickens, "Determination of double bond conversion in dental resins by near infrared spectroscopy," *Dental Materials,* vol. 17, pp. 71-79, Jan 2001.

[37] A. Peutzfeldt, "Resin composites in dentistry: The monomer systems," *European Journal of Oral Sciences,* vol. 105, pp. 97-116, Apr 1997.

[38] L. G. Lovell, H. Lu, J. E. Elliott, J. W. Stansbury, and C. N. Bowman, "The effect of cure rate on the mechanical properties of dental resins," *Dental Materials,* vol. 17, pp. 504-511, Nov 2001.

[39] N. Emami, K.-J. M. Söderholm, and L. A. Berglund, "Effect of light power density variations on bulk curing properties of dental composites," *Journal of Dentistry,* vol. 31, pp. 189-196, 2003.

[40] M. R. Bouschlicher, M. A. Vargas, and D. B. Boyer, "Effect of composite type, light intensity, configuration factor and laser polymerization on polymerization contraction forces," *American Journal of Dentistry,* vol. 10, pp. 88-96, Apr 1997.

[41] L. Feng and B. I. Suh, "A mechanism on why slower polymerization of a dental composite produces lower contraction stress," *Journal of Biomedical Materials Research Part B-Applied Biomaterials,* vol. 78B, pp. 63-69, Jul 2006.

[42] P. D. Ganahl, "Structured illumination as a processing method for controlling photopolymerized coating characteristics," Ph.D. Thesis, Chemical and Biochemical Engineering, University of Iowa, 2007.

[43] V. Tomeckova and J. W. Halloran, "Cure depth for photopolymerization of ceramic suspensions," *Journal of the European Ceramic Society,* vol. 30, pp. 3023-3033, 2010.

[44] J. Halloran, "Comparing Hanovia Spectrum with the Georgia Tech Spectrum," D. Yuan, Private Communication, 2009.

[45] Global Graphics, "Harlequin RIP OEM Manual," ed, 2007.

[46] J. W. Halloran, V. Tomeckova, and B. J. Love, "Intensity Effects on the Photopolymerization of Powder Suspensions," in *12th Conference of the European Ceramic Society*, Stockholm, Sweeden, 2011.

[47] M. L. Griffith and J. W. Halloran, "Scattering of ultraviolet radiation in turbid suspensions," *Journal of Applied Physics,* vol. 81, pp. 2538-2546, Mar 1997.

[48] F. A. Ogliari, C. Ely, G. S. Lima, M. C. M. Conde, C. L. Petzhold, F. F. Demarco, and E. Piva, "Onium salt reduces the inhibitory polymerization effect from an organic solvent in a model dental adhesive resin," *Journal of Biomedical Materials Research Part B: Applied Biomaterials,* vol. 86B, pp. 113-118, 2008.

[49] D.-S. Tsai, "Pressure buildup and internal stresses during binder burnout: Numerical analysis," *AIChE Journal,* vol. 37, pp. 547-554, 1991.

[50] P. Bhargava, A. Bandyopadhyay, S. Rangarajan, G. Qi, C. Dai, S. Wu, S. Danforth, and A. Safari, "Shrinkage, weight loss and crack prevention during binder burn out of components produced by fused deposition of ceramics (FDC)," in *Solid Freeform Fabrication Proceedings, September 1997*, D. L. Bourell, J. J. Beaman, R. H. Crawford, H. L. Marcus, and J. W. Barlow, Eds., ed, 1997, pp. 395-402.

[51] C.-J. Bae and J. W. Halloran, "Influence of Residual Monomer on Cracking in Ceramics Fabricated by Stereolithography," *International Journal of Applied Ceramic Technology,* pp. no-no, 2010.

[52] D. C. Watts, "Reaction kinetics and mechanics in photo-polymerised networks," *Dental Materials,* vol. 21, pp. 27-35, 2005.